Numerical and experimental analysis of multiple Chua circuits

van der Steen, R.

Award date:
2006

Numerical and experimental analysis of multiple Chua circuits

R. van der Steen

DCT 2006.15

Master's thesis

Coaches:	prof. dr. H. Nijmeijer ir. L. Kodde
Supervisor:	prof. dr. H. Nijmeijer
Committee:	prof. dr. H. Nijmeijer ir. L. Kodde prof. dr. D. Lenstra dr. ir. M.K. Camlibel

Eindhoven University of Technology
Department of Mechanical Engineering
Dynamics and Control group

Eindhoven, January, 2006

Abstract

Nonlinear systems can have multiple equilibria or limit cycles and bifurcations can change the qualitative features of a system, which can result in very complex behavior. Some examples are the global weather, turbulence of fluids or chemical reactions.

The objective of this thesis is to achieve a better understanding of the complicated behavior of complex chaotic systems including synchronization. To provide this insight one of many possible complex systems is chosen and analyzed. The system that is considered in this thesis is the electrical Chua circuit. This seemingly simple circuit, the only nonlinearity is given by a piecewise-linear characteristic, is however capable of generating bifurcation and chaos phenomena.

The rich dynamic behavior of a Chua circuit has been analyzed by determining the stability properties of the equilibria and a Poincaré map has been derived to explain the possible bifurcations. With this powerful tool the qualitative behavior of the Chua circuit can be easily visualized. Further it is shown that the conditions, which are required for chaos, can be fulfilled.

To compare numerical results with experimental results an experimental setup has been designed and built. The parameters of the setup are estimated using two identification methods. The first method is based on measurements of the separate components of the circuit, for the second method a switching nonlinear Kalman filter is designed and implemented. The obtained numerical results are qualitatively comparable with experiments, however it is impossible to follow a chaotic trajectory if no information of the experimental trajectory is used.

Furthermore the possibility of experimental synchronization has been studied. Two synchronization methods, master-slave synchronization and mutual synchronization, have been applied.
To be able to specify asymptotic synchronization of non-identical systems a form of practical synchronization is introduced. This is necessary because it is impossible to built identical circuits, due to tolerances in electrical components.
In experiments master-slave synchronization has been achieved by applying a negative feedback to the slave system. In the case of mutual synchronization the circuits are diffusively coupled. Besides synchronization of two systems, synchronization in a network of four symmetrically coupled circuits has been investigated. It is shown that, under certain conditions, it is possible to achieve a partial synchronized situation, which is also experimentally confirmed.

Samenvatting

Niet-lineaire systemen kunnen meerdere evenwichtspunten of periodieke oplossingen bevatten en bifurcaties kunnen het kwalitatieve gedrag van een systeem veranderen. Dit heeft tot gevolg dat er zeer complex gedrag in een niet-lineair systeem kan optreden. Enkele voorbeelden hiervan zijn het weer, turbulentie in vloeistoffen en chemische reacties.

De doelstelling van dit onderzoek is het verkrijgen van een beter praktisch inzicht in het complexe gedrag van niet-lineaire chaotische systemen inclusief synchronisatie met andere systemen. Om dit inzicht te verkrijgen is een representatief systeem gekozen en onderzocht. Het systeem dat in dit onderzoek wordt beschouwd, is het elektrische Chua circuit. Dit ogenschijnlijk simpele systeem, de enige niet-lineariteit wordt beschreven door een stuksgewijze lineaire karakteristiek, vertoont bifurcaties en chaotisch gedrag.

Het variërende gedrag van het Chua circuit is geanalyseerd door het bepalen van de stabiliteits eigenschappen van de evenwichtspunten en door middel van de afleiding van een Poincaré afbeelding zijn de mogelijke bifurcaties te verklaren. Met de Poincaré afbeelding kan het kwalitatieve gedrag van het Chua circuit eenvoudig zichtbaar gemaakt worden. Eveneens is aangetoond dat aan de condities, die vereist zijn voor chaos, voldaan kan worden.

Om numerieke en experimentele resultaten met elkaar te kunnen vergelijken is er een experimentele opstelling ontworpen en gebouwd. De parameters van de opstelling zijn geschat door middel van het toepassen van twee identificatie methoden. De eerste methode is gebaseerd op metingen van de afzonderlijke componenten van het circuit, voor de twee methode is een schakelend niet-lineair Kalman filter ontworpen en geïmplementeerd. De verkregen numerieke oplossingen zijn kwalitatief vergelijkbaar met de experimenten, maar het is onmogelijk een chaotische oplossing te volgen indien er geen gebruik gemaakt wordt van meetdata.

Tevens is de mogelijkheid van synchronisatie experimenteel onderzocht. Twee synchronisatie methoden zijn toegepast, master-slave synchronisatie en synchronisatie op basis van wederzijdse koppeling. In het geval van master-slave synchronisatie wordt het gedrag van de slave opgelegd door de master. Om asymptotische synchronisatie van niet-identieke systemen te kunnen specificeren is er een vorm van praktische synchronisatie geïntroduceerd. Dit is noodzakelijk, omdat het onmogelijk is identieke circuits te fabriceren vanwege toleranties van de elektrische componenten. Master-slave synchronisatie in experimenten is verkregen door toepassing van een negatieve terugkoppeling op het slave systeem. In het geval van wederzijdse synchronisatie zijn alle circuits met elkaar gekoppeld. Behalve synchronisatie van twee systemen is ook de mogelijkheid van synchronisatie in een netwerk van vier symmetrisch gekoppelde circuits onderzocht. Er is aangetoond dat, onder bepaalde voorwaarden, er partiële synchronisatie optreedt, dit is tevens experimenteel bevestigd.

Contents

Numerical and experimental analysis of multiple Chua circuits

Chapter 1

Introduction

1.1 Complex systems

The term complex system refers to a system of parts coupled in a nonlinear fashion. Such a system may be discrete, e.g. difference equations, or it may be continuous as in a system of differential equations. Because they are nonlinear, complex systems are more than the sum of their parts because a linear system is subject to the principle of superposition, and hence is literally the sum of its parts. A linear system can have only one or an infinite number of equilibrium points. Nonlinear systems can have multiple equilibria and limit cycles. Bifurcations can change the qualitative features of a complex system such as the number of equilibrium points or limit cycles or their stability properties. This is caused by parametric variation in the model.
Complex systems are found in many fields. Some examples include the global weather, turbulence of fluids, chemical reactions and the well-known nonlinear van der Pol oscillator (van der Pol, 1927).

1.2 Chaotic systems

Complex systems are often referred to as chaotic systems. However this is not correct, a chaotic system, in contrast to complex systems, has to satisfy specific properties, which are usually very hard to verify.
The word chaos was introduced by Yorke (Li and Yorke, 1975) several years after the publication of Lorenz (Lorenz, 1963). Although Lorenz' model is considered as one of the first chaotic models, chaos was already noticed by Poincaré. In the year 1887 the king of Sweden sponsored a mathematical competition for the resolution of the question of how stable is the solar system, a variation of the three-body problem. Poincaré found that the evolution of such a system is often 'chaotic' in the sense that a small perturbation in the initial state such as a slight change in one body's initial position might lead to a radically different later state (Poincaré, 1890).
However after the work of Lorenz chaos has developed into a new research area. Smale developed the so-called horseshoe map (Smale, 1967). A new view on the turbulence problem was given by (Ruelle and Takens, 1971), which led to the so-called 'strange' attractor in the phase space. A system inspired by the work of Lorenz is the Rössler system (Rössler, 1976), which has only one spiral instead of two. Another well-known example from biology is the population map or logistic equation (May, 1976), which was investigated further by Feigenbaum. Feigenbaum developed the base of what is now known as the Feigenbaum number. He described that in systems where period doubling occur, the period doubling follows a constant relation (Feigenbaum, 1978).
To illustrate the very complex behavior of chaotic systems we look at the, at first sight simple, logistic equation $x_{t+1} = f(x_t)$ with $f(x) = \alpha x(1-x),\ x \in [0,\ 1]$ for some values of α, see figure 1.1.

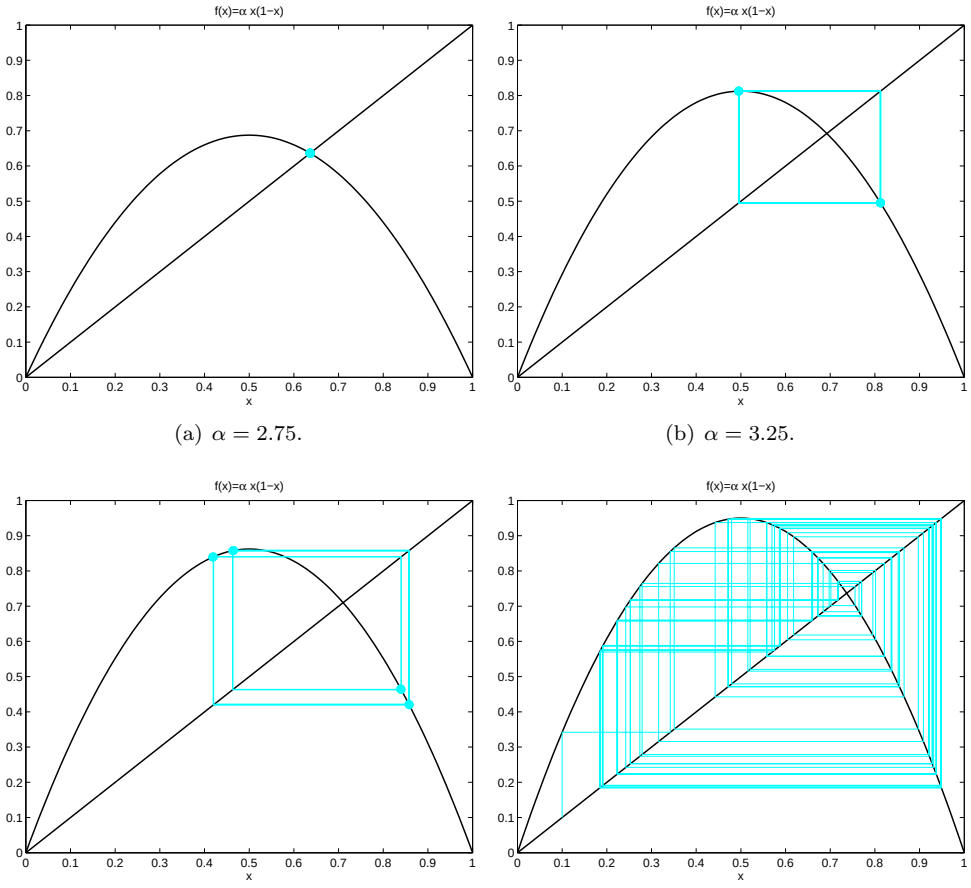

(a) $\alpha = 2.75$.

(b) $\alpha = 3.25$.

(c) $\alpha = 3.449$.

(d) $\alpha = 3.8$.

Figure 1.1: 140 iterations of $f(x) = \alpha x(1-x)$ for four different values of α. If $1 < \alpha < 3$ we have one stable fixed point, i.e., after a number of iterations $x_{t+1} = x_t$. If the value of $\alpha > 3$ this fixed point loses its stability and a period doubling bifurcation occurs, if α is increased further several period doubling bifurcations occur and for $3.570 < \alpha < 4$ the dynamics are very complicated. The trajectories appear to wander around randomly.

1.3 Synchronization

The Dutch scientist Christiaan Huygens was probably the first who described synchronization. He discovered that two pendulum clocks hanging from a beam exhibit anti-phase synchronization, i.e. the two pendulums move in opposite directions (Huygens, 1986). Huygens used the pendulum clock to solve the problem of finding longitude at sea, but ironically his discovery that the pendulums influenced each other led the Royal Society to lose faith in pendulum clocks as a solution to the longitude problem.

Synchronization can be understood as the adjustment of rhythms of oscillating objects due to weak interaction (Pikovsky *et al.*, 2001). The requirement of (self-sustaining) oscillating objects gives an indication that complex systems are needed to make synchronization possible. Synchronization is encountered in several fields e.g. (van der Pol and van der Mark, 1928; Winfree, 1980; Gray, 1994; Pikovsky *et al.*, 2001; Nijmeijer and Rodrigues-Angeles, 2003).

However since the publication of (Pecora and Carroll, 1990), chaotic synchronization has been receiving much interest in literature. Some examples of applications of chaotic synchronization can be found in (Dedieu *et al.*, 1993; Terry *et al.*, 1999; Ticos *et al.*, 2000). Synchronization of

electrical circuits is considered in (Heagy *et al.*, 1994; Wu and Chua, 1995; Chua *et al.*, 1996; Matías *et al.*, 1997). A different view on chaotic synchronization, where synchronization is viewed as an observer problem, is given in (Nijmeijer and Mareels, 1997; Santoboni *et al.*, 2001).

1.4 Objective

The main goal of this thesis is to get more insight in the complicated behavior of complex (chaotic) systems including synchronization, not only at a theoretical level, but also based on experimental results. To achieve this we divide the objective into the following aspects

- Analysis of a single complex system.
- Development and comparison of numerical and experimental results.
- Synchronization of multiple complex systems; when are two coupled complex systems synchronized?

First of all we need to choose a complex system to investigate. As already mentioned there are many possible choices. However we want to include experimental results and that gives some practical restrictions. Although the drill-string setup in the DCT-lab (Mihajlovic, 2005) is a complex mechanical system, it is not a practical setup to be used for synchronization due to the large dimensions. Biological cells for instance are much more appealing to be used for synchronization. But the main disadvantage of biological systems is to keep the systems and environmental conditions at an adequate level. Also the modeling of biological cells seems still an issue. Therefore we choose an electrical system. This has some great advantages, they are relatively cheap to build and the dimensions can be kept small. A well-known complex electrical system is the so-called Chua circuit (Matsumoto, 1984). This electrical circuit is a hybrid system, due to a piecewise-linear characteristic, and is capable of generating bifurcation and chaos. Although a mechanical equivalent of the Chua circuit is proposed in (Awrejcewicz and Calvisi, 2002), it is questionable of the proposed device will be able to reproduce the diverse dynamical behavior of the electrical circuit, cf. (Verhees, 2004), and therefore the electrical circuit will be used for experiments.

1.5 Outline

The outline of this thesis is as follows. In chapter 2 we start with a numerical analysis of a single Chua circuit. By varying a bifurcation parameter several trajectories are generated. We analyze these trajectories by using the equilibrium points of the system and a Poincaré map. This complex Poincaré map is approximated by a simple 1D Poincaré map. With this map the bifurcations are visualized and explained. At the end of this chapter a definition of chaos is presented. With this definition it is possible to show that a Chua system is chaotic in a mathematical context.
In the third chapter the different aspects of building a Chua circuit are explained. Two identification methods are used to obtain parameters of the fabricated realization. The first identification method is based on measurements of the used components and measurements of separate segments of the total circuit. Secondly a Kalman filter is used to estimate states and parameters for the complete circuit. Different strategies are compared and the results are discussed. In chapter 4 the experiments, which validate the numerical results, are described.
Synchronization of Chua circuits is treated in chapter 5. Two synchronization methods are presented here. First master-slave synchronization is explained and applied both numerically and experimentally. Secondly mutual synchronization is applied on a network consisting of maximal four circuits, again both numerically and experimentally.
Finally we end with conclusions and recommendations in chapter 6.

Chapter 2

Dynamics of the Chua circuit

The Chua circuit, first discovered by computer simulations (Matsumoto, 1984) and experimentally validated by (Zhong and Ayrom, 1985), is a simple autonomous electrical circuit capable of generating bifurcation and chaos phenomena. The circuit consists of all but one linear elements, a nonlinear resistor with a piecewise-linear characteristic.
The three equations of motion for the circuit are given by

$$\begin{aligned} C_1\dot{v}_1 &= G(v_2 - v_1) - f(v_1) \\ C_2\dot{v}_2 &= G(v_1 - v_2) + i_L \\ L\dot{i}_L &= -v_2 - R_0 i_L, \end{aligned} \tag{2.1}$$

with $G = \frac{1}{R}$ and the function $f(v_1)$ is defined as

$$f(v_1) = G_b v_1 + \frac{1}{2}(G_a - G_b)(|v_1 + B_p| - |v_1 - B_p|). \tag{2.2}$$

In these equations the state variables v_1 and v_2 are the voltages across the capacitors, C_1 and C_2, i_L is the current flowing through the inductor L, which has an internal resistance R_0. G_a and G_b are the conductances of the piecewise characteristic for $|v_1| < B_p$ and $|v_1| \geq B_p$ respectively. B_p is the voltage of the breakpoint. A schematic representation of a Chua oscillator can be seen in figure 2.1. After adding the resistor, R_0, the circuit has been referred to as a Chua oscillator. Another common name is the 'double scroll attractor', which will be explained later. However all names will be used throughout the text for the circuit as given in (2.1).
An example of a piecewise linear resistor is given in figure 2.2.

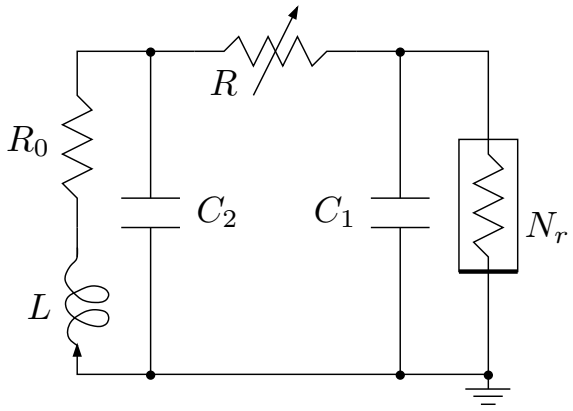

Figure 2.1: Schematic layout of a Chua circuit.

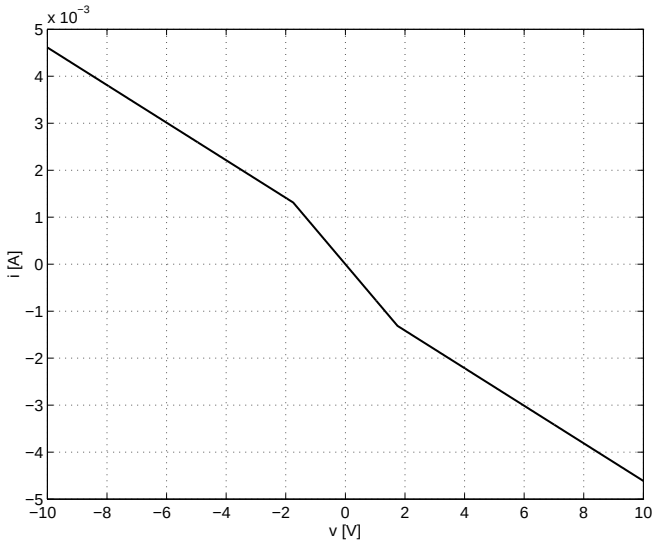

Figure 2.2: $v - i$ characteristic of the piecewise linear resistor.

2.1 Parameters

The variable resistor R, see figure 2.1, will be used as a bifurcation parameter, while all other parameters are considered fixed. In the remainder of this chapter a typical parameter set is chosen as in table 2.1.
Before we present a rigorous analysis of (2.1) some possible trajectories, with the chosen parameters, are given in the next figures to illustrate the variety of the circuit. In figure 2.3 (a), (b), (c) and (d) the periodic solutions are given for both negative and positive initial conditions. It is also possible to choose initial conditions such that the trajectory is unbounded. This is due to the fact that system (2.1) is not a passive system, see (Willems, 1972; van der Steen and Nijmeijer, 2006).

Table 2.1: Parameter values for the circuit.

Component	Value
C_1	10 [nF]
C_2	100 [nF]
L	22 [mH]
R_0	22 [Ω]
G_a	-0.75 [mS]
G_b	-0.40 [mS]
B_p	1.75 [V]

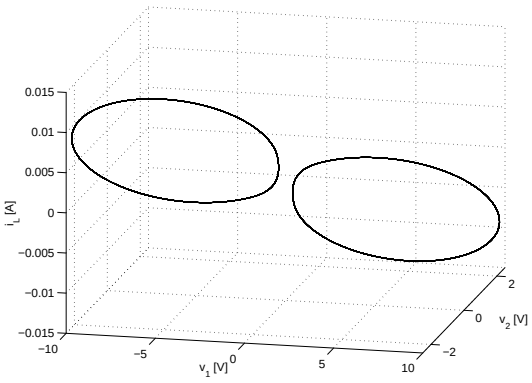

(a) $R = 1985$ [Ω].

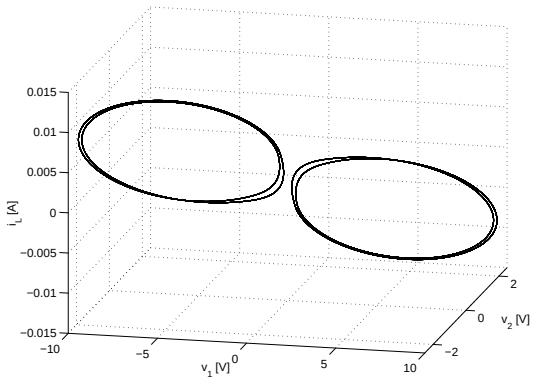

(b) $R = 1975$ [Ω].

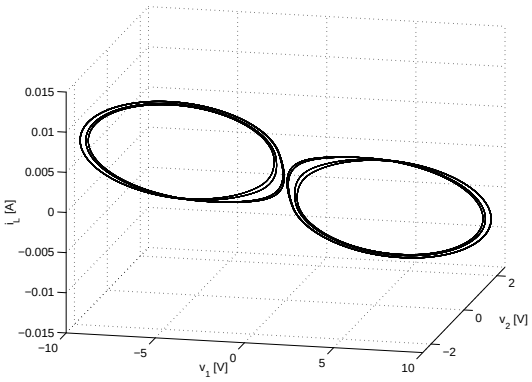

(c) $R = 1967$ [Ω].

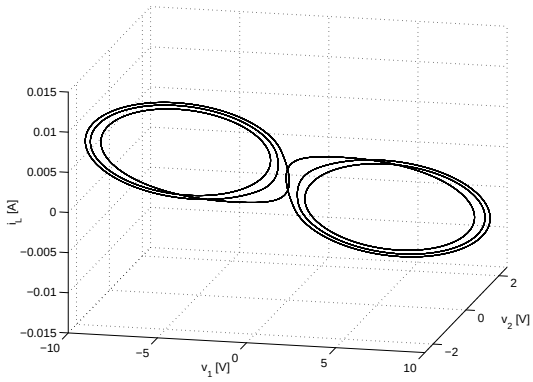

(d) $R = 1960$ [Ω].

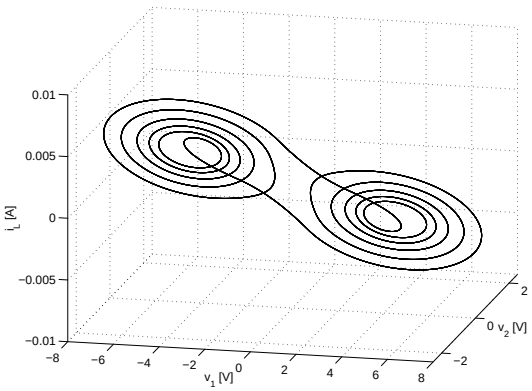

(e) $R = 1830$ [Ω].

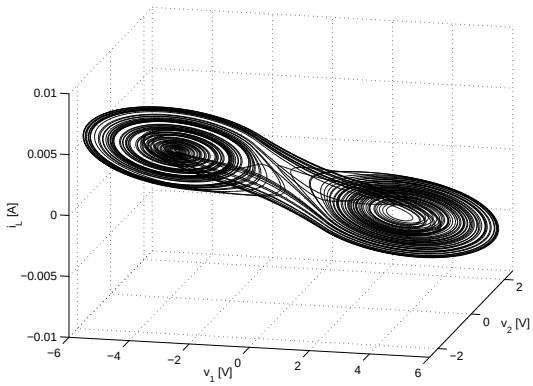

(f) $R = 1760$ [Ω].

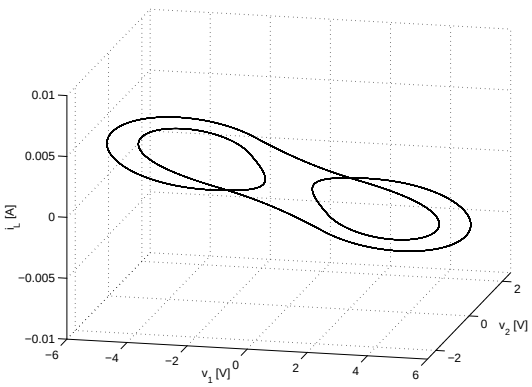

(g) $R = 1700$ [Ω].

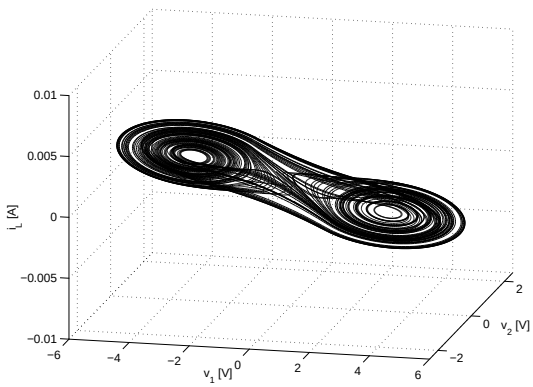

(h) $R = 1680$ [Ω].

Figure 2.3: Trajectories for different values of R.

2.2 Equilibrium points

There are three equilibrium points of (2.1), which are given by

$$eq_1 = \begin{bmatrix} \frac{B_p(-G_a+G_b)(GR_0+1)}{G+G_bGR_0+G_b} & \frac{B_pG(-G_a+G_b)R_0}{G+G_bGR_0+G_b} & -\frac{B_pG(-G_a+G_b)}{G+G_bGR_0+G_b} \end{bmatrix} \quad (2.3)$$

$$eq_2 = \begin{bmatrix} 0 & 0 & 0 \end{bmatrix} \quad (2.4)$$

$$eq_3 = \begin{bmatrix} -\frac{B_p(-G_a+G_b)(GR_0+1)}{G+G_bGR_0+G_b} & -\frac{B_pG(-G_a+G_b)R_0}{G+G_bGR_0+G_b} & \frac{B_pG(-G_a+G_b)}{G+G_bGR_0+G_b} \end{bmatrix} \quad (2.5)$$

The feasibility of these equilibrium points depends on the value of state v_1, i.e., $eq1$ and $eq3$ are only feasible if $v_1 \geq B_p$ or $v_1 \leq -B_p$ respectively, leading to the following condition for the feasibility of these equilibrium points

$$\frac{B_p(-G_a+G_b)(GR_0+1)}{G+G_bGR_0+G_b} \geq B_p. \quad (2.6)$$

Rewriting condition (2.6) and substituting the parameters values gives a lower and upper bound on the variable resistor R

$$\left|\frac{G_b}{1+G_bR_0}\right| \leq G \leq |G_a| \quad (2.7)$$

$$1333\ [\Omega] \leq R \leq 2478\ [\Omega] \quad (2.8)$$

Using (2.3) and (2.7) the lower bound of v_1, which occurs at $G = |G_a| = -G_a$, is given by

$$\frac{B_p(-G_a+G_b)(-G_aR_0+1)}{-G_a-G_bG_aR_0+G_b} \Rightarrow \frac{-B_pG_a^2R_0}{G_a+G_aG_bR_0-G_b} + B_p. \quad (2.9)$$

The nominator and denominator of (2.9) are both negative, since $B_p,\ R_0,\ G_a^2 > 0,\ G_a < G_b < 0$ and $|G_a| >> |G_aG_bR_0|$.
The theoretical upper bound of v_1 is given by

$$\lim_{G \to \left|\frac{G_b}{1+G_bR_0}\right|} \frac{B_p(-G_a+G_b)(GR_0+1)}{G+G_bGR_0+G_b} = +\infty. \quad (2.10)$$

Therefore the equilibrium point (2.3) is located at a value $v_1 > B_p$.

2.2.1 Stability of the equilibrium points

The stability of the equilibrium points is determined by the linearization of (2.1) around the equilibrium points (2.3), (2.4) and (2.5). The stability properties of the third equilibrium point are equal to the first equilibrium point because the linearization around (2.3) and (2.5) are equal. The linearization around the first equilibrium point and the origin for varying R are given in figure 2.4 (a) and (b) respectively.
It is immediately clear that the origin is always an unstable equilibrium point, while there is a region where the real part of all three eigenvalues are negative for the first (and third) equilibrium point. The crossing of the imaginary axis is numerically determined to find the stable region for the parameter R.
By means of simulation it is shown that a trajectory of system (2.1) converges to one of those equilibrium points, if R is chosen between $2007 - 2478$, for a large set of initial conditions. A prove might be obtained using the work of (Leonov *et al.*, 1996).
Further it follows from figure 2.4 (a) that there are two pure imaginary eigenvalues and one real eigenvalue at R equal to 2007 [Ω]. At this point a Hopf bifurcation, see (Guckenheimer and Holmes, 1983), occurs, i.e., the equilibrium point loses its stability and a stable limit cycle appears.

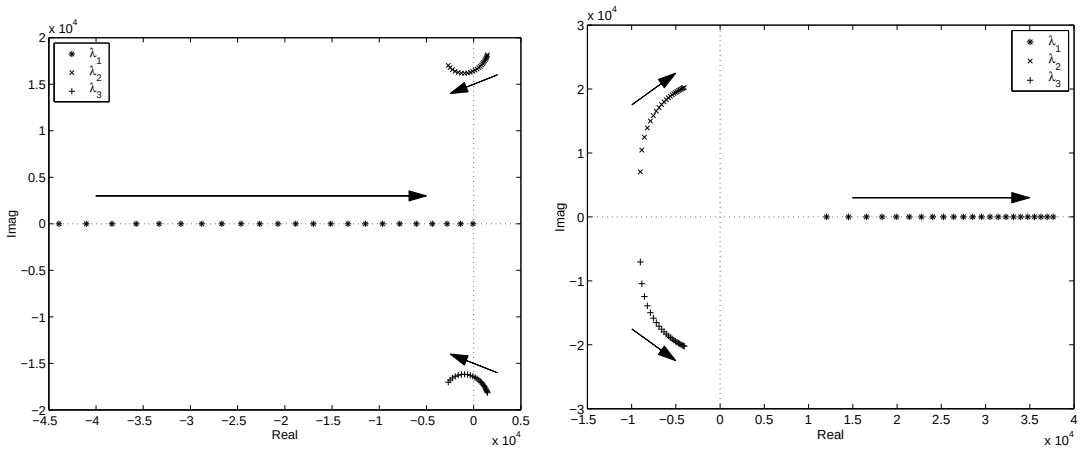

(a) Eigenvalues of linearization around eq_1.

(b) Eigenvalues of linearization around eq_2.

Figure 2.4: Stability diagram for 1333 [Ω] $<$ R $<$ 2478 [Ω]. The arrows indicate the direction of the eigenvalues for an increasing value of R. The equilibrium point eq_1 is stable for 2007 [Ω] $<$ R $<$ 2478 [Ω].

2.3 Poincaré map

To explain figure 2.3 in more detail we use the strategy described in (Chua *et al.*, 1986). In this work a one dimensional approximation of a two dimensional Poincaré map is described. With this tool it is possible to visualize the periodic solutions as well as the 'birth' and 'death' of the double scroll in a rather straightforward manner.

2.3.1 Dimensionless model

The dimensionless model of (2.1) is given by

$$\begin{aligned} \dot{x} &= \alpha(y - h(x)) \\ \dot{y} &= x - y + z \\ \dot{z} &= -\beta y - \gamma z \end{aligned} \tag{2.11}$$

where

$$\begin{aligned} h(x) &= x + f(x) = m_1 x + \frac{1}{2}(m_0 - m_1)(|x+1| - |x-1|), \\ x &= \frac{v_1}{B_p}, \qquad \alpha = \frac{C_1}{C_2}, \qquad a = RG_a, \\ y &= \frac{v_2}{B_p}, \qquad \beta = \frac{R^2 C_2}{L}, \qquad b = RG_b, \\ z &= i\frac{R}{B_p}, \qquad \gamma = \frac{RR_0C_2}{L}, \qquad \tau = \frac{t}{RC_2}. \end{aligned}$$

The breakpoints are located at $x = -1$ and $x = 1$, while the slope is equal to $m_0 = a + 1 < 0$ at the inner segment and $m_1 = b + 1 > 0$ at the outer segment. Therefore $h(x)$ can be rewritten

$$\begin{aligned} h(x) &= m_1 x + (m_0 - m_1), && x \geq 1 \\ &= m_0 x, && |x| < 1 \\ &= m_1 x - (m_0 - m_1), && x \leq 1. \end{aligned} \tag{2.12}$$

Now system (2.11) can be described by five parameters $\alpha, \beta, \gamma, m_0$ and m_1.
The vector field corresponding to (2.11), $\xi : \mathbb{R}^3 \to \mathbb{R}^3$, satisfies the following properties, cf. (Chua *et al.*, 1986):

1. ξ is symmetric with respect to the origin, i.e., $\xi(-x, -y, -z) = -\xi(x, y, z)$.
2. There a two planes U_1 and U_{-1} which are symmetric with respect to the origin and they partition $\mathbb{R}^3$ into three closed regions D_1, D_0 and D_{-1}, see figure 2.5.
3. In each region $D_i, (i = -1, 0, 1)$, the vector field ξ is affine, i.e.,
$$D\xi(x, y, x) = M_i, \ \textit{for}\ (x, y, z) \in D_i$$
where $D\xi$ denotes the Jacobian matrix of $\xi(\mathbf{x})$ and M_i a 3×3 real constant matrix.
4. ξ has three equilibrium points, one at the origin O, and one in the interior of $D_i, i = -1, 1$ denoted by $P^{\pm}$.
5. Each matrix M_i has a pair of complex conjugate eigenvalues $\tilde{\sigma}_0 \pm j\tilde{\omega}_0$ for M_0 and $\tilde{\sigma}_1 \pm j\tilde{\omega}_1$ for M_{-1} and M_1, where $\tilde{\omega}_0 > 0$ and $\tilde{\omega}_1 > 0$ and a real eigenvalue $\tilde{\gamma}_0 \neq 0$ for M_0 and $\tilde{\gamma}_1 \neq 0$ for M_{-1} and M_1.
6. The eigenspace associated with either the real or complex eigenvalues at each equilibrium point is not parallel to U_1 or U_{-1}.

$$
\begin{aligned}
A &= L_0 \cap L_1 \\
B &= L_1 \cap L_2 \\
C &= E^r(O) \cap U_1 \\
D &= E^r(P^+) \cap U_1 \\
E &= L_0 \cap L_2 \\
F &= \mathbf{x} \in L_2 : \xi(\mathbf{x}) \parallel L_2 \\
L_0 &= E^c(O) \cap U_1 \\
L_1 &= E^c(P^+) \cap U_1 \\
L_2 &= \mathbf{x} \in U_1 : \xi(\mathbf{x}) \parallel U_1
\end{aligned}
$$

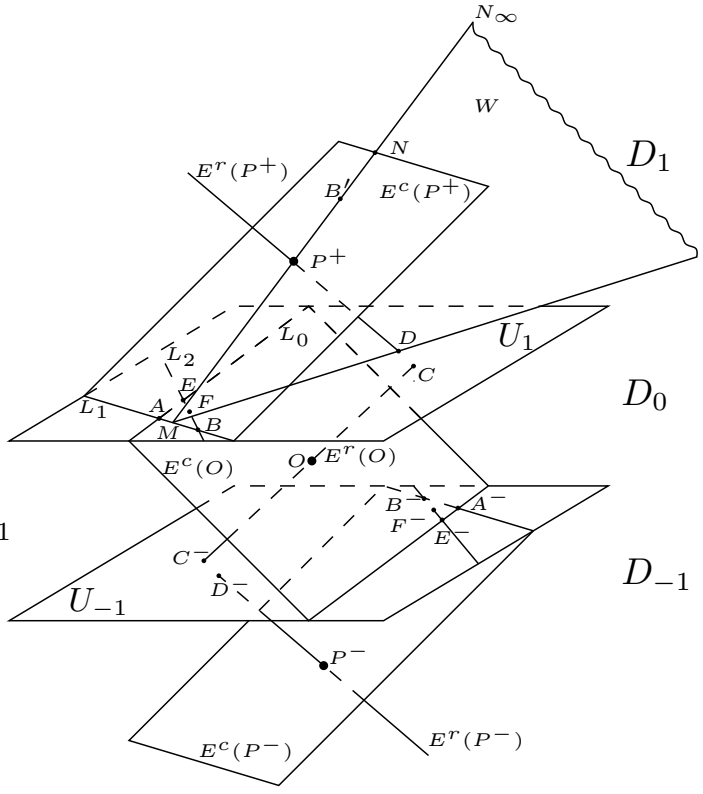

Figure 2.5: Eigenspaces of the equilibria. $E^c(0) = 2$D eigenspace spanned by the real and imaginary part of the complex eigenvalue $\tilde{\sigma}_0 \pm j\tilde{\omega}_0$, $E^r(0) = 1$D eigenspace corresponding to the real eigenvalue $\tilde{\gamma}_0$. $E^c(P^+) = 2$D eigenspace spanned by the real and imaginary part of the complex eigenvalue $\tilde{\sigma}_1 \pm j\tilde{\omega}_1$, $E^r(P^+) = 1$D eigenspace corresponding to the real eigenvalue $\tilde{\gamma}_1$.

2.3.2 Reference frame

A reference frame is introduced by two coordinate transformations for each of the linear regions D_0 and D_1:

$$\Psi_0 : D_0 \to \mathbb{R}^3, \tag{2.13}$$
$$\Psi_1 : D_1 \to \mathbb{R}^3. \tag{2.14}$$

These affine transformations reduce M_0 and M_1 to the real Jordan form (Chua *et al.*, 1986) and simultaneously transform the planes $U_{\pm 1}$ in a simple form. In the new coordinate system we have

$$\begin{aligned}
\Psi_0(0) &= 0 && (2.15)\\
\Psi_0(U_1) &= V_0 = \{(x,y,z) : x+z = 1\} && (2.16)\\
\Psi_0(U_{-1}) &= V_0^- = \{(x,y,z) : x+z = -1\} && (2.17)\\
\frac{1}{\tilde{\omega}_0} D\Psi_0(\xi(\Psi_0^{-1})) &= \xi_0(\mathbf{x}) = \begin{bmatrix} \sigma_0 & -1 & 0 \\ 1 & \sigma_0 & 0 \\ 0 & 0 & \gamma_0 \end{bmatrix} \mathbf{x} && (2.18)\\
\Psi_1(P) &= 0 && (2.19)\\
\Psi_1(U_1) &= V_1 = \{(x,y,z) : x+z = 1\} && (2.20)\\
\frac{1}{\tilde{\omega}_1} D\Psi_1(\xi(\Psi_1^{-1})) &= \xi_1(\mathbf{x}) = \begin{bmatrix} \sigma_1 & -1 & 0 \\ 1 & \sigma_1 & 0 \\ 0 & 0 & \gamma_1 \end{bmatrix} \mathbf{x} && (2.21)
\end{aligned}$$

where $\sigma_0 = \frac{\tilde{\sigma}_0}{\tilde{\omega}_0}$, $\gamma_0 = \frac{\tilde{\gamma}_0}{\tilde{\omega}_0}$, $\sigma_1 = \frac{\tilde{\sigma}_1}{\tilde{\omega}_1}$, $\gamma_1 = \frac{\tilde{\gamma}_1}{\tilde{\omega}_1}$, $\mathbf{x} = [x,y,z]^T$ and $P = P^+$. Although we still use the notation (x,y,z) it are different coordinate systems for both reference frames. However due to the subscript 0 and 1 no confusion should arise. The important points A, B, C, D, E and F from figure 2.5 are also transformed in the new reference frame and denoted by

$$\begin{aligned}
&A_0 = \Psi_0(A), \quad B_0 = \Psi_0(B), \quad C_0 = \Psi_0(C),\\
&D_0 = \Psi_0(D), \quad E_0 = \Psi_0(E), \quad F_0 = \Psi_0(F), && (2.22)\\
&A_1 = \Psi_1(A), \quad B_1 = \Psi_1(B), \quad C_1 = \Psi_1(C),\\
&D_1 = \Psi_1(D), \quad E_1 = \Psi_1(E), \quad F_1 = \Psi_1(F). && (2.23)
\end{aligned}$$

The explicit coordinates of (2.22) and (2.23) can be found in appendix A.

2.3.3 Poincaré map

In figure 2.6 we consider again figure 2.5, but now with two typical arbitrary trajectories and their corresponding trajectories in the two reference frames. The upper trajectory Γ_1 originates from a point on U_1, moves downward and turns around, before hitting U_{-1} and returns to U_1 after a certain amount of time. The trajectory continues upward, turns around and returns again on U_1. This typical trajectory defines a Poincaré map from some subset $S \subset U_1$ into S.
The Poincaré map can be decomposed into two components. A half return map, which maps the initial point on U_1 to the first return point on U_1, and a second half return map, which maps the first return point to the second return point on U_1.
The other trajectory, Γ_2 also starts at U_1, but it crosses the plane U_{-1} before it turns around and hits U_{-1} a second time. Due to the odd-symmetry of the vector field each return point $\mathbf{x}$ on U_{-1} can be identified by its reflected image $-\mathbf{x}$ in U_1. Also the portion below U_{-1} can be identified with a corresponding version of Γ_1 above U_1. This means that both typical trajectories define the same Poincaré map, which is the composition of the two half return maps. However the half returns maps cannot be calculated explicitly. Therefore the simplified but equivalent reference frames are used to compute the half return maps.

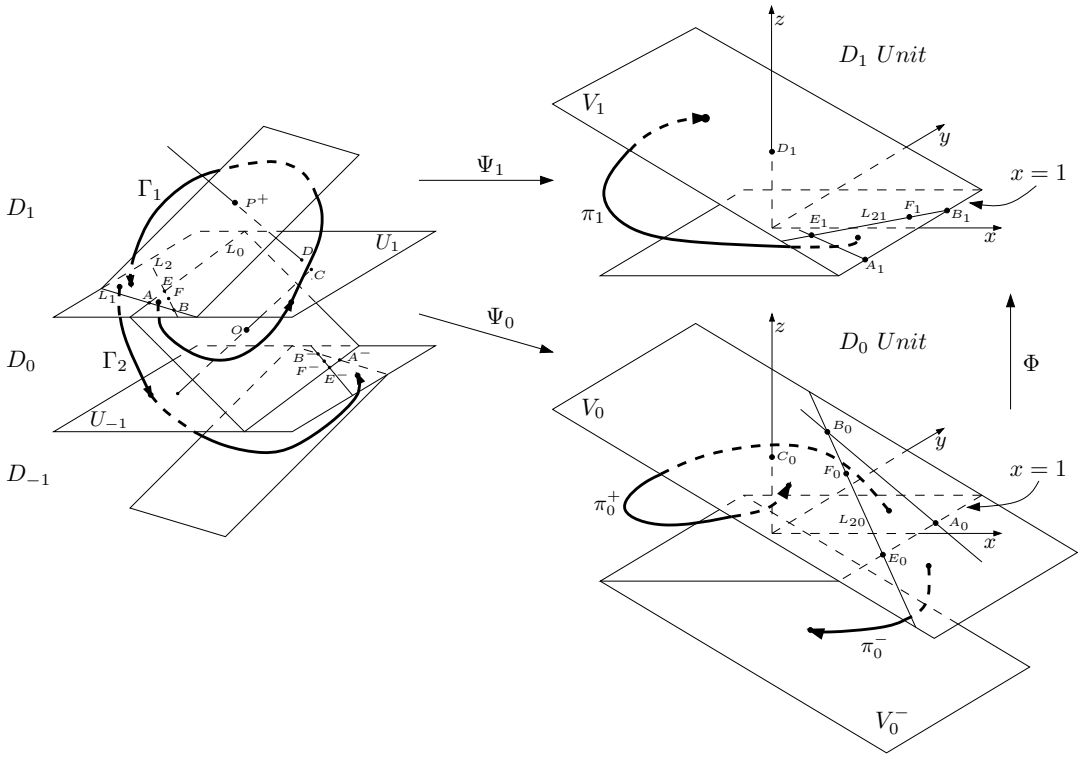

Figure 2.6: Original system with two typical trajectories and their images in the D_0 and D_1 units of the transformed system.

2.3.4 First half return map

The line L_2 in figure 2.6 is mapped into a straight line L_{20} in the D_0 unit through the points B_0 and E_0. The vector field $\xi_0(\mathbf{x})$ penetrates V_0 from above for all x to the right of L_2, while the vector field $\xi_0(\mathbf{x})$ crosses V_0 from below for x to the left of L_2. This means that any trajectory starting inside the triangular region

$$\triangle A_0B_0E_0 = \{\mathbf{x} \in V_0 | \mathbf{x} \textit{ is bounded in the triangle } A_0B_0E_0\} \tag{2.24}$$

penetrates V_0 from above and moves down. But the z-axis $= \Psi_0(E^r(0))$ corresponds to the unstable eigenvector $E^r(0)$ and therefore the trajectory moves upwards to V_0 again. This can be defined as one part of the half return map

$$\pi_0^+(\mathbf{x}) : \triangle A_0B_0E_0 \to V_0 \tag{2.25}$$

via the image

$$\pi_0^+(\mathbf{x}) = \varphi_0^T(\mathbf{x}) \tag{2.26}$$

where

$$\varphi_0^T(\mathbf{x}_0) = \begin{bmatrix} e^{\sigma_0 T}\cos(T) & -e^{\sigma_0 T}\sin(T) & 0 \\ e^{\sigma_0 T}\sin(T) & e^{\sigma_0 T}\cos(T) & 0 \\ 0 & 0 & e^{\gamma_0 T} \end{bmatrix} \begin{bmatrix} x_0 \\ y_0 \\ z_0 \end{bmatrix} \tag{2.27}$$

the flow from $\mathbf{x}$ to the first return point on V_0 at a first return time $T > 0$, where

$$T = T(\mathbf{x}) = inf\{t > 0 | \varphi_0^t(\mathbf{x}) \in V_0\}. \tag{2.28}$$

It is assumed that $\varphi_0^t(\mathbf{x})$ does not cross V_0^- before time T.
If a trajectory starts from a point in the wedge, see figure 2.6,

$$\angle A_0B_0E_0 = \{\mathbf{x} \in V_0 | \mathbf{x} \textit{ lies within the wedge extension of } \triangle A_0B_0E_0\} \tag{2.29}$$

it must go downward again and the trajectory intersects with V_0^-. This corresponds to the first part of the trajectory Γ_2 and the following map can be defined

$$\pi_0^-(\mathbf{x}) : \angle A_0B_0E_0 \backslash \triangle A_0B_0E_0 \rightarrow V_0^- \tag{2.30}$$

via the image

$$\pi_0^-(\mathbf{x}) = \varphi_0^T(\mathbf{x}) \tag{2.31}$$

where

$$T = T(\mathbf{x}) = inf\{t > 0 | \varphi_0^t(\mathbf{x}) \in V_0^-\}. \tag{2.32}$$

is now the time when the trajectory first hits V_0^-. By making use of the reflected image in V_0 the first half return map is defined as

$$\pi_0(\mathbf{x}) = \begin{cases} \pi_0^+(\mathbf{x}) & \mathbf{x} \in \triangle A_0B_0E_0 \\ -\pi_0^-(\mathbf{x}) & \mathbf{x} \in \angle A_0B_0E_0 \backslash \triangle A_0B_0E_0 \end{cases} \tag{2.33}$$

In order to calculate (2.33) a local coordinate system is introduced for points inside $\angle A_0B_0E_0$. Each point on V_0 can be defined by its x and y coordinate since the z-coordinate on V_0 is given by $z = 1 - x$. A coordinate system (u, v) is chosen such that all points $\mathbf{x} \in \angle A_0B_0E_0$ are specified in terms of (u, v). These coordinates are chosen as a weighted sum of the four corner points $A_0,\ B_0,\ E_0$ and F_0

$$\mathbf{x}_0(u, v) = u\,[vA_0 + (1 - v)E_0] + (1 - u)\,[vB_0 + (1 - v)F_0] \tag{2.34}$$

where $0 \leq u < \infty$ and $0 \leq v \leq 1$. This is visualized in figure 2.7. Note that all points inside

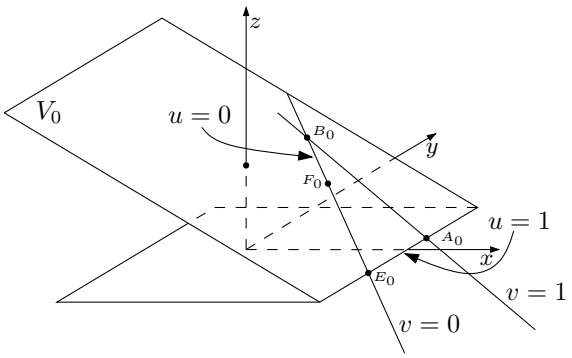

Figure 2.7: Local (u, v) coordinate system.

$\triangle A_0B_0E_0$ have $0 \leq u < 1$, while points outside this triangle have $1 \leq u < \infty$. We can rewrite (2.24) and (2.29) in an equivalent form as follows

$$\triangle A_0B_0E_0 = \{\mathbf{x}_0(u, v) | (u, v) \in [0, 1] \times [0, 1]\} \tag{2.35}$$

$$\angle A_0B_0E_0 = \{\mathbf{x}_0(u, v) | (u, v) \in [0, \infty) \times [0, 1]\}. \tag{2.36}$$

For a given $\mathbf{x}_0(u, v)$ the return map $\pi_0^+(\mathbf{x}_0)$ is now given by

$$\pi_0^+(\mathbf{x}_0) = e^{\sigma_0 t} \begin{bmatrix} \cos(t) & -\sin(t) \\ \sin(t) & \cos(t) \end{bmatrix} \mathbf{x}_0(u, v) \tag{2.37}$$

where t is the first return time and can be calculated by an inverse return time function using the v coordinate

$$u^+(v,t) = \frac{\langle \varphi_0^t(B_{0v}), h\rangle - 1}{\langle \varphi_0^t(B_{0v} - A_{0v}), h\rangle} \tag{2.38}$$

where $h = [1\ 0\ 1]^T$ is the normal vector from to origin to V_0, $\langle , \rangle$ is the inner product, A_{0v} is the location of a point along the line $\overline{E_0A_0}$, v units from E_0 and B_{0v} is the location of a point along the line $\overline{F_0B_0}$, v units from F_0.
Using the u coordinate the first return time can be calculated by

$$t = inf\{t \geq 0 | u^+(v,t) = u\}. \tag{2.39}$$

The return map $\pi_0^-(\mathbf{x}_0)$ can be calculated in a similar way using the following equations

$$u^-(v,t) = \frac{\langle \varphi_0^t(B_{0v}), h\rangle + 1}{\langle \varphi_0^t(B_{0v} - A_{0v}), h\rangle} \tag{2.40}$$

$$t = inf\{t \geq 0 | u^-(v,t) = u\}. \tag{2.41}$$

2.3.5 Second half return map

The second return map is defined in the same way as the first half return map. The only difference is that the stability properties of the equilibrium point P are opposite of the equilibrium point at the origin. Therefore we look at the inverse image, such that the stable eigenvector $E^r(P)$ and the unstable eigenvectors of $E^c(P)$ become unstable and stable respectively. This means that a trajectory crossing the V_1 plane from above inside the angular region $\angle A_1B_1E_1$ moves upwards to hit V_1. Hence the second half return map can be defined as

$$\pi_1(\mathbf{x}) : \angle A_1B_1E_1 \rightarrow V_1 \tag{2.42}$$

via the inverse image

$$\pi_1(\mathbf{x}) = \varphi_1^{-T}(\mathbf{x}) \tag{2.43}$$

where $\varphi_1^{-T}(\mathbf{x})$ is the flow from $\mathbf{x}$ to the first return point where the trajectory hits V_1 at a reverse time $-T < 0$ where

$$T = T(x) = inf\{t > 0 | \varphi_1^{-t}(x) \in V_1\}. \tag{2.44}$$

To link the first and second half return maps together we need a relation between the D_0 unit and the D_1 unit. Therefore a connection map is defined as follows

$$\Phi = (\Psi_1|_{U_1}) \circ (\Psi_0|_{U_1})^{-1} \tag{2.45}$$

where $\Psi_1|_{U_1}$ and $\Psi_0|_{U_1}$ denote the restrictions on U_1. Since the coordinates of points on the V_0 and the V_1 planes are explicitly known, it is possible to transform the coordinates of one unit into the other.
The total 2D Poincaré map can now be defined as

$$\pi : V_1' \rightarrow V_1' \tag{2.46}$$

where

$$V_1' = \{(x,y) \in V_1 | x \leq 1\} \tag{2.47}$$

and is given by

$$\pi(\mathbf{x}) = \begin{cases} \pi_1^{-1}\Phi\pi_0\Phi^{-1}(\mathbf{x}) & \mathbf{x} \in \angle A_1B_1E_1 \\ \Phi\pi_0\Phi^{-1}\pi_1^{-1}(\mathbf{x}) & \mathbf{x} \in V_1' \backslash \angle A_1B_1E_1 \end{cases} \tag{2.48}$$

2.3.6 Approximation of the Poincaré map

Instead of using the complex Poincaré map (2.48) a simpler approximation can be made. For the parameter values given in table 2.1 it holds that the real eigenvalue $|\gamma_1|$ is relatively large compared to σ_1. This means that all trajectories originating on either side of the eigenspace $E^c(P)$ will converge rapidly to this eigenspace and eventually cross the plane U_1 at the line L_1 in figure 2.5. Therefore we define a 1D approximation of the Poincaré map π by restricting its domain to a line L_1', which starts at point B, passes through A and extends to infinity. The domain of the 1D approximation map is chosen as another semi-infinite line segment. This line is constructed through the points $M = \Psi_1^{-1}[1,\ 0,\ 0]^T$ and P^+, its extension through N and then deleting the line segment between M and P^+, which defines the following Poincaré map

$$\pi^* : \overline{P^+N_\infty} \to \overline{P^+N_\infty} \tag{2.49}$$

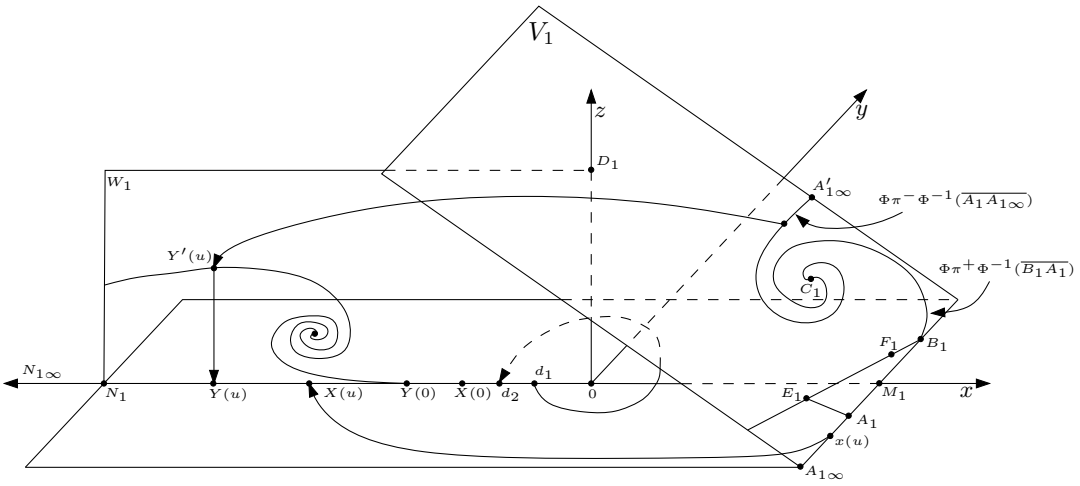

Figure 2.8: Geometrical interpretation of the one dimensional approximated Poincaré map.

In figure 2.8 the D_1 unit is shown where the plane W, which corresponds to the line segments $\overline{P^+D}$ and $\overline{ND}$ from figure 2.5, is transformed into the rectangular region

$$W_1 = \{x, y, z) \in \mathbb{R}^3 | x \leq 0, y = 0\}. \tag{2.50}$$

In terms of local coordinates (u, v), points on the line $\overline{B_1A_{1\infty}}$ are identified by a single coordinate u since $v = 1$ on this line

$$\mathbf{x}(u) = \mathbf{x}_1(u, 1) \begin{cases} 0 \leq u \leq 1 & \mathbf{x}(u) \in \overline{B_1A_1} \\ 1 < u < \infty & \mathbf{x}(u) \in \overline{A_1A_\infty} \end{cases} \tag{2.51}$$

All trajectories originating from the line $\overline{B_1A_{1\infty}}$ remain in the $x - y$ plane, since this is the eigenspace $\Psi_1(E^c(P))$, spiraling inwards (in backward time) and hit the line $\overline{0N_1}$ a distance $X(u)$ from 0 after a specific time interval $\pi + arg(\mathbf{x}(u))$. We can rewrite this as

$$X(u) = |\mathbf{x}(u)|e^{-\sigma_1(\pi + arg(\mathbf{x}(u)))} \geq 0 \tag{2.52}$$

where

$$arg(\mathbf{x}) = \arctan\left(\frac{\mathbf{x}_y(u)}{\mathbf{x}_x(u)}\right). \tag{2.53}$$

It is shown in (Chua *et al.*, 1986) that the inverse return time functions $u^+(1, t)$ (2.38) and $u^-(1, t)$ (2.40) are both monotone functions and hence have an unique inverse. This means that every point

$X(u) \geq 0$ on the line $\overline{N_1 X(0)}$ maps uniquely into a point on $\overline{B_1 A_{1\infty}}$ via the flow φ_1^t, where $X(0)$ is the limiting point which maps into B_1. Any point d_1 between $X(0)$ and 0 must map into a point d_2 where

$$d_2 = e^{2\pi\sigma_1} d_1 \tag{2.54}$$

since it does not intersect the line $\overline{B_1 A_{1\infty}}$.
Each point on the line $\overline{B_1 A_{1\infty}}$ maps into one of the two spirals, defined by (2.33) and transformed into the D_1 unit as shown in figure 2.8 with coordinates $\mathbf{y}(u)$. It is also shown in (Chua *et al.*, 1986) that under the flow φ_1^t the point $\mathbf{y}(u)$ intersects with the plane W_1 with two spirales at coordinates

$$Y'(u) = \left(-|\mathbf{y}(u)| e^{\sigma_1(\pi - arg(\mathbf{y}(u)))},\ 0,\ \mathbf{y}_z(u) e^{\gamma_1(\pi - arg(\mathbf{y}(u)))} \right) \tag{2.55}$$

where

$$arg(\mathbf{y}) = \arctan\left(\frac{\mathbf{y}_y(u)}{\mathbf{y}_x(u)} \right). \tag{2.56}$$

If γ_1 is relatively large, the two spirales are squeezed into a thin line close to the line $\overline{N_\infty 0}$ and the points $Y'(u)$ can be approximated with points on the line $\overline{N_\infty 0}$ by

$$Y(u) = |\mathbf{y}(u)| e^{\sigma_1(\pi - arg(\mathbf{y}(u)))}, \quad 0 \leq u \leq \infty \tag{2.57}$$

To calculate the approximated Poincaré map (2.49) for $X(u) > X(0)$ we use

$$(X(u), Y(u)) = \left\{ \begin{array}{l} (X(u^+(1,t)), Y(u^+(1,t))), \quad 0 \leq t < \infty \ for\ 0 \leq u < 1 \\ (X(u^-(1,t)), Y(u^-(1,t))), \quad 0 < t < \infty \ for\ 1 \leq u < \infty \end{array} \right\} \tag{2.58}$$

For points between $X(0)$ and 0 we make use of (2.54)

$$Y(u) = e^{2\pi\sigma_1} X(u), \quad u < 0. \tag{2.59}$$

The approximated Poincaré (2.49) map can also be identified in figure 2.5. The point B' corresponds with $X(0)$. For each point $\mathbf{x} \in \overline{P^+ B'}$ the poincaré map is a linear map from $\overline{P^+ B'}$ onto $\overline{P^+ \pi^*(B')}$. For points $\mathbf{x} \in \overline{B' N_\infty}$, π^* is a nonlinear continuous map from $\overline{B' N_\infty}$ into $\overline{P^+ N_\infty}$.

2.4 1D Poincaré map

With the Poincaré map and a value for the variable resistor R the qualitative behavior of system (2.1) can be predicted, without explicitly integrating the equations. The approximated Poincaré map is given by (2.58) and (2.59) for a given parameter set. After the transient of (2.1) the behavior can be visualized by iterating this map.
An important point of the map is located at $X(1)$ which corresponds to the point A. If a trajectory starts at the line $\overline{BA}$, which is part of the triangular region (2.24), it does not intersect with the plane U_{-1}, see figure 2.6, and we call this trajectory a single scroll trajectory. If a trajectory starts at the line $\overline{AA_\infty}$, which is part of the wedge extension (2.29), the trajectory crosses the U_{-1} plane before it returns and is naturally called a double scroll trajectory. The 'birth' and 'death' of double scroll trajectories can therefore be explained using the Poincaré map.
To compare the approximated Poincaré map with the trajectories of (2.1) as in figure 2.3 the same resistor values are used to compute the maps. In figure 2.9 the map for $R = 1985$ [Ω] is shown. The boxed area in the upper left corner is a magnification of the rectangular box in the middle of the figure. Further the point $X(1)$ is located at $X = 1.1223$, indicated by a vertical dashed line. It can be seen that the map has a stable fixed point $X(u) = \pi^*(X(u)) = Y(u)$ to the left of the point $X(1)$. This means that a single scroll period one trajectory should occur, which is indeed the case in figure 2.3 (a). A single scroll period two solution, indicated by $X_2 = \pi^*(X_1)$, $X_1 = \pi^*(X_2)$ with X_1 and X_2 both to the left of $X(1)$ can be seen in figure 2.10. In figures 2.11 and 2.12 the existence of single scroll periodic solutions with period four and period three are visualized.
The transition from a single scroll to the double scroll, i.e. the 'birth' of the double scroll, is

shown in figure 2.13. With $R = 1942$ [Ω] the maximum value of Y on the interval [0 $X(1)$] is equal to X(1). This means that Y maps precisely through the boundary point A_1, if R is decreased further the point Y_{max} on the interval [0 $X(1)$] maps to the right of $X(1)$ and a double scroll scroll trajectory occurs.
Another special case is observed at $R = 1778$ [Ω], see figure 2.14. A double scroll trajectory occurs since Y_{max} on the interval [0 $X(1)$] is greater than $X(1)$, but the minimum value Y_{min} on the interval [$X(1)$ ∞] is equal to zero. This implies that the spiral $A'_{1\infty}C$ in figure 2.8 goes through the point D_1, because $Y = 0$. Recall from figure 2.6 that D_1 is the point on V_1 corresponding to the stable eigenvector $\Psi_1(E^r(P))$ of P^+. Therefore the double scroll trajectory goes through P and spirales outwards until it hits U_1, this is referred to as a hole-filling orbit.
A different periodic two limit cycle is shown in figure 2.15. Again $X_2 = \pi^*(X_1)$, $X_1 = \pi^*(X_2)$, but now $X_1 < X(1)$ and $X_2 > X(1)$. So we have one period of the limit cycle as a single scroll and the other period as the double scroll. This corresponds to the trajectory of figure 2.3 (g).
Finally in figure 2.16 the 'death' of the double scroll is visualized. Y_{max} on the interval [0 $X(1)$] maps to a second fixed point which corresponds to an unstable saddle-type closed orbit cycle, cf. (Chua *et al.*, 1986). When the attractor collides with the unstable closed orbit a boundary crisis (Grebogi *et al.*, 1982) occurs, resulting in the loss of the attractor (and its basin) and trajectories diverge to $\pm\infty$ for every initial condition.
Since this is physically impossible the model for the nonlinear resistor (2.2) could be extended with a second breakpoint $B_{p2} > B_p$ and a positive slope G_c to introduce passivity if $|v_1| > B_{p2}$,

$$f(v_1) = G_c v_1 + \frac{1}{2}(G_a - G_b)(|v_1 + B_p| - |v_1 - B_p|) + \frac{1}{2}(G_b - G_c)(|v_1 + B_{p2}| - |v_1 - B_{p2}|). \quad (2.60)$$

A new characteristic, with $B_{p2} = 13$ [V] and $G_c = 4.5$ [mS], is shown in figure 2.17. This has no effect on the actual attractor and the unstable closed orbit, because normally $|v_1| < B_{p2}$. However if the boundary crisis occurs the resulting trajectory is a large stable limit cycle, see (Matsumoto, 1984).

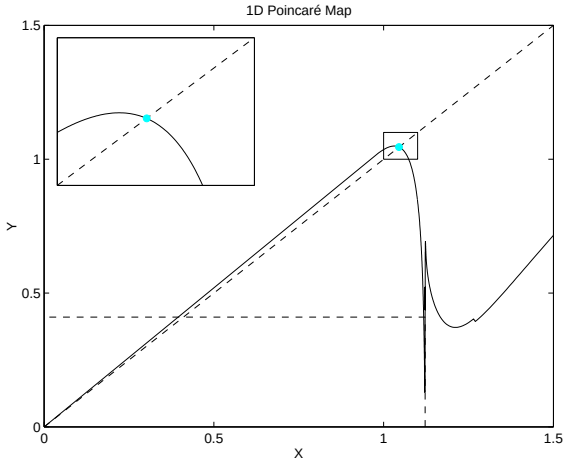

Figure 2.9: Period one limit cycle for $R = 1985$ [Ω].

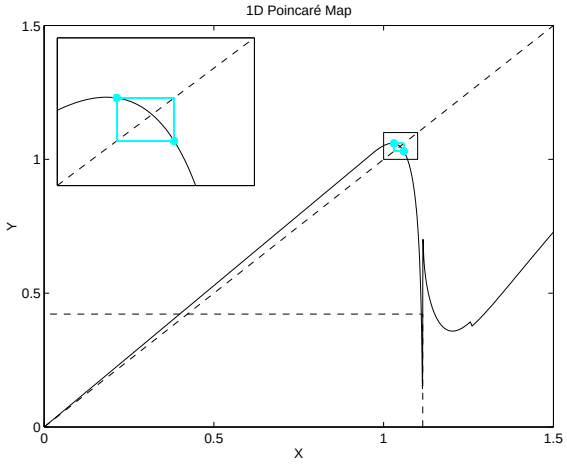

Figure 2.10: Period two limit cycle for $R = 1975$ [Ω].

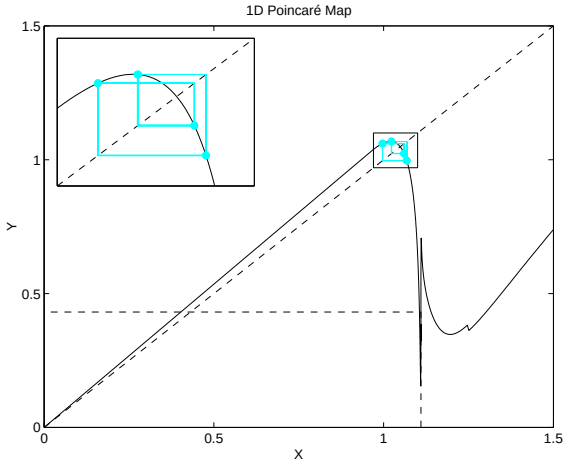

Figure 2.11: Period four limit cycle for $R = 1967$ [Ω].

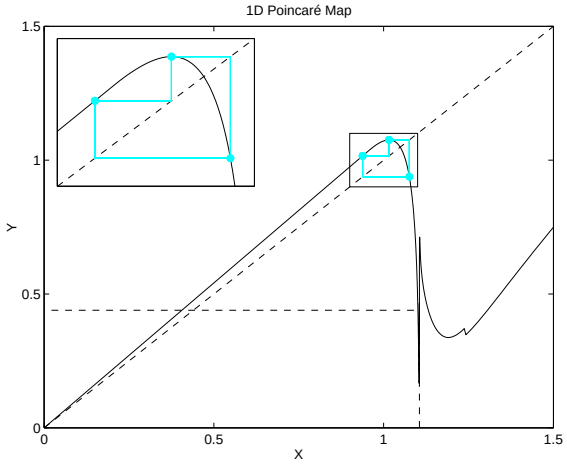

Figure 2.12: Period three limit cycle for $R = 1960$ [Ω].

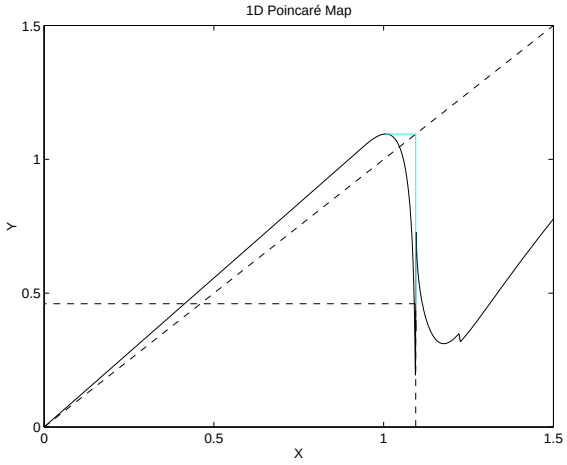

Figure 2.13: Birth of the double scroll for $R = 1942$ [Ω].

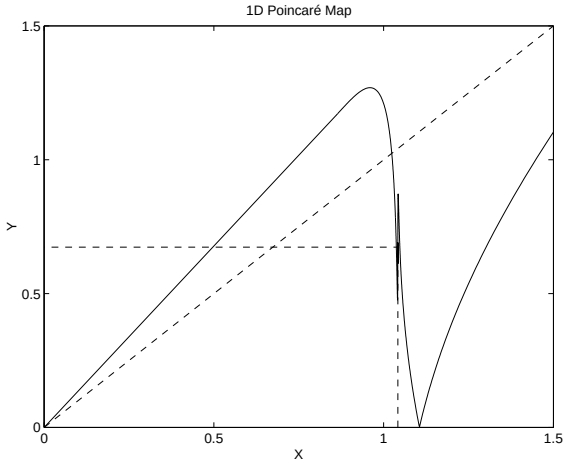

Figure 2.14: Hole-filling orbit for $R = 1778$ [Ω].

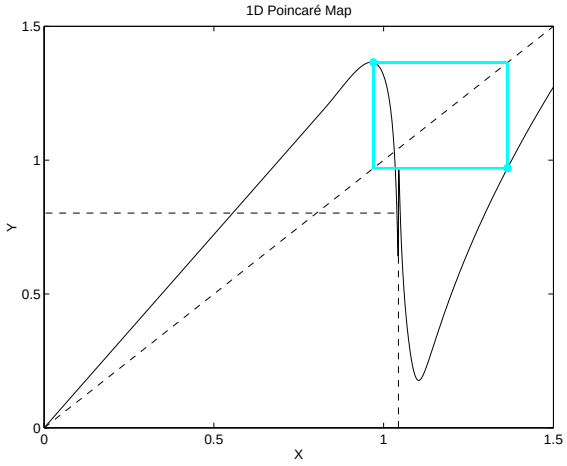

Figure 2.15: Double scroll period two limit cycle for $R = 1700$ [Ω].

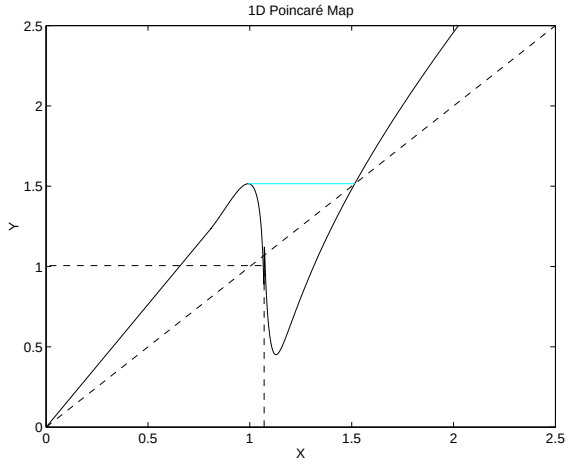

Figure 2.16: Death of the double scroll for $R = 1609$ [Ω].

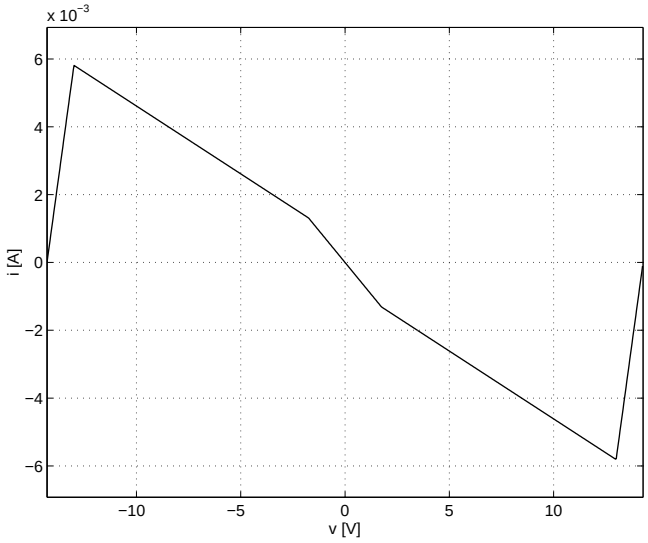

Figure 2.17: $v - i$ characteristic of the extended piecewise linear resistor.

2.5 Chaos

It is already mentioned that the Chua circuit is also capable of generating chaos. In this section the approximated Poincaré map is used to explain why chaotic behavior is possible in the circuit. In figure 2.18 another special case is shown. The point $X(1)$ is now a fixed point, i.e., it holds that $Y(1) = \pi^*(X(1)) = X(1)$. This implies that a trajectory which starts at the point A converges to the origin since it lies in the stable eigenspace of $E^c(0)$ and continues along the unstable eigenspace $E^r(0)$ until it hits the plane U_1 in point C, see figure 2.5. Point C corresponds to C_1 in figure 2.8 and since $Y(1) = X(1)$, the trajectory continuing from C_1 intersects the plane W_1 at $Y'(1)$, whose projection $Y(1)$ is equal to $X(1)$. This trajectory is a homoclinic orbit of the origin. A homoclinic orbit is an orbit which tends to a fixed point under backward iteration and lands on the same fixed point under forward iteration. This orbit plays a crucial role to show that the double scroll attractor is a chaotic system.

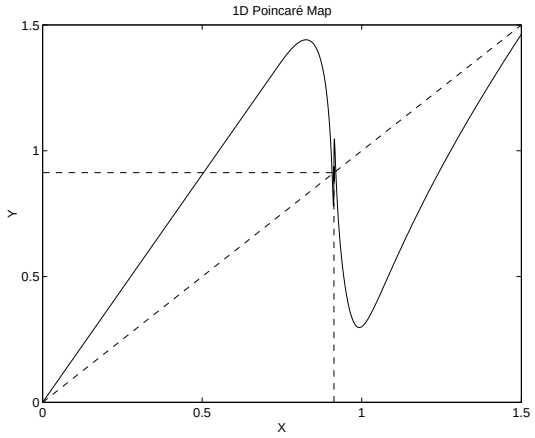

Figure 2.18: Homoclinic orbit for $R = 1635.7$ [Ω] and $G_b = -0.5$ [mS].

First we need to characterize chaos in such a way that it is easy to verify. Therefore we use the definition of chaos for discrete time dynamics as is given in (Devaney, 1986):
Let V be a set. $F : V \to V$ is said to be chaotic on V if

1. f has sensitive dependence on initial conditions.
2. f is topologically transitive.
3. periodic points are dense in V.

If a system has sensitive dependence on initial conditions than initially nearby points can evolve quickly into very different states. This implies that a chaotic system is unpredictable.
A function $f : J \to J$ is said to be topologically transitive if for any pair of open sets $U, V \subset J$ there exists $k > 0$ such that $f^k(U) \cap V \neq \emptyset$, i.e., since the intersection is a non-empty set some points from U, under iteration, intersect with the set V. So a dynamical system, which is topologically transitive, cannot be decomposed into two disjoint open sets which are invariant under the map. Therefore it is not possible to decompose a chaotic system into two subsystems.
However there is still regular behavior possible in a chaotic system since the periodic points are dense in V.

To verify that system (2.1) is chaotic we make use of a theorem posed by Šilnikov, cf. (Guckenheimer and Holmes, 1983; Silva, 1993).
Šilnikov considered a three dimensional flow, containing a homoclinic trajectory to a saddle point,

see figure 2.19.
Under the condition that the real eigenvalue (γ) has larger magnitude than the real part of the complex eigenvalues ($\sigma \pm j\omega$), there are horseshoes present in the return maps defined near the homoclinic orbit. The proof for this can be found in (Guckenheimer and Holmes, 1983).

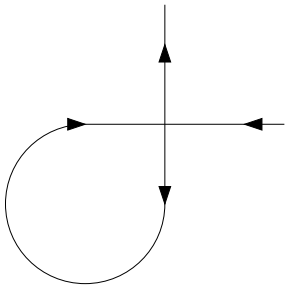

Figure 2.19: Abstraction of a homoclinic orbit to a saddle point.

The horseshoe is an example of a hyperbolic limit set (Guckenheimer and Holmes, 1983). The Smale horseshoe map is defined by the map $f : S \to \mathbb{R}^2$, where $S = [0,1] \times [0,1]$ is the unit square in the plane, shown in figure 2.20.

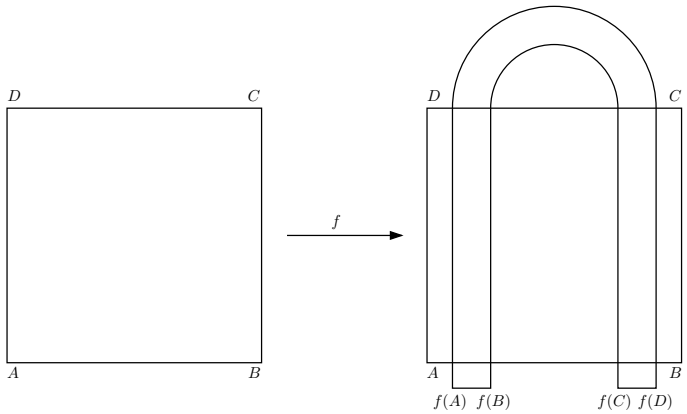

Figure 2.20: Abstraction of the Smale horseshoe map.

If f is iterated most points leave S, however the points that remain in S for all time form a set $\Lambda = \{x | f^i(x) \in S, -\infty < i < \infty\}$. This set is a Cantor set, see (Devaney, 1986). The horseshoe map has the following properties (Guckenheimer and Holmes, 1983):
The map f has an invariant Cantor set Λ such that:

1. Λ contains a countable set of periodic orbits of arbitrarily long periods.
2. Λ contains an uncountable set of bounded nonperiodic motions.
3. Λ contains a dense orbit.

Now we are able to verify that the double scroll is indeed chaotic. There exists a parameter set such that there is a homoclinic orbit through the origin, (see figure 2.18), further it holds that $|\sigma_0| < \gamma_0$ and therefore Šilnikovs conditions hold. The points two and three in the definition of a chaotic system follow directly from the Cantor set Λ, (since Λ contains a dense orbit it is also topologically transitive (Devaney, 1986)). It remains to verify that system (2.1) is sensitive to

initial conditions.
We try to demonstrate this through a simulation. System (2.1) is integrated twice with slightly different initial conditions. In the first simulation the initial conditions are chosen as $[1\ 1\ 0]^T$, for the second simulation the initial condition is chosen as $[1+1\cdot10^{-11}\ 1\ 0]^T$. The results for the first state, v_1, are shown in figure 2.21. After $t = 0.012$ it is visible that the solutions diverge. This shows that system (2.1) is sensitive to initial conditions.
Another property indicating chaos in system (2.1) is the existence of the period three limit cycle as shown in figure 2.12, see (Šarkovskii, 1964; Li and Yorke, 1975).

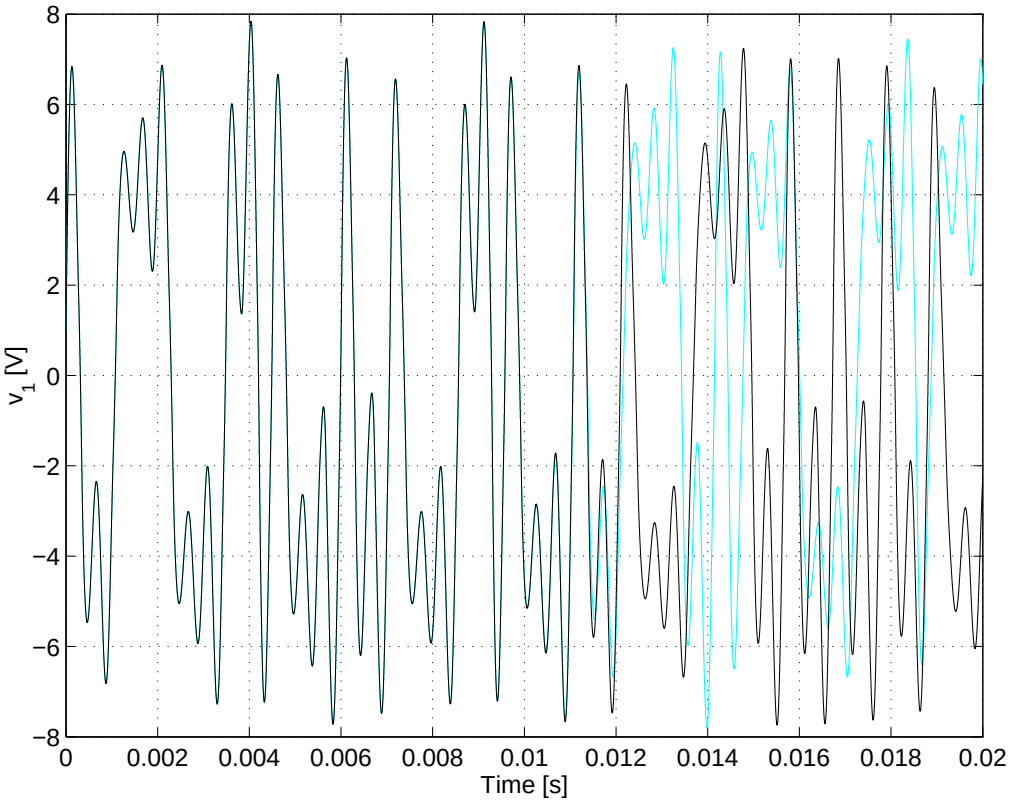

Figure 2.21: Time signals for v_1 of both simulations.

Chapter 3

Building and identification of a Chua circuit

In this chapter the electrical realization of model (2.1) is presented. The different aspects of this realization are explained. After the design the identification of the circuit is described. Different identification methods are compared and the results are discussed.

3.1 Realization

Consider again the schematic circuit in figure 3.1. The circuit basically consists of two capacitors, an inductor, a variable resistor and the so-called negative resistor. In the next paragraphes the actual electronic counterparts of the schematic components are introduced. The main part of the layout of the circuit is based on the methodology presented in (Kennedy, 1992). The nominal values of the electronic components are chosen to match with the parameter values in table 2.1.

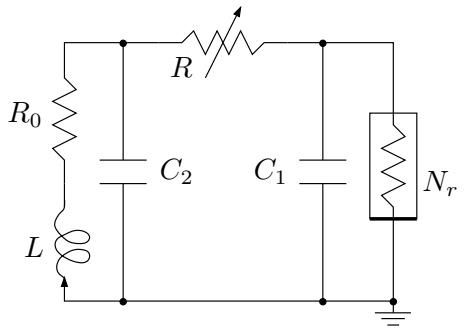

Figure 3.1: Schematic layout of a Chua circuit.

3.1.1 Variable resistor and capacitors

The variable resistor, R, is composed of a precision metal film resistor with a nominal value of 1500 [Ω] and a precision potentiometer with a range from $0 - 500$ [Ω]. In this way the variable resistor is more accurate in the region of interest. The dielectric capacitors C_1 and C_2 are chosen with nominal values of 0.01 [μF] and 0.1 [μF] respectively.

3.1.2 Nonlinear resistor

There are several ways to obtain the piecewise linear function, $f(v_1)$ (2.2), using electronic components, e.g. using transistors (Matsumoto *et al.*, 1986), operational amplifiers (Op Amps) (Kennedy, 1992) or operational transconductance amplifiers (Cruz and Chua, 1992). In this design the nonlinear resistor is constructed with operational amplifiers and resistors.
A negative resistance can be synthesized using three normal positive resistances and a voltage-controlled voltage source (VCVS). A VCVS is an ideal circuit element with two important properties: The voltage at the output is a linear function of the potential difference at the input and no current flows in, or out, the input terminals. Since a VCVS is an ideal circuit element an Op Amp is used as an approximation of a VCVS. The output of an Op amp depends linearly on the potential difference V_d at the input, however the output V_o of an Op Amp saturates when the absolute difference of the input crosses a threshold voltage. This can be seen in figure 3.2, it is assumed that there is no voltage offset ($V_d = 0\ [V] \mapsto V_o = 0\ [V]$). When the resistors are connected as shown in figure 3.3 the following relations (Kennedy, 1992) hold

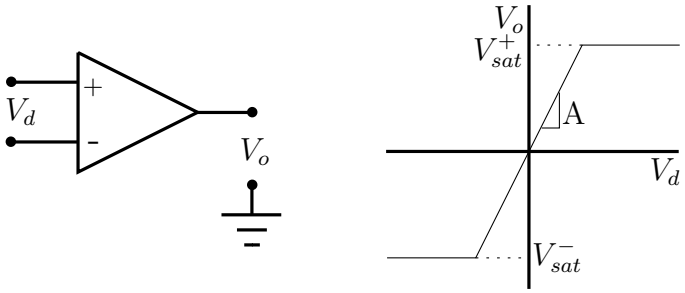

Figure 3.2: Operational Amplifier and voltage transfer characteristic.

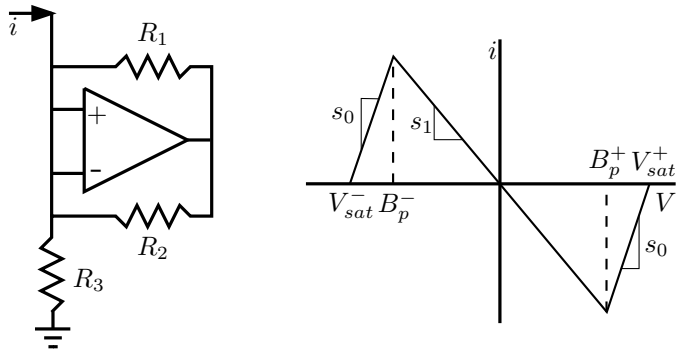

Figure 3.3: Negative resistor converter and $v - i$ characteristic.

$$s_0 = \frac{1}{R_1} \tag{3.1}$$

$$B_p^+ = \frac{R_2 + (1+A)R_3}{A(R_2+R_3)} V_{sat}^+ \tag{3.2}$$

$$s_1 = \frac{(1-A)R_2 + R_3}{R_1[R_2 + (1+A)R_3]} \tag{3.3}$$

$$B_p^- = \frac{R_2 + (1+A)R_3}{A(R_2+R_3)} V_{sat}^-, \tag{3.4}$$

where A is the gain of the Op Amp and V_{sat} the saturation voltage.
When the gain A is large and R_2 is equal to R_1 these equations can be approximated by

$$s_0 = \frac{1}{R_1} \tag{3.5}$$

$$B_p^+ \approx \frac{R_3}{R_2 + R_3} V_{sat}^+ \tag{3.6}$$

$$s_1 \approx -\frac{1}{R_3} \tag{3.7}$$

$$B_p^- \approx \frac{R_3}{R_2 + R_3} V_{sat}^-. \tag{3.8}$$

It follows from figure 3.3 that as soon as the voltage exceeds B_p the resistance becomes positive. This prevents that after the 'death' of the double scroll the voltage becomes unbounded.
When two negative resistors are connected in parallel the piecewise-linear resistor (2.2) is obtained.

3.1.3 Inductor

The inductor in the circuit is constructed using resistors, an Op Amp and a capacitor. With these components it is possible to synthesize an inductor. The inductor used in a previous realization (Hees, 2004) did not give satisfactory results, therefore a different layout is used. This new layout is shown in figure 3.4 and based on the work of (Pegna *et al.*, 2000). Under the assumption that the gain $A \to \infty$, the value of L can be approximated by

$$L \approx C_3 R_0 (R - R_0) \tag{3.9}$$

where R_0 acts as the internal resistance of the inductor.

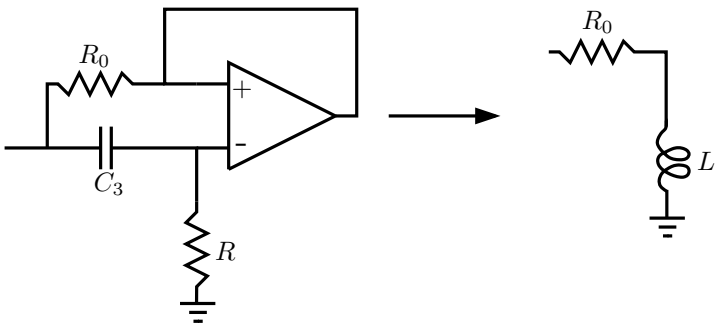

Figure 3.4: Inductor layout.

3.1.4 Total circuit

With the parts described in the previous sections the complete circuit can be realized. However some additional components are used to be able to measure the voltage across the two capacitors C_1 and C_2. In order to use data acquisition devices, such as Siglab, or other electronic devices (loudspeakers or other Chua circuits) without influencing the circuit itself so-called voltage followers are added. A practical addition are two 'jumpers' that divide the circuit into three separate subsystems. In this way it is possible to measure only the nonlinear resistor or a resonance circuit consisting of the inductor L and capacitor C_2. Another practical addition are bypass capacitors connected across the power supplies of the Op Amps to maintain a steady DC voltage. The complete realization can be seen in figure 3.5. The circuit layout with component list can be found in appendix B.

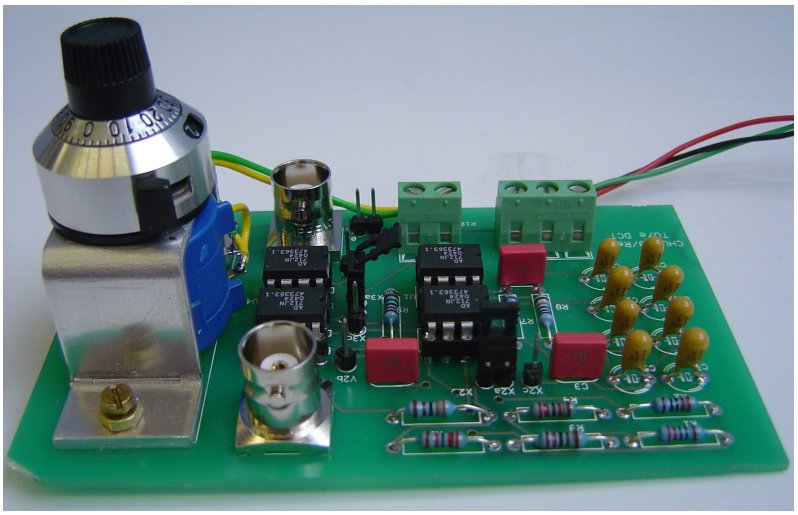

Figure 3.5: Realization of Chua circuit.

3.2 Identification using measurements

3.2.1 Variable resistor and capacitors

The variable resistor is measured using a standard multi-meter. A linear characteristic is assumed and approximated by a least square estimate

$$R = 49.3(turn + number/100) + 0.8. \tag{3.10}$$

The turn is the number of rotations of the potentiometer (0-10) and number is the scale division

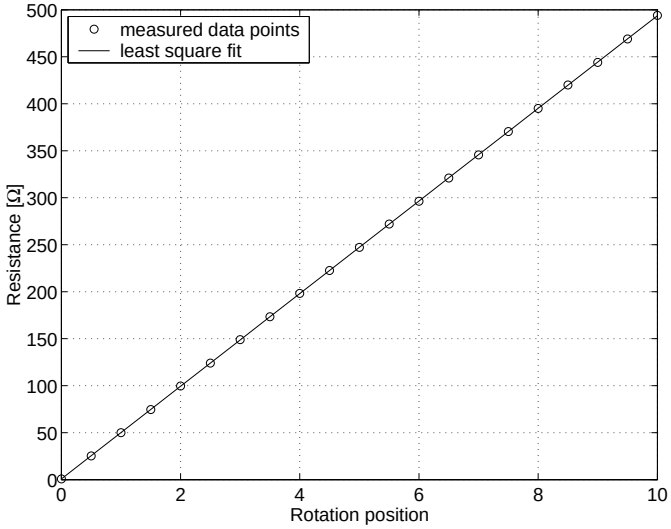

Figure 3.6: Characteristic of the variable resistor.

(0-100) in one turn.
The capacitors C_1, C_2 and C_3 are measured with a Fluke RCL meter before assembly and con-

sidered fixed hereafter.

$$C_1 = 10.90\ [nF] \tag{3.11}$$
$$C_2 = 97.93\ [nF] \tag{3.12}$$
$$C_3 = 10.92\ [nF] \tag{3.13}$$

3.2.2 Nonlinear resistor

By removing one of the jumpers the nonlinear resistor part can be isolated from the total circuit. To measure the current through the nonlinear resistor a differential amplifier ($AD620$) in combination with a resistor R_m is used. With the amplified voltage over the resistor R_m and using Ohm's law it is possible to obtain the $v - i$ characteristic. A sinusoidal signal is used as input. Several experiments are performed and averaged to determine the positive and negative breakpoints as well as the slopes G_a and G_b. The main observation is that the slopes G_b in the positive and negative parts are equal. Furthermore there is a little difference between the breakpoints. This is due to different saturation points for positive and negative voltages of the used operational amplifiers.
One of the disadvantages of this measuring method is that the slopes are very sensitive to the total amplification factor, which consists of the differential amplifier itself times the value of R_m. The values in table 3.1 are determined using a (ideal) total amplification factor of 100. The theoretical values for G_a and G_b are -0.7591 [mS] and -0.4096 [mS] respectively.
Another interesting phenomenon is illustrated in figure 3.8. It seems that there is some sort of hysteresis present in the nonlinear resistor, although this is investigated further in (Criens, 2005; Wouters, 2005) no specific explanation is found.

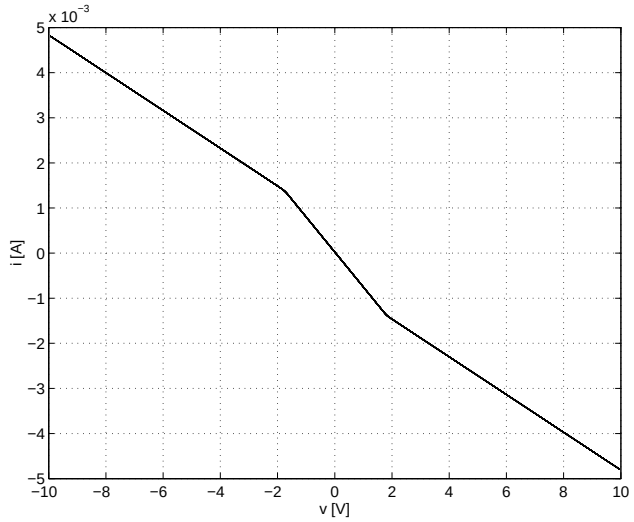

Figure 3.7: Measured characteristic of the nonlinear resistor with a 30 [Hz] sinusoidal input.

Table 3.1: Parameters for the nonlinear resistor.

Parameter	Value	Parameter	Value
G_a	-0.7665 [mS]	Bp^+	1.81 [V]
G_b^+	-0.4119 [mS]	Bp^-	-1.75 [V]
G_b^-	-0.4119 [mS]		

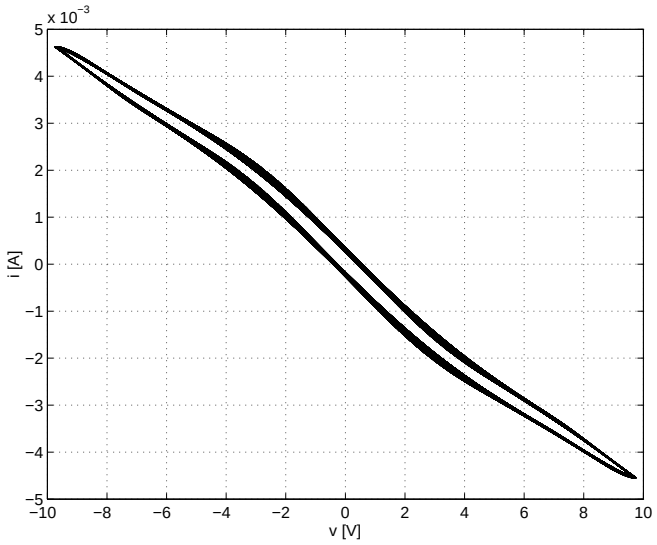

Figure 3.8: Measured characteristic of the nonlinear resistor with a 3500 [Hz] sinusoidal input.

3.2.3 Inductor

The theoretical values, based on the used components and (3.9), are 0.0245 $[H]$ for the inductor and 22.40 $[\Omega]$ for the internal resistance R_0.
By removing the other jumper a resonance circuit is created, which makes it possible to perform a frequency response measurement.
The resonance circuit is shown in figure 3.9, where V_{in} and V_{out} are measured. V_{out} is used as measurement for the current through the circuit. We assume again that the total amplification factor is equal to 100, which gives the following relation for the total impedance of the resonance circuit

$$Z = \frac{V_{in}}{I_{in}} \approx 100 \frac{V_{in}}{V_{out}}. \tag{3.14}$$

The theoretical impedance is given by

$$Z = \frac{(R_0 + j\omega L)\,\frac{1}{j\omega C_2}}{R_0 + j\omega L + \frac{1}{j\omega C_2}} + R_m \tag{3.15}$$

$$Z = \frac{C_2 L R_m s^2 + (L + R_m C_2 R_0)\, s + R_0 + R_m}{C_2 L s^2 + C_2 R_0 s + 1}. \tag{3.16}$$

Under the assumption that C_2 is known, we can fit a frequency response function and use the denominator of (3.16) to calculate L and R_0. In this way the effect of the amplification factor is canceled since a gain only affects the nominator. The frequency response function is shown in figure 3.10 and the values for L and R_0 are given in table 3.2.

Table 3.2: Parameters for the inductor.

Parameter	Value
L	0.0243 [H]
R_0	37.29 [Ω]

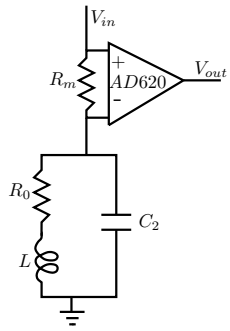

Figure 3.9: Resonance circuit.

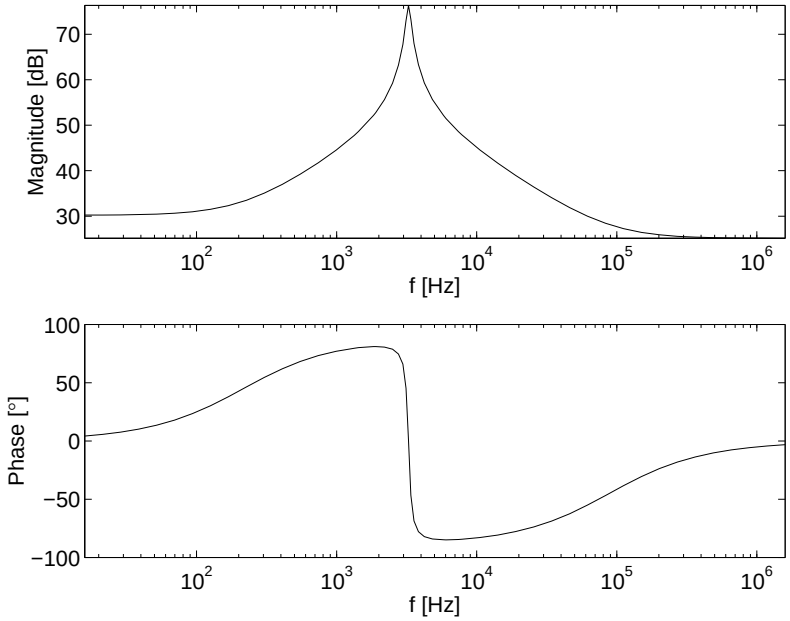

Figure 3.10: Frequency response function.

3.3 Identification using filtering

A popular technique to estimate states (and parameters) in the presence of measurement (and system) noise is Kalman filtering. Kalman filters for linear systems produce optimal - i.e., the filter minimizes the variance of the difference between actual and estimated state - unbiased and consistent estimations of the systems states. Kalman filters can also be applied to nonlinear systems and are known as Extended Kalman filters. The main drawback of an extended filter is however that the filter is not anymore optimal in the above sense.

3.3.1 Augmented Continuous-Discrete filter

To identify the state of the double scroll circuit some remarks must be made. The differential equations are continuous in time, while measurements can only be taken at discrete times. This means that a continuous model is needed to estimate the states between measurements and a discrete update law should be used whenever a new measurement is available. This can be done by using a so-called continuous-discrete Kalman filter.

3.3.2 Parameters

Besides the states also some parameters are not accurately known, e.g. the slopes of the nonlinear resistor and the internal resistance R_0 of the inductor. The value of the variable resistor R can be measured, however internal resistances of the print board itself are unknown. Since R is used as bifurcation parameter we want to know its value as accurate as possible. Therefore this parameter should be estimated as well.
The nonlinear resistor is characterized by the slopes, G_a, G_b^+ and G_b^- and the breakpoints B_p^+ and B_p^-. We assume that the breakpoints are fixed, while the slopes cannot be measured accurately enough due to uncertainties in the measurement device. Therefore the state $\mathbf{x}$ is augmented to $[v_1\ v_2\ i\ G\ R_0\ -G_a^-\ -G_b^+\ -G_b^-]^T$ where $G = \frac{1}{R}$.

3.3.3 Algorithm

In this section the filter algorithm, based on (Gelb, 2001), is summarized. We start with a system and measurement model given by

$$\begin{aligned} \dot{\mathbf{x}}(t) &= f(\mathbf{x}(t), t) + \mathbf{w}(t) && \mathbf{w}(t) \sim N(0, Q(t)), && (3.17)\\ \mathbf{z}_k &= \mathbf{h}_k(\mathbf{x}(t_k)) + \mathbf{v}_k \quad k = 1, 2, \ldots && v_k \sim N(0, R_k), && (3.18)\\ t_k &= k\Delta t && && (3.19) \end{aligned}$$

where Δt is the time between sample k and $k+1$. $\mathbf{w}(t)$ and $\mathbf{v}_k$ represents the process and measurement noise respectively. In absence of information about this noise, it is assumed to be white noise with zero mean and a normal distribution. The covariance matrices of the process and measurement noise are $Q(t)$ and R_k. In the ideal case, having a perfect model and no measurement noise, $\mathbf{w}(t)$ and $\mathbf{v}_k$ are absent.
The state estimation and error covariance propagation are as follows

$$\begin{aligned} \dot{\hat{\mathbf{x}}}(t) &= f(\hat{\mathbf{x}}(t), t), && (3.20)\\ \dot{P}(t) &= F(\hat{\mathbf{x}}(t), t)P(t) + P(t)F^T(\hat{\mathbf{x}}(t), t) + Q(t), && (3.21) \end{aligned}$$

where $\hat{\mathbf{x}}$ is the filtered estimate of $\mathbf{x}$ and $F(\hat{\mathbf{x}}(t), t)$ is the Jacobian matrix defined as

$$F(\hat{\mathbf{x}}(t), t) = \left.\frac{\partial f(\mathbf{x}(t), t)}{\partial \mathbf{x}(t)}\right|_{\mathbf{x}(t)=\hat{\mathbf{x}}(t)}. \tag{3.22}$$

The covariance matrix $P(t)$ is a symmetric matrix representing an approximation of the true covariance.
When a new measurement is available the state estimation and error covariance matrix are updated using the following update laws

$$\begin{aligned} \hat{\mathbf{x}}_k(+) &= \hat{\mathbf{x}}_k(-) + K_k[\mathbf{z}_k - h_k(\hat{\mathbf{x}}_k(-))], && (3.23)\\ P_k(+) &= [I - K_k H_k(\hat{\mathbf{x}}_k(-))]P_k(-), && (3.24)\\ K_k &= P_k(-)H_k^T(\hat{\mathbf{x}}_k(-))[H_k(\hat{\mathbf{x}}_k(-))P_k(-)H_k^T(\hat{\mathbf{x}}_k(-)) + R_k]^{-1}, && (3.25) \end{aligned}$$

where $\hat{\mathbf{x}}_k(-)$ is the estimate of $\mathbf{x}(t)$ at time t_k before measurement $\mathbf{z}_k$ is taken into account and $\hat{\mathbf{x}}_k(+)$ is the estimation at time t_k after this measurement. K_k is the gain matrix and I is the identity matrix. $P_k(-)$ and $P_k(+)$ are the discrete error covariance before and after the update. $H_k(\hat{\mathbf{x}}_k(-))$ is the Jacobian matrix defined as

$$H_k(\hat{\mathbf{x}}_k(-)) = \left.\frac{\partial h_k(\mathbf{x}(t_k))}{\partial \mathbf{x}(t_k)}\right|_{\mathbf{x}(t_k)=\hat{\mathbf{x}}_k(-)}. \tag{3.26}$$

The following model for the electric circuit is used (see chapter 2)

$$\begin{aligned} C_1\dot{v}_1 &= G(v_2 - v_1) - f(v_1)\\ C_2\dot{v}_2 &= G(v_1 - v_2) + i_L && (3.27)\\ L\dot{i}_L &= -v_2 - R_0 i_L, \end{aligned}$$

which can be divided into three linear parts by writing out $f(v_1)$:

$$\begin{aligned} v_1 &\geq B_p^+ \\ C_1\dot{v}_1 &= G(v_2 - v_1) - (G_b^+ v_1 + (G_a - G_b^+)B_p^+) \end{aligned} \tag{3.28}$$

$$\begin{aligned} B_p^- &< v_1 < B_p^+ \\ C_1\dot{v}_1 &= G(v_2 - v_1) - G_a v_1 \end{aligned} \tag{3.29}$$

$$\begin{aligned} v_1 &\leq B_p^- \\ C_1\dot{v}_1 &= G(v_2 - v_1) - (G_b^- v_1 + (G_a - G_b^-)B_p^-) \end{aligned} \tag{3.30}$$

The advantage of this model, compared to the dimensionless model (2.11), is that a measurement sample can be used directly, whereas the dimensionless time τ depends on the parameter R, which is to be estimated.
Since the piecewise linear model consists of three different linear systems the Jacobian of $f(\mathbf{x}(t), t)$ (3.22) is not continuous and a modification is required. There are multiple ways to solve the Ricatti equation (3.21).
In the next section we introduce an extension of a 'switching' Kalman filter as presented in (Cruz and Nijmeijer, 2000; Cruz *et al.*, 2001). Although this filter switches between linear parts it is not an optimal filter. Three different methods will be used and compared.

3.3.4 Methods

The first method consists of one Ricatti equation. Although the linearization of $f(\hat{\mathbf{x}}(t), t)$, see (3.27), is evaluated at the current state of the system, it gives three different Jacobian matrices depending on the state v_1. This gives a 'jump' in the Ricatti equation.
Instead of one Ricatti equation, three Ricatti equations can be used to prevent the jump. There are two ways to solve these equations. One way, method 2, is to solve all three equations at the same time and chose the right update gain vector, which depends on the state v_1, to update the state. The Ricatti equations are updated using the three different gain vectors. The problem here is however that the linearization of $f(\hat{\mathbf{x}}(t), t)$ is not a good approximation for two of the three regions. Therefore the update for two Ricatti equations is not correct.
The other way, method 3, is to integrate the system and just one Ricatti equation between two samples. Then update this Ricatti equation and holding the other two at their previous values. Now the linearization of $f(\hat{\mathbf{x}}(t), t)$ is correct, but the Ricatti equations are not continuous in time anymore.

3.3.5 Results

To compare the three methods one data set is used and the settings for Q and R_k are kept constant. The results can be seen in figure 3.11. In this figure a part of a measured time signal of v_1 together with the errors between measurement and estimation for the three methods is shown. In the unstable area, the area between the two horizontal lines in the measured time signal, the error remains large compared to the stable regions. In table 3.3 the RMS value of the error is given. It can be seen that the three Ricatti equations perform a little bit better. For the filter, where one Ricatti equation is solved between two samples, the obtained parameters are presented in table 3.4.

3.4 Comparison filters for measurement and process noise

3.4.1 Measurement noise

To compare the two filters with the three Ricatti equations we investigate the influence of different levels of measurement and process noise. For the measurement noise a diagonal matrix $R_k = diag([R_1\ R_2])$ is used. To compare the influence different values for R_k are evaluated ranging from 1^{-8} till 1^{-4}. The comparison is made by using the 2 and infinity norm of the error between measurement and prediction of v_1. It can be seen in the figure 3.12 that if R_k is too small the measurements are not considered reliable, also the filter is not stable anymore.
When R_k is too big, the filter tries to follow all measurement samples and the model information is ignored. There seems to be an optimum around $R_k = 1^{-6}$. For all simulations the process noise is chosen as $Q = diag([1^{-5}\ 1^{-5}\ 1^{-5}\ 0\ 0\ 0\ 0\ 0])$.

3.4.2 Process noise

To see the influence of process noise on the differential equations Q is varied, while the process noise for the parameter equations is set to zero. R_k is chosen as $R_k = diag([1^{-6}\ 1^{-6}])$ in this case. It follows that if there is too much process noise the model is not considered reliable and again the filter tries to follow every measurement sample.

3.5 Discussion

The described identification methods can be used to obtain values for the parameters. Several simple experiments are used to determine parameters of different parts of the circuit. Further three Kalman filters are used to estimate parameters based on measurements of the whole circuit. However if the obtained parameters from measurements or the Kalman filter are used in a numerical simulation, the solution always differs from experimental data. There are several reasons why this happens. We know that system (2.1) is a chaotic system and is therefore sensitive to parameter values. The initial condition of the current is unknown, which also plays an important role in the final trajectory and the tolerances of the used solver cause unwanted rounding errors.
An illustrative example is visualized in figure 3.14. To give an explanation of the radical difference in figure 3.14 we take a closer look at the experiment and the Kalman filter. If we look at one period of the periodic solution, see figure 3.15, it can be seen that the error in the two outer regions is relatively small compared to the error in middle region, especially when the trajectory goes from left to right or visa versa.
However there is always a nonzero error and this means that trajectories will always diverge from a measured trajectory if we do not use measurement data to correct the computed numerical trajectory.
The closed orbit shown in figure 3.14 is not robust to parameter variations and therefore it is practically impossible to obtain this periodic solution by numerical integration of system (2.1). The result is the trajectory as shown in figure 3.14 (c).
So we need measurement information to follow experimental trajectories and therefore we end this chapter with some remarks about the Kalman filter. It is already mentioned that the error in the two outer regions is smaller than the error in middle region. This indicates that results obtained by the Kalman filter might improve if the model for the region $B_p^- < v_1 < B_p^+$ is changed. There is a very small current offset at zero volt in the measured nonlinear resistor, see figure 3.7, which is not modeled. Further we approximated the location of the breakpoints by averaging several experiments and used this as the switching between the three regions. A filter that is capable of estimating the breakpoints (see (Santoboni and Nijmeijer, 2001)) could improve the results as well.
Finally, and probably the most important, the dynamic behavior of the electric components is neglected in the used model (3.27). The influence of the operational amplifiers is already pointed out in (Kennedy, 1992). This can be investigated further by performing circuit simulations, such

as SPICE (Quarles *et al.*, 1993).
In the next chapters we will focus more on the qualitative behavior instead of the quantitative behavior.

Table 3.3: Root mean square values of the error signals.

Method 1	Method 2	Method 3
0.0464 [V]	0.0320 [V]	0.0262 [V]

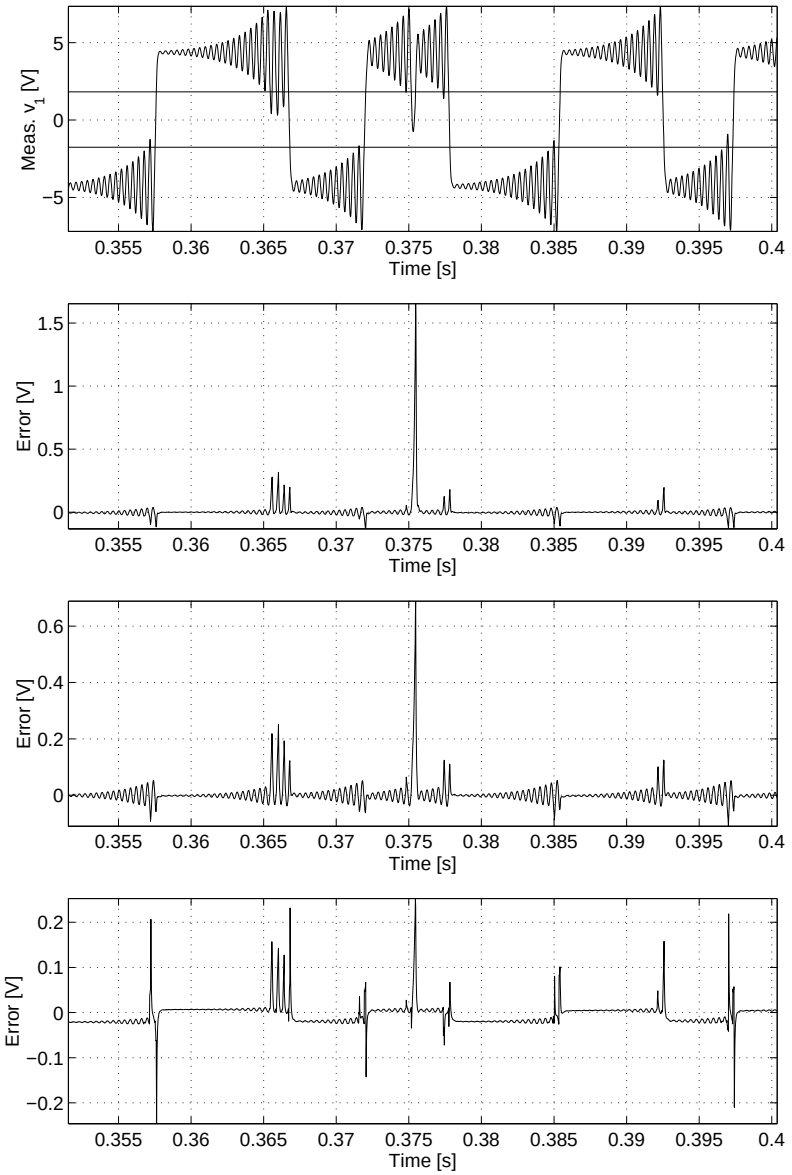

Figure 3.11: Experimental data and error between measurement and estimation of v_1 for the three methods. The first error is for one Ricatti equation. The second error is obtained by solving all three Ricatti equations at once. The last error plot is obtained by solving one Ricatti equation between two samples.

Table 3.4: Parameters obtained by Kalman filter, std stands for the standard deviation.

Parameter	Mean value	std
R_0	25.70 [Ω]	0.20 [Ω]
G_a	-0.7385 [mS]	0.0049 [mS]
G_b^+	-0.4018 [mS]	0.0013 [mS]
G_b^-	-0.4020 [mS]	0.0024 [mS]

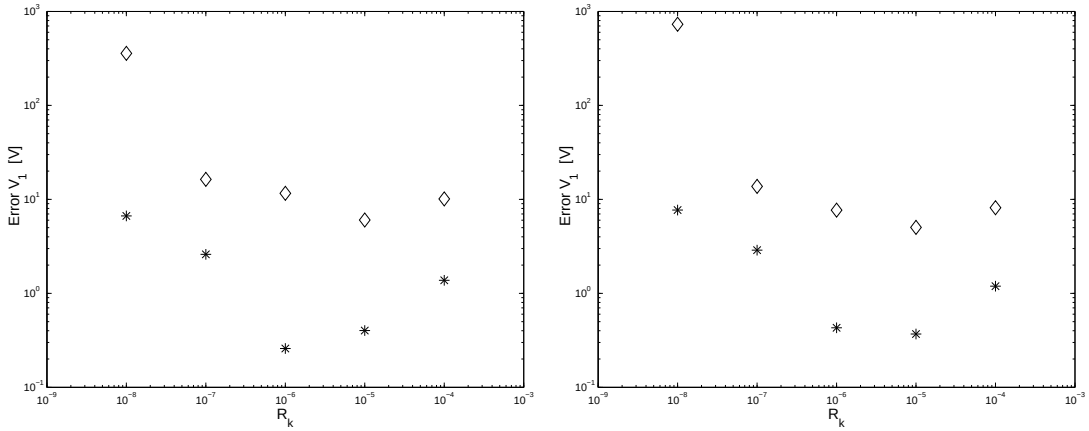

(a) 3 Ricatti-equations, continuous in time.
$\diamondsuit = \|Error\ v_1\|_2,\ * = \|Error\ v_1\|_\infty$

(b) 3 Ricatti-equations, discontinuous in time.
$\diamondsuit = \|Error\ v_1\|_2,\ * = \|Error\ v_1\|_\infty$

Figure 3.12: Influence of measurement noise levels.

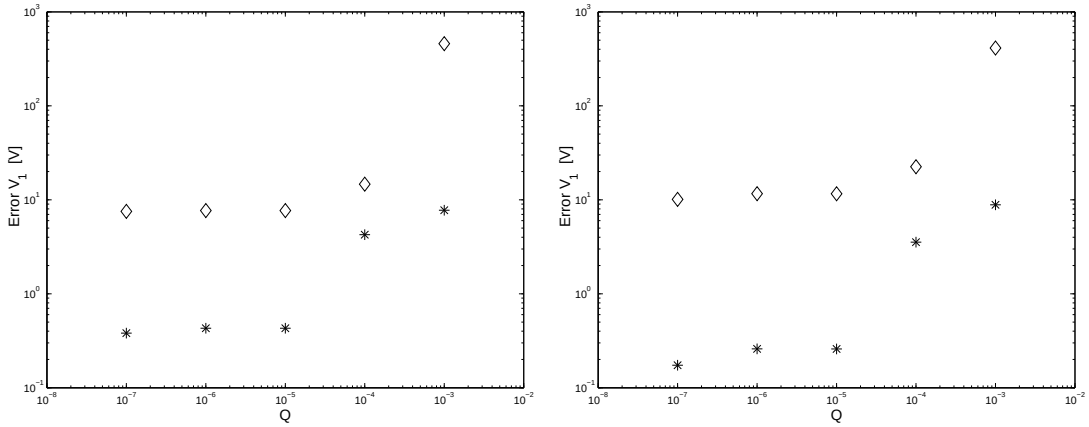

(a) 3 Ricatti-equations, continuous in time.
$\diamondsuit = \|Error\ v_1\|_2,\ * = \|Error\ v_1\|_\infty$

(b) 3 Ricatti-equations, discontinuous in time.
$\diamondsuit = \|Error\ v_1\|_2,\ * = \|Error\ v_1\|_\infty$

Figure 3.13: Influence of process noise levels.

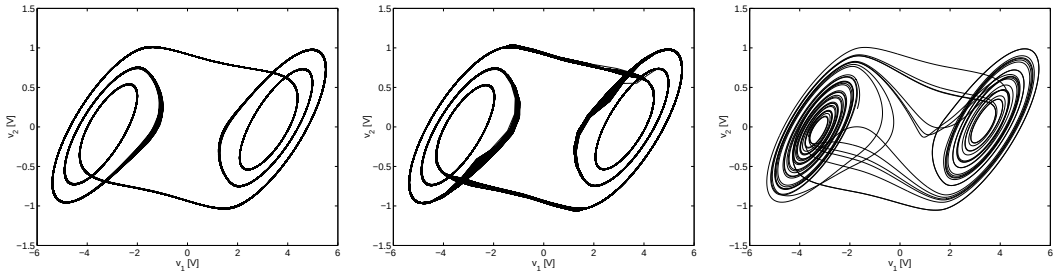

(a) Experiment. (b) Kalman filter. (c) Simulation.

Figure 3.14: Difference between experiment, Kalman filter and simulation.

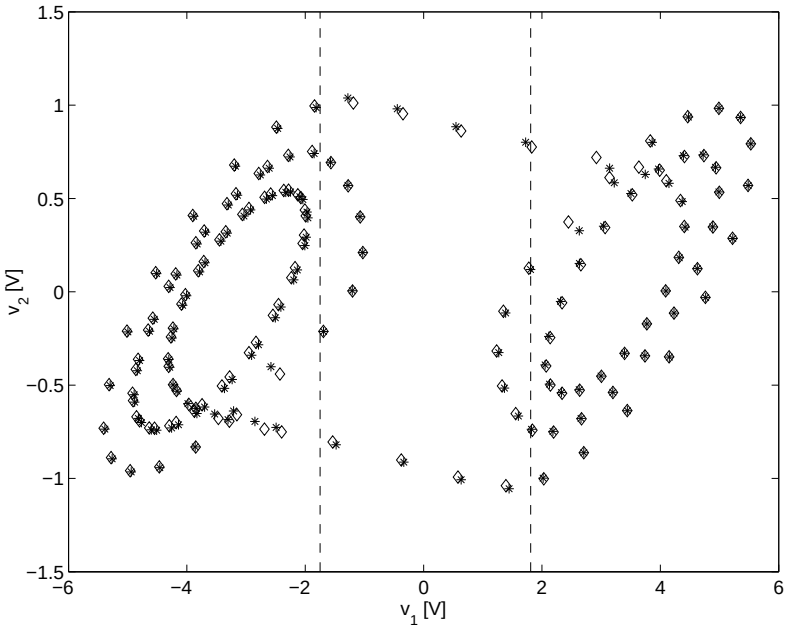

Figure 3.15: $\diamondsuit$ indicate measured data points and $*$ indicate filtered data.

Chapter 4

Experiments

With the electronic realization as described in the previous chapter several experiments are conducted. In this chapter the qualitative numerical results obtained in chapter 2 are validated experimentally. For the experiments the same approach as in chapter 2 is followed. This means we start at $R \approx 2000$ [Ω] and then decrease the resistor value. The value of R is obtained by the number of rotations of the potentiometer and using (3.10).

4.1 Single scroll trajectories

One of the disadvantages of the setup is that is not possible to choose initial conditions. The setup is initialized when the voltage supply of the operational amplifiers is turned on. Although the initial conditions are random, often the voltage across capacitor C_1 is negative. Therefore we present the single scroll solutions only for negative voltages v_1. However all solutions are also observed for positive v_1.
The bifurcation point at which the stable equilibrium point loses its stability occurs at $R \approx 1902$ [Ω]. In figure 4.1 projections of v_2 versus v_1 can be seen. In these figures the trajectories intersect with each other due to the projection of the three dimensional state space on the $v_1 - v_2$ plane. The projection of the period three limit cycle is probably the most interesting, since this is a strong indication that the experimental setup is capable of generating chaos.
The 'birth' of the double scroll occurs at $R \approx 1823$ [Ω]. This is visualized in figure 4.1 (e). In this experiment only one of over two hundred oscillations takes place in the positive part of the $v_1 - v_2$ plane.

4.2 Double scroll trajectories

When we further decrease the resistor value, the double scroll is observed. In figure 4.2 several periodic solutions are shown. The so-called hole filling trajectory is also experimentally observed for $R \approx 1772$ [Ω].
Another special trajectory occurs at $R \approx 1542$ [Ω]. To make that more clear the measured data for this experiment is used in the described Kalman filter to obtain parameter values. With the identified parameters the 1D Poincaré map can be calculated.
This is done by using four different time series in the Kalman filter. For the second iteration the final parameter estimates of the first time series are used as initial conditions. After the fourth iteration the parameter estimates, see table 4.1, are used to compute the 1D Poincaré map. It follows from this map that the trajectory is related to the homoclinic orbit. This homoclinic orbit is another confirmation that the experimental setup is a chaotic system.
It can also be seen in figure 4.4 that this happens just before the double scroll collides with the unstable closed orbit. If the resistor value is decreased further, the trajectory is not bounded by the attractor anymore and v_1 exceeds the saturation level of the operational amplifiers. The

negative resistance becomes positive (passive) and the resulting trajectory is a large stable limit cycle, see chapter 2.

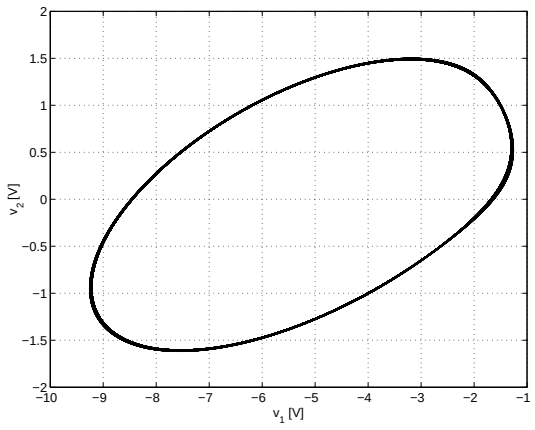

(a) $R \approx 1880$ [Ω].

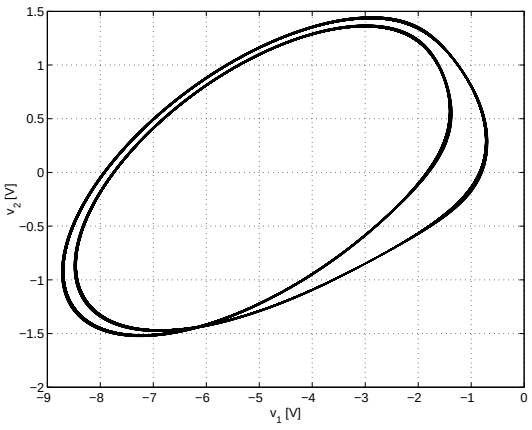

(b) $R \approx 1856$ [Ω].

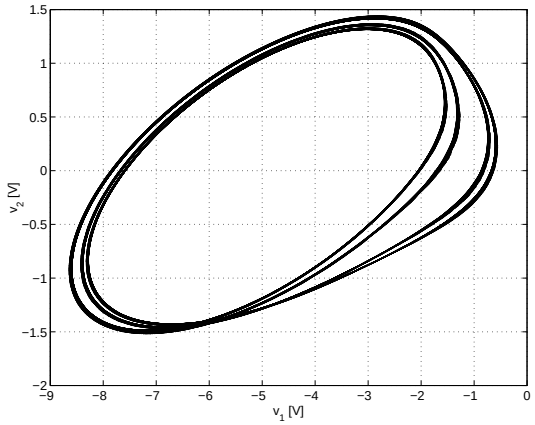

(c) $R \approx 1852$ [Ω].

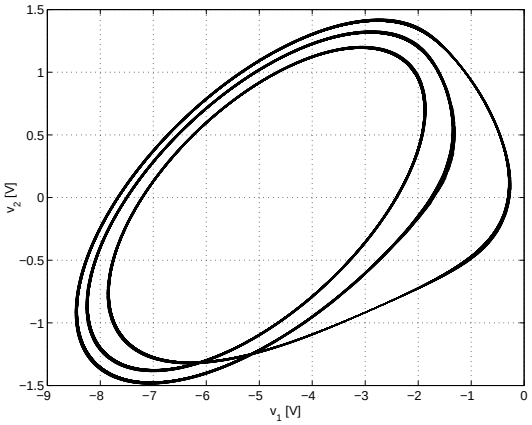

(d) $R \approx 1843$ [Ω].

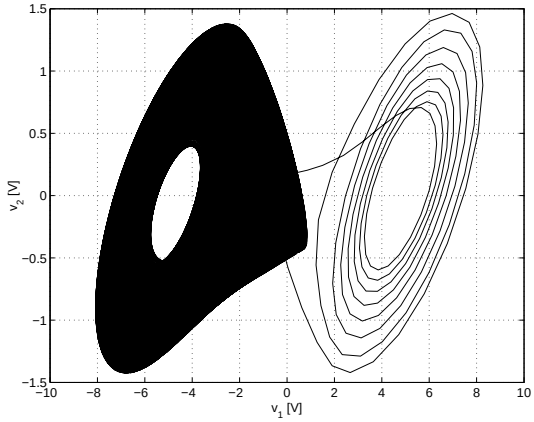

(e) 'Birth' of the double scroll for $R \approx 1823$ [Ω].

Figure 4.1: Projections of v_2 versus v_1 for different values of R.

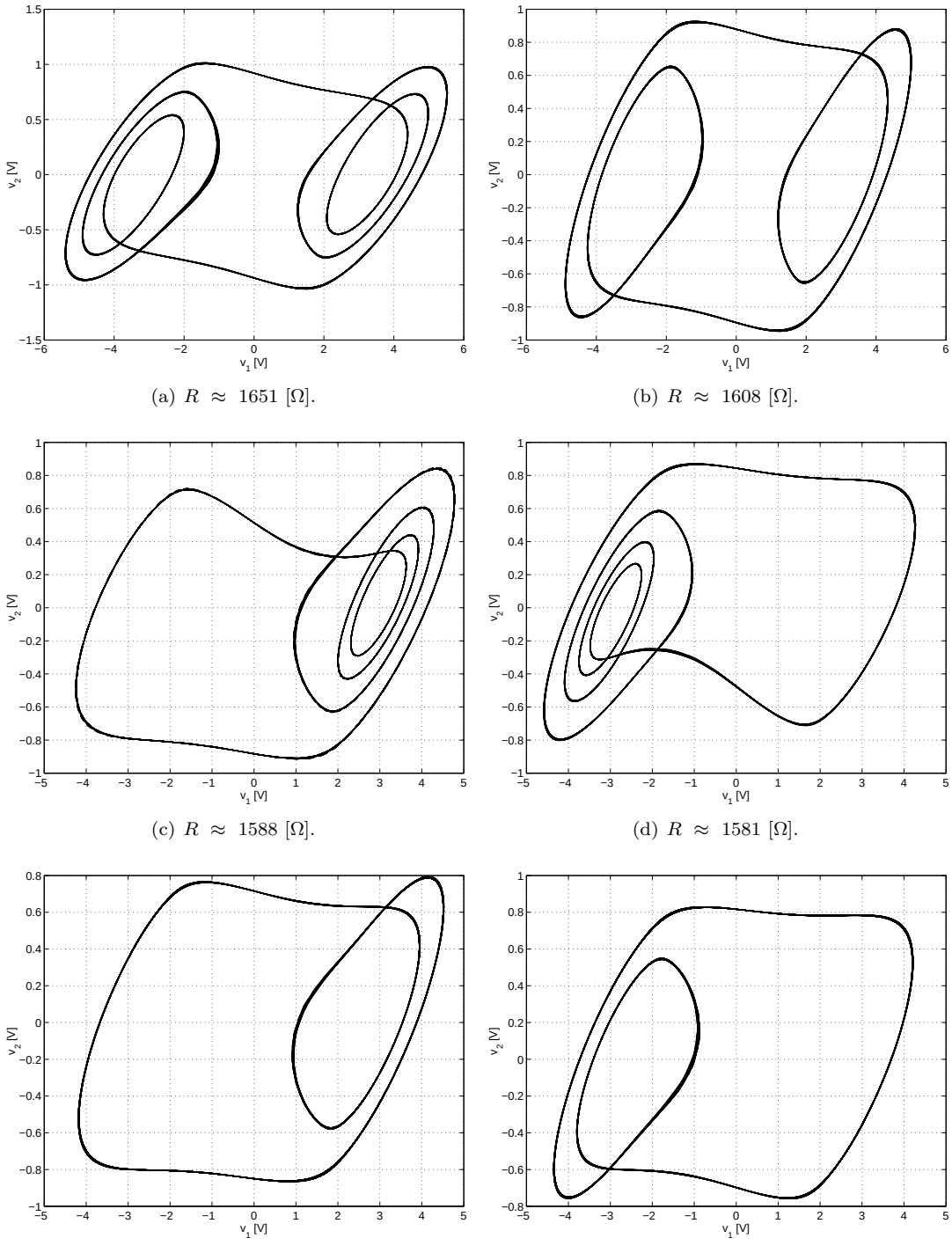

(a) $R \approx 1651$ [Ω].

(b) $R \approx 1608$ [Ω].

(c) $R \approx 1588$ [Ω].

(d) $R \approx 1581$ [Ω].

(e) $R \approx 1564$ [Ω].

(f) $R \approx 1558$ [Ω].

Figure 4.2: Projections of v_2 versus v_1 for different values of R.

Table 4.1: Parameters used to compute the 1D Poincaré map.

Parameter	Value	Parameter	Value
C_1	10.90 [nF]	C_2	97.93 [nF]
G_a	-0.7333 [mS]	G_b^+	-0.4005 [mS]
R	1593 [Ω]	R_0	25.64 [Ω]
L	24.39 [mH]	B_p^+	1.8191 [V]

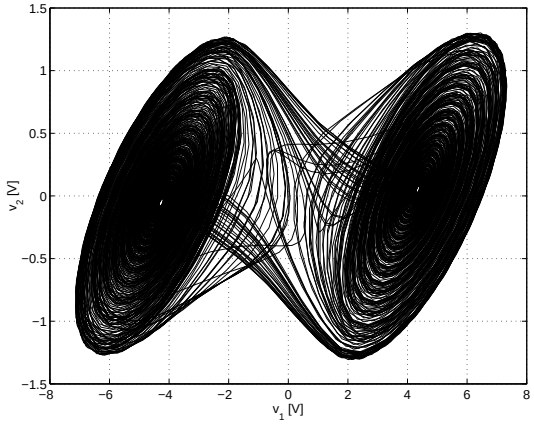

Figure 4.3: Hole filling orbit for $R \approx 1772$ [Ω].

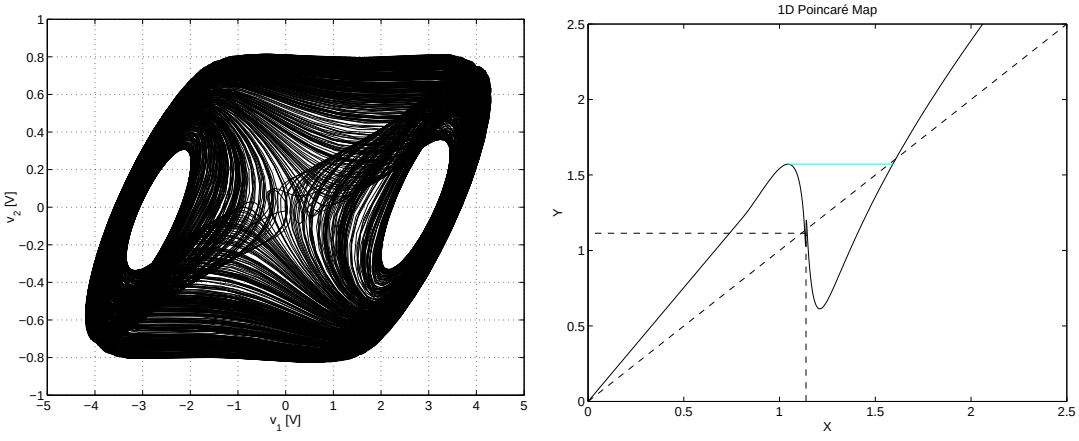

(a) Homoclinic orbit for $R \approx 1542$ [Ω].

(b) Associated 1D Poincaré map.

Figure 4.4: Homoclinic orbit and estimation of the Poincaré map.

Chapter 5

Synchronization

As last part of this thesis synchronization of multiple Chua circuits is investigated.
With synchronization we mean that two or more circuits follow the same trajectory. This might seem strange for chaotic systems, since trajectories of two identical systems with nearly identical initial conditions diverge exponentially. However it is possible for chaotic systems to synchronize with each other under certain conditions.
In this chapter two different methods are used, master-slave synchronization and mutual synchronization. In the case of mutual synchronization an article, which has been written during this graduation project, is included. This article is accompanied with additional numerical simulations.

5.1 Master-slave synchronization

Synchronization of chaotic systems can be found in (Pecora and Carroll, 1990; Carroll and Pecora, 1991). The general scheme for synchronization here is to take a driving system, create a subsystem and drive this and a duplicate of this subsystem, called a response system, with signals from the drive system. A related method is master-slave synchronization. This method consists of a master and a slave system, which follows the master. This can be obtained if we take two identical systems

$$\begin{aligned} \dot{\mathbf{x}}_1 &= \mathbf{F}(\mathbf{x}_1) \\ \dot{\mathbf{x}}_2 &= \mathbf{F}(\mathbf{x}_2) \end{aligned} \tag{5.1}$$

and apply an unidirectional coupling to the second system

$$\begin{aligned} \dot{\mathbf{x}}_1 &= \mathbf{F}(\mathbf{x}_1) \\ \dot{\mathbf{x}}_2 &= \mathbf{F}(\mathbf{x}_2) + f(\mathbf{x}_1, \mathbf{x}_2). \end{aligned} \tag{5.2}$$

Asymptotic synchronization occurs when $\lim_{t\to\infty} |\mathbf{x}_1(t) - \mathbf{x}_2(t)| = 0$. This can be achieved by using continuous feedback (Ott *et al.*, 1990; Pyragas, 1992). A schematic overview can be seen in figure 5.1. Consider (5.2) where some of the state variables can be measured. The chaotic systems are unidirectionally coupled in such a way that the difference between the signals $\mathbf{x}_{1i}$ and $\mathbf{x}_{2i}$ is used as a linear control signal, i.e.

$$f(\mathbf{x}_1, \mathbf{x}_2) = K(\mathbf{x}_{1i} - \mathbf{x}_{2i}), \tag{5.3}$$

which is applied to the second system as a negative feedback. The parameter $K > 0$ is an adjustable gain. An important feature of (5.3) is that it does not change the solution of (5.1).

5.1.1 Numerical results

We use the same parameters as in table 2.1 and choose R equal to 1775 [Ω] such that the circuit operates at the double scroll attractor. The following master-slave configuration, as described in

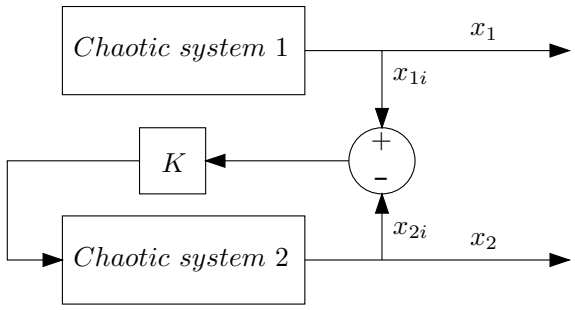

Figure 5.1: Schematic overview of master-slave synchronization using feedback.

(Kapitaniak, 2000), is used:

$$\begin{aligned} C_1\dot{v}_{11} &= G(v_{12}-v_{11})-f(v_{11}) \\ C_2\dot{v}_{12} &= G(v_{11}-v_{12})+i_{L1} \\ L\dot{i}_{L1} &= -v_{12}-R_0 i_{L1} \\ C_1\dot{v}_{21} &= G(v_{22}-v_{21})-f(v_{21})+K_1(v_{11}-v_{21}) \\ C_2\dot{v}_{22} &= G(v_{21}-v_{22})+i_{L2}+K_2(v_{12}-v_{22}) \\ L\dot{i}_{L2} &= -v_{22}-R_0 i_{L2} \end{aligned} \tag{5.4}$$

with $K_i = \frac{1}{R_{ci}}$ the coupling strength and R_{ci} are variable resistors, see figure 5.2.
The asymptotic synchronized situation is defined as

$$\lim_{t\to\infty} |\mathbf{x}_1(t) - \mathbf{x}_2(t)| = 0, \tag{5.5}$$

with $\mathbf{x}_i = [v_{1i}\ v_{2i}\ i_{Li}]$.

First synchronization between identical systems is considered. We consider coupling through K_1 or K_2 respectively. It can be seen in figure 5.3 that synchronization occurs if R_{c1} does not exceed 4100 [Ω]. The upper bound for synchronization using K_2 is approximately $R_{c2} = 2500$ [Ω]. If K_i is increased the circuits synchronize in a shorter time period.

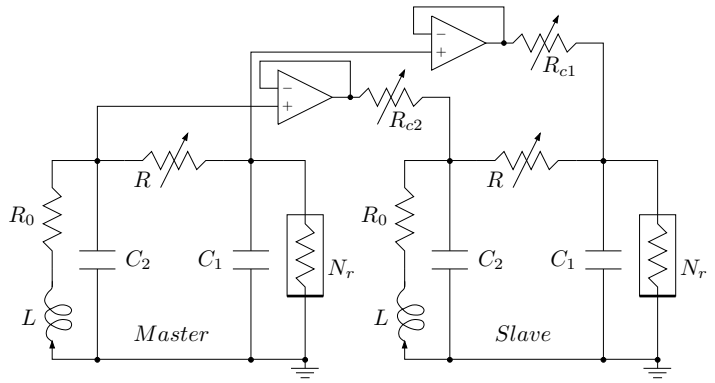

Figure 5.2: Master-slave synchronization for Chua circuits with unidirectional coupling.

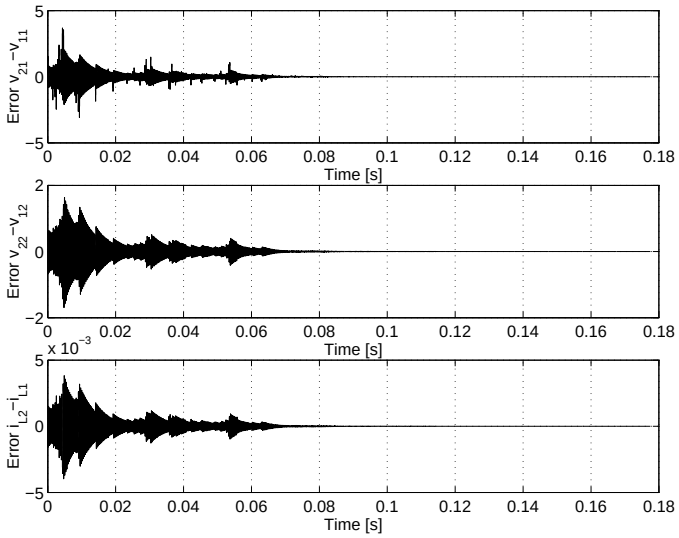

Figure 5.3: $R_{c1} = 4100\ \Omega$. Synchronization error for identical systems.

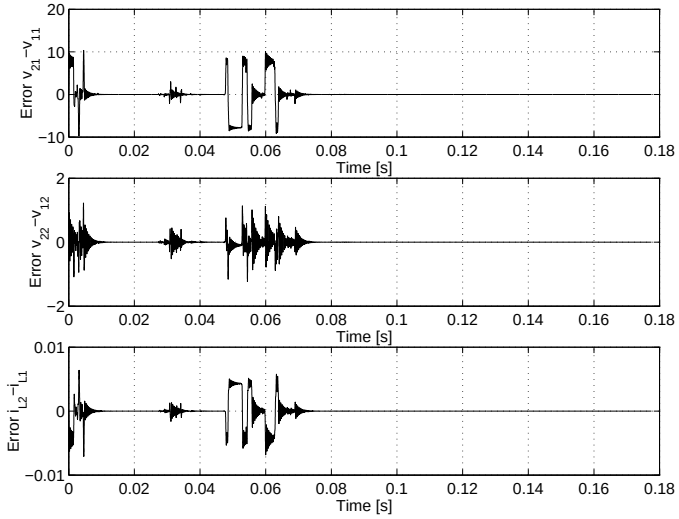

Figure 5.4: $R_{c2} = 2500\ \Omega$. Synchronization error for identical systems.

5.1.2 Non-identical systems

In practice the circuits are build using standard components and due to tolerances of these components every circuit is slightly different. Therefore perfect synchronization is not possible and we introduce a form of practical asymptotic synchronization as

$$\lim_{t\to\infty} |\mathbf{x}_1(t) - \mathbf{x}_2(t)| \leq \delta, \tag{5.6}$$

for some fixed, preferably small, $\delta > 0$.
To simulate the effect of component tolerances some of the parameters are changed, see table 5.1. The results are shown in the figures 5.5 and 5.6.

Table 5.1: Changed parameters for system 1 and 2.

System 1	Value	System 2	Value
C_1	10.90 [nF]	C_1	10.80 [nF]
C_2	97.93 [nF]	C_2	99.60 [nF]
R	1775 [Ω]	R	1778 [Ω]

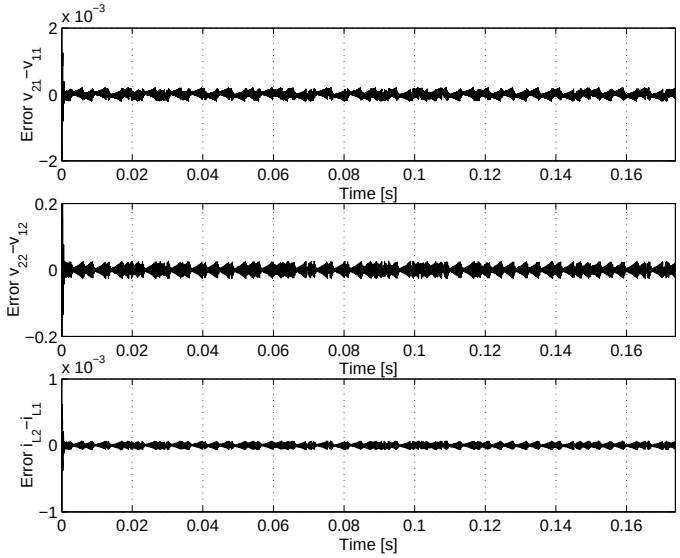

Figure 5.5: $R_{c1} = 10\ \Omega$. Synchronization error for different systems.

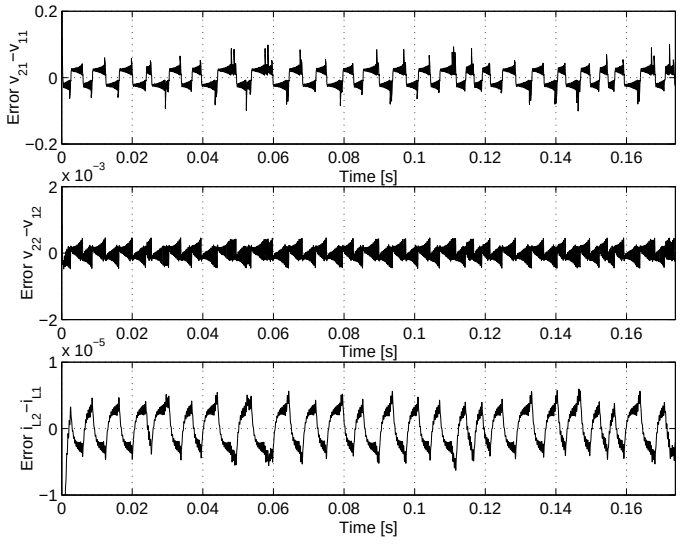

Figure 5.6: $R_{c2} = 10\ \Omega$. Synchronization error for different systems.

5.1.3 Experimental results

For the experiments the value of the variable resistor is fixed for both systems at 1775 [Ω]. In the first experiment both circuits operate as free systems. Although the projections seems similar, see figure 5.7, there is no synchronization. This is shown in figure 5.8. If there is synchronization, it can be seen as a diagonal line in the phase portrait.
In the second experiment the upper bound for R_{c1} is determined, while for the third experiment R_{c1} is chosen as low as possible to create the strongest coupling factor. The same procedure is followed for R_{c2}.
It can be seen that synchronization occurs for a larger range of R_{c1} than R_{c2} and the synchronization error is also smaller. Despite the different values for the resistors again the results are qualitative comparable with the obtained simulation results.
Another interesting phenomenon can be seen in figure 5.12. It seems that there occurs intermittency. Although most of the time the slave is synchronized, it bursts out of synchronization for very short time intervals. This occurs also in numerical simulations if the coupling factor R_{c2} exceeds 2500 [Ω]. Finally we remark that if the coupling strength is decreased the systems start to desynchronize and above a certain threshold value the slave is no longer bounded by the attractor.

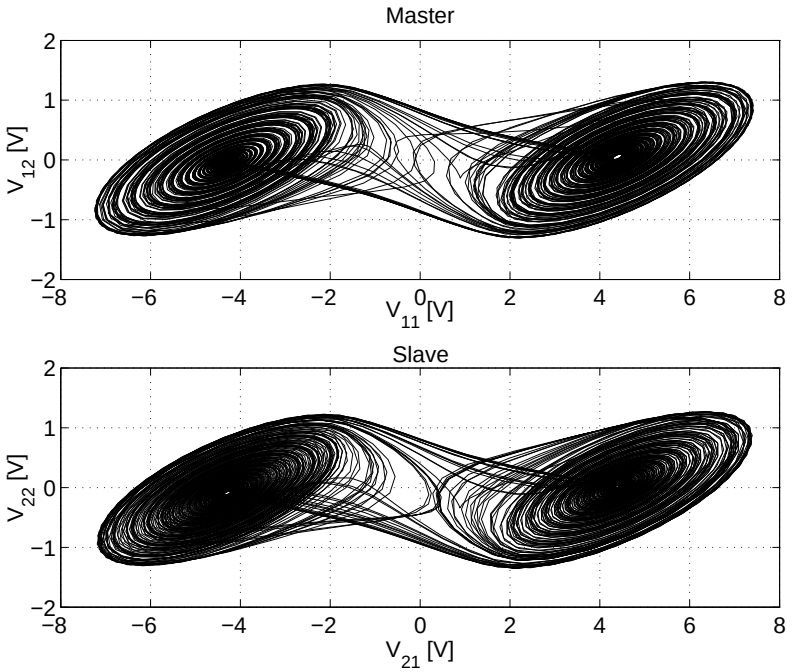

Figure 5.7: Projections of both systems without coupling.

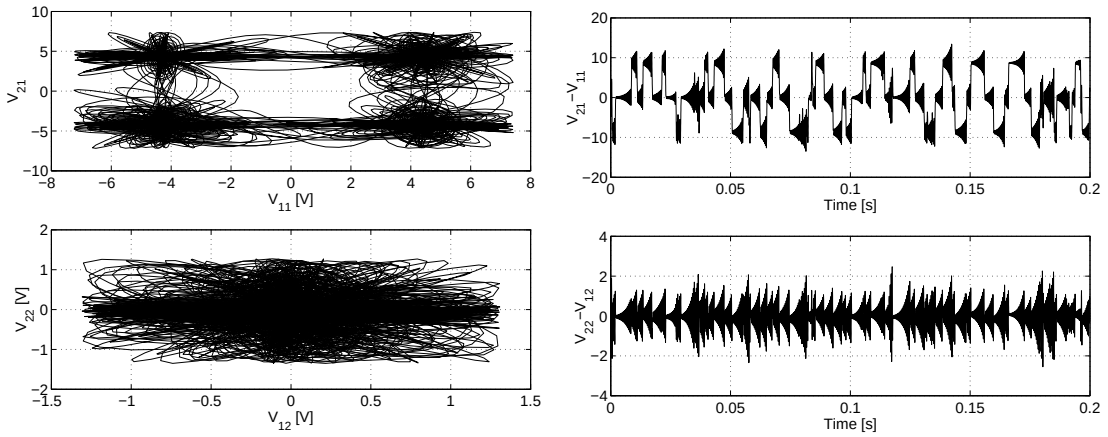

(a) Synchronization phase portraits. (b) Synchronization error.

Figure 5.8: Synchronization phase portrait and error without coupling.

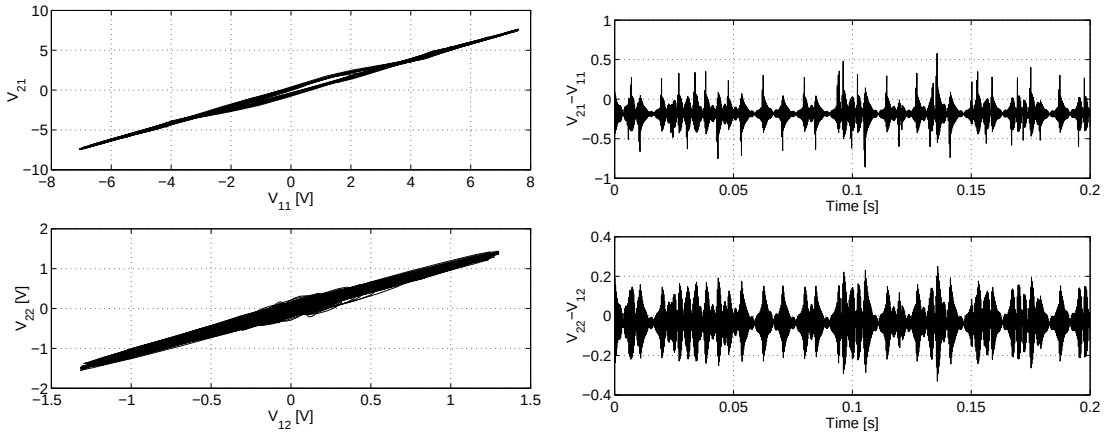

(a) Synchronization phase portraits. (b) Synchronization error.

Figure 5.9: Synchronization phase portrait and error for $R_{c1} \approx$ 3288 [Ω].

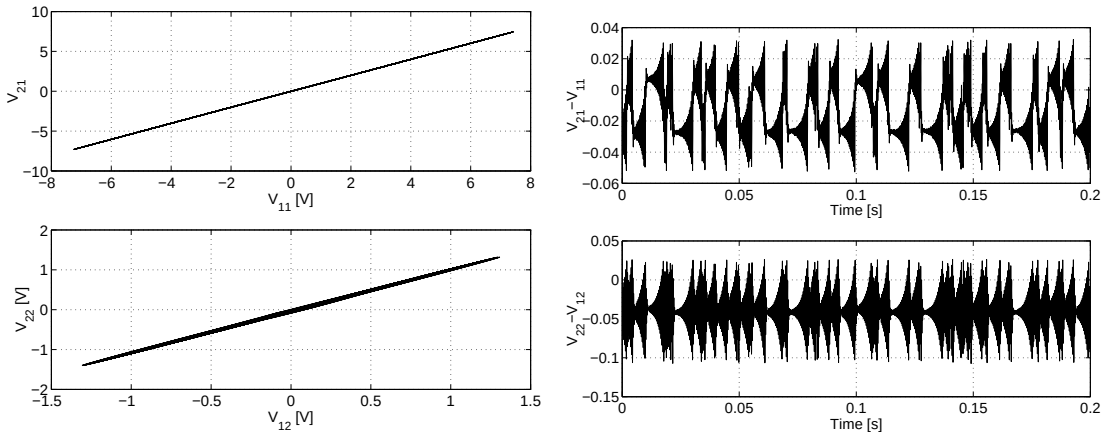

(a) Synchronization phase portraits. (b) Synchronization error.

Figure 5.10: Synchronization phase portrait and error for $R_{c1} \approx 2$ [Ω].

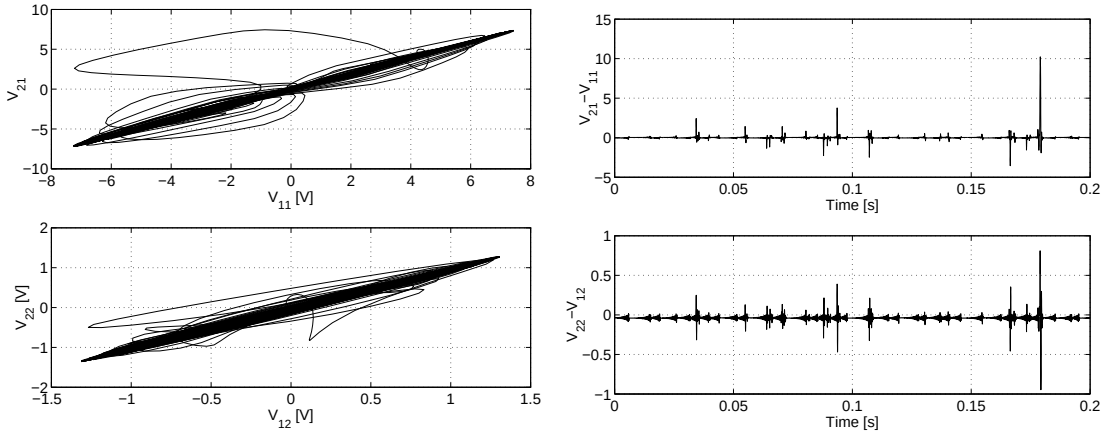

(a) Synchronization phase portraits. (b) Synchronization error.

Figure 5.11: Synchronization phase portrait and error for $R_{c2} \approx 200$ [Ω].

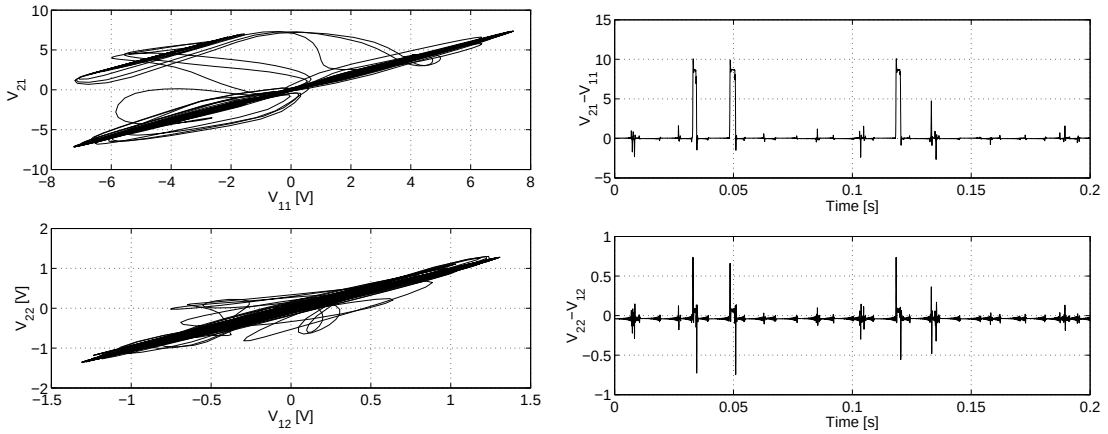

(a) Synchronization phase portraits.

(b) Synchronization error.

Figure 5.12: Synchronization phase portrait and error for $R_{c2} \approx 2$ [Ω].

5.2 Mutual synchronization

In this section a different synchronization scheme is applied, instead of a unidirectional coupling (5.2) we use a bidirectional coupling

$$\begin{aligned} \dot{\mathbf{x}}_1 &= \mathbf{F}(\mathbf{x}_1) + f(\mathbf{x}_1, \mathbf{x}_2) \\ \dot{\mathbf{x}}_2 &= \mathbf{F}(\mathbf{x}_2) + f(\mathbf{x}_1, \mathbf{x}_2). \end{aligned} \tag{5.7}$$

A schematic overview can be seen in figure 5.13. Besides synchronization of two circuits we also investigate synchronization of multiple circuits. When a network of systems is considered it is possible to achieve so-called partial synchronization in the network. Under partial synchronization some systems in the network synchronize, while other do not. Recently partial synchronization in networks of identical systems is receiving particular interest in literature (Hasler *et al.*, 1998; Zhang *et al.*, 2001; Pogromsky *et al.*, 2002). In the following article we present obtained experimental synchronization results for different topologies, with a maximum of four Chua circuits.

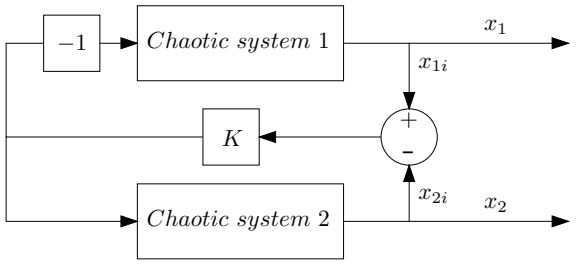

Figure 5.13: Schematic overview of mutual synchronization using diffusive coupling.

PARTIAL SYNCHRONIZATION OF DIFFUSIVELY COUPLED CHUA SYSTEMS: AN EXPERIMENTAL CASE STUDY

R. v.d. Steen, * H. Nijmeijer *

* *Department of Mechanical Engineering, Eindhoven University of Technology, P.O. box 513, 5600 MB, Eindhoven, The Netherlands. R.v.d.Steen@student.tue.nl, H.Nijmeijer@tue.nl*

Abstract: In this paper partial synchronization of diffusively coupled Chua systems is presented. Partial synchronization is defined as the situation where some circuits synchronize with each other, while others do not. An experimental setup, consisting of maximal four Chua circuits operating in the double scroll regime, is used to show the existence of linear invariant manifolds corresponding to the partial synchronized state.

Keywords: Synchronization, Electrical networks, Chaotic behavior, Network topology, Circuits

1. INTRODUCTION

Synchronization of coupled dynamical systems receives much attention in literature. One of the reasons for this is that synchronization can be found in several fields such as nature (Strogatz and Stewart, 1993), brain dynamics (Gray, 1994) and robotics (Nijmeijer and Rodrigues-Angeles, 2003). Also, the potential use of synchronization in communication and coordination forms a major reason for this interest. Recently partial synchronization in networks of identical systems is receiving particular interest. Some examples of partial synchronization can be found in (Hasler *et al.*, 1998; Zhang *et al.*, 2001; Pogromsky *et al.*, 2002).

Although there are many papers describing global synchronization of a network of coupled Chua circuits (Wu and Chua, 1995; Matías *et al.*, 1997; Sánchez *et al.*, 2000), less attention sofar has been devoted to experimental results for bidirectional coupled systems. In this paper attention will be drawn to partial synchronization of Chua circuits. Partial synchronization is defined as the situation where some circuits synchronize with each other, while others do not. It is shown that under certain conditions it is possible to obtain partial synchronization of diffusively coupled Chua circuits. An experimental setup consisting of four coupled Chua circuits is build to show the possibility of partial synchronization. The experimental results obtained qualitatively confirm simulation results. The remainder of this paper is organized as follows. In section 2 some preliminaries about the used notation are given. Further passive and convergent systems are described and the conditions for partial synchronization are stated. Section 3 deals with the experimental setup that is used. In section 4 and 5 synchronization of two and three diffusively coupled systems is shown, while in section 6 global and partial synchronization of four diffusively coupled systems is presented and discussed. Finally conclusions are drawn in section 7.

2. PRELEMINARIES

First a mathematical description for a network of coupled systems is introduced by adopting the notation used in (Pogromsky *et al.*, 2002). A general system description for k identical systems is given by

$$\dot{\mathbf{x}}_i = \mathbf{f}(\mathbf{x}_i) + \mathbf{B}\mathbf{u}_i, \quad \mathbf{y}_i = \mathbf{C}\mathbf{x}_i \tag{1}$$

where $\mathbf{f}$ is a vector field, $i = 1, \ldots, k$, $\mathbf{x}_i(t) \in \mathbb{R}^n$ is the state of the ith system, $\mathbf{u}_i(t) \in \mathbb{R}^m$ and $\mathbf{y}_i(t) \in \mathbb{R}^m$ are the input and output of the ith system, while $\mathbf{B}$, $\mathbf{C}$ are matrices of appropriate dimension.
The k systems are coupled through linear outputs

$$\mathbf{u}_i = -\gamma_{i1}(\mathbf{y}_i - \mathbf{y}_1) - \gamma_{i2}(\mathbf{y}_i - \mathbf{y}_2) - \cdots - \gamma_{ik}(\mathbf{y}_i - \mathbf{y}_k). \tag{2}$$

By defining the symmetric $k \times k$ matrix $\mathbf{\Gamma}$ as

$$\mathbf{\Gamma} = \begin{pmatrix} \sum_{i=2}^{k} \gamma_{1i} & -\gamma_{12} & \cdots & -\gamma_{1k} \\ -\gamma_{21} & \sum_{i=1, i\neq 2}^{k} \gamma_{2i} & \cdots & -\gamma_{2k} \\ \vdots & \vdots & \ddots & \vdots \\ -\gamma_{k1} & -\gamma_{2k} & \cdots & \sum_{i=1}^{k-1} \gamma_{1i} \end{pmatrix}, \tag{3}$$

the collection of k systems, with the matrix $\mathbf{\Gamma}$ and feedback $\mathbf{u}_i$, can be rewritten as

$$\dot{\mathbf{x}} = \mathbf{F}(\mathbf{x}) + (\mathbf{I}_k \otimes \mathbf{B})\mathbf{u}, \quad \mathbf{y} = (\mathbf{I}_k \otimes \mathbf{C})\mathbf{x} \tag{4}$$

with the feedback

$$\mathbf{u} = -(\mathbf{\Gamma} \otimes \mathbf{I}_m)\mathbf{y} \tag{5}$$

where $\mathbf{x} = col(\mathbf{x}_1, \ldots, \mathbf{x}_k)$, $\mathbf{F}(\mathbf{x}) = col(\mathbf{f}(\mathbf{x}_1), \ldots, \mathbf{f}(\mathbf{x}_k)) \in \mathbb{R}^{kn}$, $\mathbf{y} = col(\mathbf{y}_1, \ldots, \mathbf{y}_k)$ and $\mathbf{u} = col(\mathbf{u}_1, \ldots, \mathbf{u}_k) \in \mathbb{R}^{km}$. The notation $col(\mathbf{x}_1, \ldots, \mathbf{x}_k)$ stands for the column vector composed of the vectors $\mathbf{x}_1, \ldots, \mathbf{x}_k$. The notation $\otimes$ stands for the Kronecker product.

A system

$$\dot{\mathbf{x}} = \mathbf{f}(\mathbf{x}, \mathbf{u}), \quad \mathbf{y} = \mathbf{h}(\mathbf{x}) \tag{6}$$

is called passive, see (Willems, 1972), if the following inequality holds

$$\frac{d}{dt}V(\mathbf{x}) = \frac{\partial V(\mathbf{x})}{\partial \mathbf{x}}\mathbf{f}(\mathbf{x}, \mathbf{u}) \leq \mathbf{y}^T\mathbf{u} \tag{7}$$

where $V(\mathbf{x})$ is a nonnegative function (storage function) defined on $\mathbb{R}^n$, for which $V(0) = 0$. If the dissipation inequality (7) is satisfied only for $\mathbf{x}$ lying outside some ball

$$\dot{V}(\mathbf{x}, \mathbf{u}) \leq \mathbf{y}^T\mathbf{u} - H(\mathbf{x}) \tag{8}$$

where the function $H : \mathbb{R}^n \to \mathbb{R}$ is nonnegative outside some ball

$$\exists \rho > 0, \quad |\mathbf{x}| \geq \rho \Rightarrow H(\mathbf{x}) \geq 0, \tag{9}$$

then the system is semipassive, see (Pogromsky *et al.*, 2002).

Consider a system

$$\dot{\mathbf{z}} = \mathbf{q}(\mathbf{z}, w(t)), \tag{10}$$

with $\mathbf{z} \in \mathbb{R}^l$, driven by an external signal $w(t)$ taking values from a compact set. The system (10) is called convergent if for any bounded input $w(t)$ the solution of (10) converges to a solution $\mathbf{z}_w(t)$, in other words, the solution of (10) will forget their specific initial condition. If there exists a positive definite symmetric $l \times l$ matrix $\mathbf{P}$ such that all eigenvalues $\lambda_i(\mathbf{Q})$ of the symmetric matrix

$$\mathbf{Q}(\mathbf{z}, w) = \frac{1}{2}\left[\mathbf{P}\left(\frac{\partial \mathbf{q}}{\partial \mathbf{z}}(\mathbf{z}, w)\right) + \left(\frac{\partial \mathbf{q}}{\partial \mathbf{z}}(\mathbf{z}, w)\right)^T \mathbf{P}\right] \tag{11}$$

are negative and separated from zero, such that

$$\lambda_i(\mathbf{Q}(\mathbf{z}, w)) \leq \epsilon < 0, \tag{12}$$

with $\epsilon > 0$ and $i = 1 \ldots l$ for all $\mathbf{z}, w \in \mathbb{R}^l$, then system (10) is convergent, cf (Pavlov *et al.*, 2004).

If the network contains repeating patterns, the permutation of some elements of $\mathbf{\Gamma}$ leave the network invariant. Such a permutation matrix $\mathbf{\Pi}$ is a symmetry for the network if $\mathbf{\Pi}$ commutes with $\mathbf{\Gamma}$, i.e. $\mathbf{\Pi}\mathbf{\Gamma} - \mathbf{\Gamma}\mathbf{\Pi} = 0$. A permutation matrix $\mathbf{\Pi}$ commuting with $\mathbf{\Gamma}$ defines a linear invariant manifold of the closed loop system (4) and (5) as

$$\ker(\mathbf{I}_{kn} - \mathbf{\Pi} \otimes \mathbf{I}_n). \tag{13}$$

The stability of such manifolds depends on the asymptotic stability of sets. Due to converse Lyapunov theorem, e.g. (Lin *et al.*, 1996), the asymptotic stability of a set is equivalent to the existence of a scalar storage function V, which is zero only on the set and decays along the trajectories otherwise. In the context of the coupled systems (1, 2) a Lyapunov function should be found as a sum of two functions. The first function depends on the input-output relations of the systems (1), while the second function depends on the interacting due to the coupling of systems.
Under the assumption that the matrix $\mathbf{CB}$ is nonsingular (and positive definite) a linear coordinate transformation $\mathbf{x}_i \to (\mathbf{y}_i,\ \mathbf{z}_i)$ exists such that

$$\dot{\mathbf{z}}_i = \mathbf{q}(\mathbf{z}_i, \mathbf{y}_i), \quad \dot{\mathbf{y}}_i = \mathbf{g}(\mathbf{z}_i, \mathbf{y}_i) + \mathbf{CB}\mathbf{u}_i, \tag{14}$$

where $\mathbf{z}_i \in \mathbb{R}^{n-m}$ and $\mathbf{q}$ and $\mathbf{g}$ are vector functions. Then the stability of the manifolds given by (13) is determined by the following theorem.

Theorem 1 (Pogromsky *et al.*, 2002). Let λ' be the minimal eigenvalue of $\mathbf{\Gamma}$ under restriction that the eigenvectors of $\mathbf{\Gamma}$ are taken from the set range$(\mathbf{I}_k - \mathbf{\Pi})$. Suppose that:

1. Each individual system (1) is strictly semipassive with respect to the input $\mathbf{u}_i$ and output

$\mathbf{y}_i$ with a radially unbounded storage function $V(\mathbf{x_i}, \mathbf{u_i})$.
2. There exists a positive definite matrix $\mathbf{P}$ such that inequality (12) holds for some $\epsilon > 0$ for the matrix $\mathbf{Q}$ defined as in (11) for $\mathbf{q}$ as in (14).
Then all solutions of the diffusive cellular network (4) and (5) are ultimately bounded and there exists a positive $\bar{\lambda}$ such that if $\lambda' > \bar{\lambda}$ the set $\ker(\mathbf{I}_{kn} - \mathbf{\Pi} \otimes \mathbf{I}_n)$ contains a globally asymptotically stable compact subset.

3. SETUP

An experimental setup consisting of a network of 4 Chua circuits is used, shown in figure 1. Consider

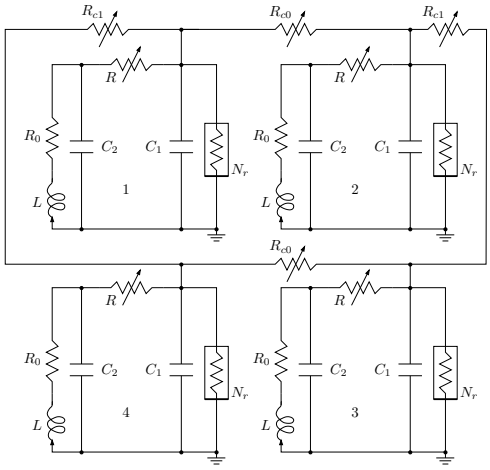

Fig. 1. Schematic layout of four symmetrically coupled Chua circuits.

the well known system description of a single Chua circuit (Matsumoto, 1984)

$$\begin{aligned} C_1\dot{x}_{i1} &= G(x_{i2} - x_{i1}) - f(x_{i1}) \\ C_2\dot{x}_{i2} &= G(x_{i1} - x_{i2}) + x_{i3} \\ L\dot{x}_{i3} &= -x_{i2} - R_0 x_{i3} \end{aligned} \tag{15}$$

with $G = \frac{1}{R}$ and the function $f(x_{i1})$ defined as

$$G_b x_{i1} + \tfrac{1}{2}(G_a - G_b)(|x_{i1} + B_p| - |x_{i1} - B_p|). \tag{16}$$

In these equations the variables x_{i1} and x_{i2} are the voltages across the capacitors, C_1 and C_2, x_{i3} is the current flowing through the inductor L, which has an internal resistance R_0. G_a and G_b are the conductances of the piecewise characteristic for $|x_{i1}| < B_p$ and $|x_{i1}| \geq B_p$ respectively. B_p is voltage of the breakpoint. Measurements of x_{i1} and x_{i2} are available. For the coupling between systems the matrices $\mathbf{B}$ and $\mathbf{C}$ are as follows

$$\mathbf{B} = [1\ 0\ 0]^T \quad \mathbf{C} = [1\ 0\ 0]. \tag{17}$$

The coupling strength between systems is controlled by four variable resistors. The nonlinear resistor, N_r, in the circuits is build with operational amplifiers (AD712JN) as described in (Kennedy, 1992). The nominal values of the components can be found in table 1, however due to tolerances of the components each circuit is slightly different. Therefore synchronization in the sense that $|\mathbf{x}_i(t) - \mathbf{x}_j(t)| = 0$ is not possible and practical synchronization is defined as $|\mathbf{x}_i(t) - \mathbf{x}_j(t)| \leq \delta$, for some fixed $\delta > 0$.

Table 1. Nominal values for each circuit.

Component	Value
C_1	10 [nF]
C_2	100 [nF]
L	22 [mH]
R_0	22 [Ω]
R	1.5-2.0 [kΩ]
G_a	-0.758 [mS]
G_b	-0.409 [mS]
B_p	1.75 [V]

4. TWO SYSTEMS

Before synchronization of four systems is considered, the threshold value for synchronization of two circuits is determined, i.e., the minimal value K such that practical synchronization occurs. The two circuits are diffusely coupled with a variable resistor, R_c, which gives the coupling constant K as $\frac{1}{R_c}$ and a coupling matrix

$$\mathbf{\Gamma}_1 = \begin{bmatrix} K & -K \\ -K & K \end{bmatrix}. \tag{18}$$

The variable resistor R is set to 1775 [Ω] on both circuits, so the circuits operate on the double scroll attractor. Synchronization is visualized by the phase portrait of x_{11} and x_{21}, shown in figure 2(b). The value of R_c for the synchronization threshold is around 3400 [Ω] with $\delta = 0.15$ [V].

Remark: If the value R_c is increased, desynchronization occurs and at about $R_c = 10$ [kΩ] the trajectories are no longer bounded. A possible explanation for this phenomena is the following. A single circuit (15), with $\mathbf{u} = 0$, can have unbounded trajectories. No storage function $V(\mathbf{x})$ can be found such that inequality (8) is satisfied to prove semipassivity for system (15). Therefore it is not guaranteed that the solutions are ultimately bounded. This may cause the bursting phenomenon above 10 [kΩ]. For $R_c = 30$ [kΩ] and above the current through the coupling resistor becomes negligible such that both circuits operate as free systems and the trajectories of both are bounded by their attractors again.

5. THREE SYSTEMS

When the network is expanded by adding a circuit, see figure 3, the following coupling matrix Γ is obtained

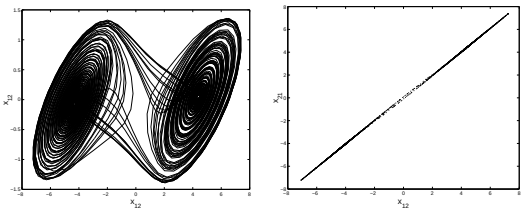

(a) Projection of x_{12} versus x_{11}.

(b) Phase portrait of x_{21} versus x_{11}.

Fig. 2. Experimental synchronization for $R_c = 3430$ [Ω].

$$\mathbf{\Gamma}_2 = \begin{bmatrix} 2K & -K & -K \\ -K & 2K & -K \\ -K & -K & 2K \end{bmatrix}. \tag{19}$$

The coupling constant needed to globally synchronize this structure can be estimated using the conjecture stated in (Wu and Chua, 1996):

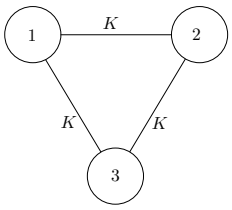

Fig. 3. Layout of three coupled systems.

$$\mu_1\alpha_1 = \mu_2\alpha_2 \tag{20}$$

where $\mu_i,\ i = 1, 2$ is the smallest nonzero eigenvalue of the coupling matrix $\mathbf{\Gamma}_i$ and α_i the coupling coefficient. Although it has been pointed out in (Pecora, 1998) that this conjecture is in general wrong, it holds in this particular case.
The synchronization threshold for three systems, using (20), requires a resistor value of 5100 [Ω]. The threshold value in experiments is found to be 4950 [Ω], confirming that three systems, coupled in a ring structure, synchronize with a lower coupling constant K.

6. FOUR SYSTEMS

Four systems are symmetrically coupled in a ring structure with two coupling constants K_0 and K_1. With the proposed coupling, as shown in figure 4,

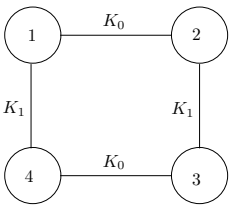

Fig. 4. Layout of four coupled systems.

the coupling matrix $\mathbf{\Gamma}$ can be written as follows

$$\mathbf{\Gamma}_3 = \begin{bmatrix} K_0+K_1 & -K_0 & 0 & -K_1 \\ -K_0 & K_0+K_1 & -K_1 & 0 \\ 0 & -K_1 & K_0+K_1 & -K_0 \\ -K_1 & 0 & -K_0 & K_0+K_1 \end{bmatrix} \tag{21}$$

If $K_0 = K_1 = K$ the smallest nonzero eigenvalue of $\mathbf{\Gamma}_3$, μ_3, is equal to the smallest eigenvalue of $\mathbf{\Gamma}_1$, and the ring structure should synchronize with R_c around 3400 [Ω]. In figure 5 global synchronization is shown for $R_c = 3200$ [Ω] again with $\delta = 0.15$ [V].

With the symmetric coupling matrix (21) there are four permutation matrices $\mathbf{\Pi}$ commuting with $\mathbf{\Gamma}_3$

$$\mathbf{\Pi}_1 = \begin{bmatrix} \mathbf{A} & \mathbf{O} \\ \mathbf{O} & \mathbf{A} \end{bmatrix}, \quad \mathbf{\Pi}_2 = \begin{bmatrix} \mathbf{O} & \mathbf{I}_2 \\ \mathbf{I}_2 & \mathbf{O} \end{bmatrix}$$
$$\mathbf{\Pi}_3 = \begin{bmatrix} \mathbf{O} & \mathbf{A} \\ \mathbf{A} & \mathbf{O} \end{bmatrix}, \quad \mathbf{\Pi}_4 = \mathbf{I}_4 \tag{22}$$

where

$$\mathbf{A} = \begin{bmatrix} 0 & 1 \\ 1 & 0 \end{bmatrix}, \quad \mathbf{O} = \begin{bmatrix} 0 & 0 \\ 0 & 0 \end{bmatrix}. \tag{23}$$

Three linear invariant manifolds associated with (22) exist independently of systems (1) and are given by

$$\mathcal{A}_1 = \mathbf{x} \in \mathbb{R}^{4n} : \mathbf{x}_1 = \mathbf{x}_2, \mathbf{x}_3 = \mathbf{x}_4 \tag{24}$$
$$\mathcal{A}_2 = \mathbf{x} \in \mathbb{R}^{4n} : \mathbf{x}_1 = \mathbf{x}_3, \mathbf{x}_2 = \mathbf{x}_4 \tag{25}$$
$$\mathcal{A}_3 = \mathbf{x} \in \mathbb{R}^{4n} : \mathbf{x}_1 = \mathbf{x}_4, \mathbf{x}_2 = \mathbf{x}_3. \tag{26}$$

The intersection of any two of these manifolds describes the full synchronization manifold ($\mathbf{x}_1 = \mathbf{x}_2 = \mathbf{x}_3 = \mathbf{x}_4$). There are two possible ways to global synchronization depending on the ratio K_0 and K_1

$$\mathcal{A}_1 \to \mathcal{A}_1 \cap \mathcal{A}_2 \tag{27}$$
$$\mathcal{A}_3 \to \mathcal{A}_3 \cap \mathcal{A}_2. \tag{28}$$

Theorem 1, to prove stability of these manifolds, depends on two conditions. It is already pointed out that the first condition is not satisfied, since system (15) is not semipassive. However on an experimental setup the solutions are normally bounded by the attractor.
With x_1 chosen as the external signal in (14) and $\mathbf{z} = [x_2\ x_3]^T$ and the parameter values in table 1, it is possible to find a matrix $\mathbf{P}$ such that (12) is satisfied and therefore system (15) is convergent. Hence it is expected that these manifolds are locally stable on the Chua circuits as long as the solutions remain bounded by the attractor. This is confirmed as shown in figures 6 and 7. In figure 6 it can be seen that the circuits one and two and also three and four are synchronized with a coupling constant $K_0 = \frac{1}{R_{c0}}$. Circuits two

and three, coupled with $K_1 = \frac{1}{R_{c1}}$, are, as well as one and four, not synchronized. This corresponds to manifold $\mathcal{A}_1$ (24). In figure 7 the situation corresponding to manifold $\mathcal{A}_3$ (26) is depicted. These manifolds are robust to parameter variation of the variable resistors R of the circuits. However if the coupling resistances are increased the same phenomena with two coupled systems occurs, i.e., the trajectories are no longer bounded. And again above a second threshold the four circuits operate as free systems. All these phenomena are summarized in a stability diagram shown in figure 8.

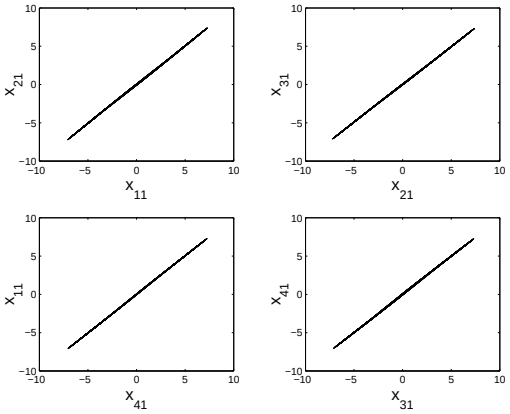

Fig. 5. Phase portraits for global synchronization with $R_{c0} = R_{c1} = 3200$ [Ω].

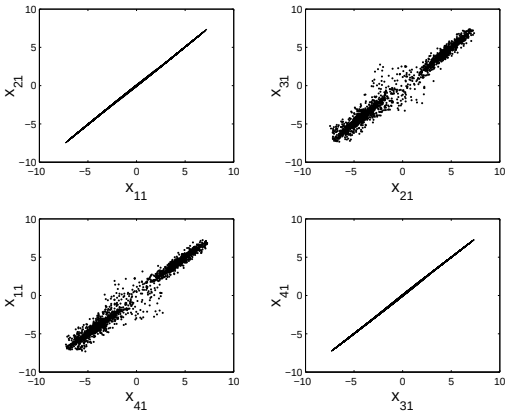

Fig. 6. Phase portraits for partial synchronization with $R_{c0} = 3200$ and $R_{c1} = 9300$.

This stability diagram can also be obtained by numerically integrating four Chua systems (15), taking the tolerances of the components into account. The presented experimental results are qualitative comparable with numerical simulations. As an illustrative numerical example partial synchronization is considered. For the individual systems the capacitors and variable resistor are chosen as in table 2, while the other parameters of system (15) are the same as in table 1. The coupling constants K_0 and K_1 are $\frac{1}{8500}$ and $\frac{1}{3200}$ respectively. In figure 9 the error signals $x_{i1} - x_{j1},\ i, j = 1, 2, 3, 4$ are

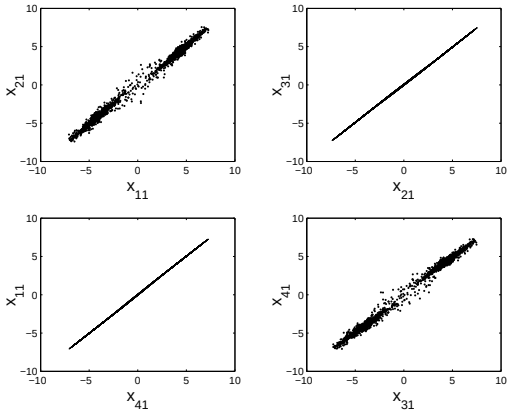

Fig. 7. Phase portraits for partial synchronization with $R_{c0} = 9300$ and $R_{c1} = 3200$.

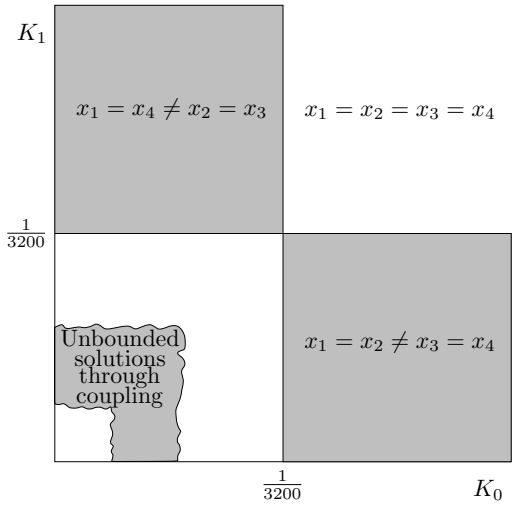

Fig. 8. Stability diagram.

shown. After the transients are vanished systems two and three synchronize as well as one and four. This simulation result matches with the experimental partial synchronization as shown in figure 7.

Table 2. Parameter values for individual circuits.

System	Component	Value
1	C_1	10.90 [nF]
	C_2	97.93 [nF]
	R	1775 [Ω]
2	C_1	10.80 [nF]
	C_2	99.60 [nF]
	R	1778 [Ω]
3	C_1	10.98 [nF]
	C_2	101.90 [nF]
	R	1770 [Ω]
4	C_1	10.65 [nF]
	C_2	100.50 [nF]
	R	1780 [Ω]

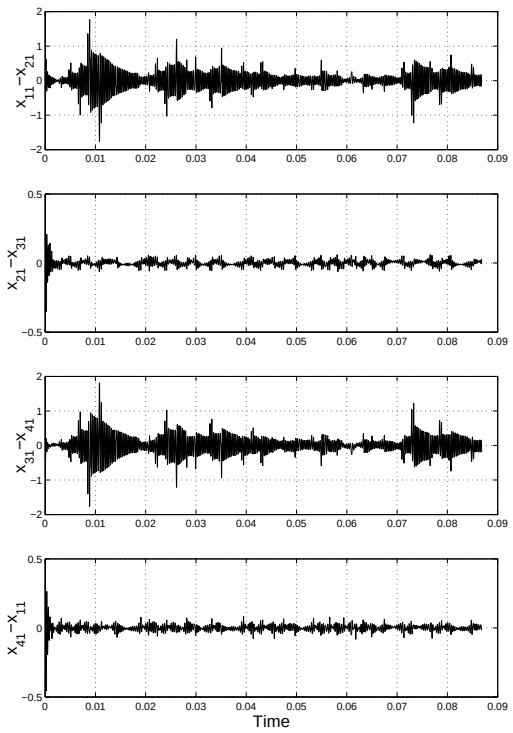

Fig. 9. Simulation synchronization errors for $R_{c0} = 8500$ and $R_{c1} = 3200$.

7. CONCLUSIONS

In this paper experimental partial synchronization of diffusively coupled Chua circuits is presented. With the experimental setup it is impossible to achieve a zero synchronization error due to tolerances of the electrical components. Therefore a form of practical synchronization is introduced to be able to specify synchronization of two systems. Besides global synchronization of two circuits, a bursting phenomena is observed if the diffusive coupling between two systems is above a certain threshold value. At this point the trajectories are no longer bounded by the double scroll attractor. In the case where four circuits are symmetrically coupled it shown that partial synchronization is possible. The stability of the linear invariant manifolds, describing this partial synchronization, can not be proven globally. However the manifolds are locally stable if the solutions remain bounded by the double scroll attractors.

REFERENCES

Gray, C.M. (1994). Synchronous oscillations in neuronal systems: mechanisms and functions. *J. Comput. Neurosci.* **1**, 11–38.

Hasler, M., Y. Maistrenko and O. Popovych (1998). Simple example of partial synchronization of chaotic systems. *Phys. Rev. E* **58**(5), 6843–6846.

Kennedy, M.P. (1992). Robust Op Amp realization of Chua's circuit. *Frequenz* **46**(3-4), 66–80.

Lin, Y., E.D. Sontag and Y. Wang (1996). A smooth converse lyapunov theorem for robust stability. *SIAM J. Control Opt.* **34**, 124–160.

Matías, M.A., V. Pérez-Muñuzuri, M.N. Lorenzo, I.P. Mariño and V.Pérez-Villar (1997). Observation of a fast rotating wave in rings of coupled chaotic oscillators. *Phys. Rev. Lett.* **78**(2), 219–222.

Matsumoto, T. (1984). A chaotic attractor from Chua's circuit. *IEEE Trans. Circ. Syst.* **31**(12), 1055–1058.

Nijmeijer, H. and A. Rodrigues-Angeles (2003). *Synchronization of mechanical systems.* World Scientific Publishing Co. London.

Pavlov, A., A. Pogromsky, N. van de Wouw and H. Nijmeijer (2004). Convergent dynamics, a tribute to Boris Pavlovich Demidovich. *Sys. Cont. Lett.* **52**, 257–261.

Pecora, L.M. (1998). Synchronization conditions and desynchronization patterns in coupled limit-cycle and chaotic systems. *Phys. Rev. E* **58**(1), 347–360.

Pogromsky, A., G. Santoboni and H. Nijmeijer (2002). Partial synchronization: from symmetry towards stability. *Physica D* **172**, 65–87.

Sánchez, E., M.A. Matías and V. Pérez-Muñuzuri (2000). Chaotic synchronization in small assemblies of driven Chua's circuits. *IEEE Trans. Circ. Syst.* **47**(5), 644–654.

Strogatz, S.H. and I. Stewart (1993). Coupled oscillators and biological synchronization. *Sci. Am.* **269**, 102–109.

Willems, J.C. (1972). Dissipative Dynamical Systems Part I: General Theory. *Arch. Rational. Mech. Anal.* **45**, 321–351.

Wu, C.W. and L.O. Chua (1995). Synchronization in an array of linearly coupled dynamical systems. *IEEE Trans. Circ. Syst.* **42**(8), 430–447.

Wu, C.W. and L.O. Chua (1996). On a conjecture regarding the synchronization in an array of linearly coupled dynamical systems. *IEEE Trans. Circ. Syst.* **43**(2), 161–165.

Zhang, Y., G. Hu, H.A. Cerdeira, S. Chen, T. Braun and Y. Yao (2001). Partial synchronization and spontaneous spatial ordering in coupled chaotic systems. *Phys. Rev. E* **63**, 026211.

5.2.2 Additional simulations

As an addition to this article some numerical results are included to complement the presented experimental results. These simulations are carried out for the situation of the four diffusively coupled systems.
The stability diagram, see fig. 8 in the article, is used as a guideline for the simulations. We consider the second partial synchronized and the full synchronized situation. Further the different situations for the unsynchronized state are given.
In figure 5.14 the second partial synchronization is shown. This corresponds to the situation that $\mathbf{x}_1 = \mathbf{x}_2 \neq \mathbf{x}_3 = \mathbf{x}_4$. Full synchronization can be seen in figure 5.15.
In the case of weak coupling three situations exist. If the coupling resistances are increased the circuits first desynchronize, then the trajectories grow unbounded and finally the resistance is so high that the current is negligible and the circuits operate as it are free systems.

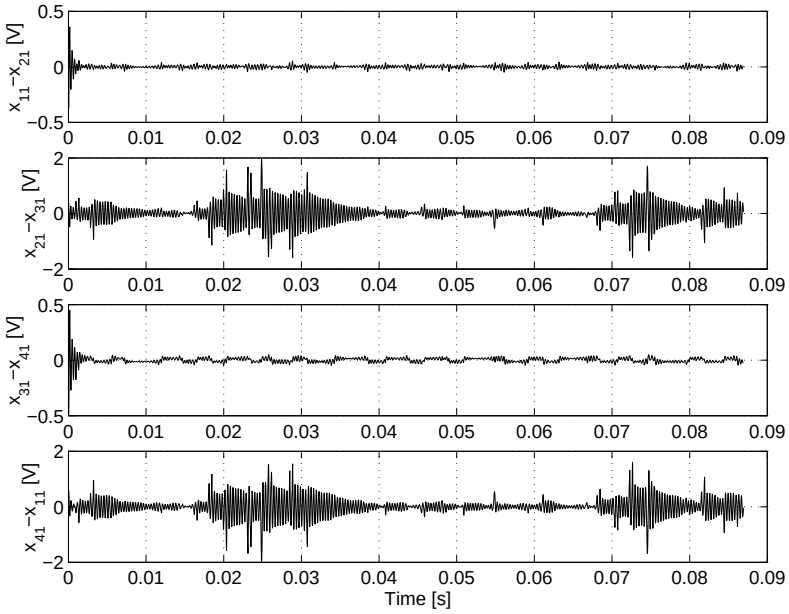

Figure 5.14: Synchronization error for $R_{c0} = 3200$ [Ω] and $R_{c1} = 8500$ [Ω].

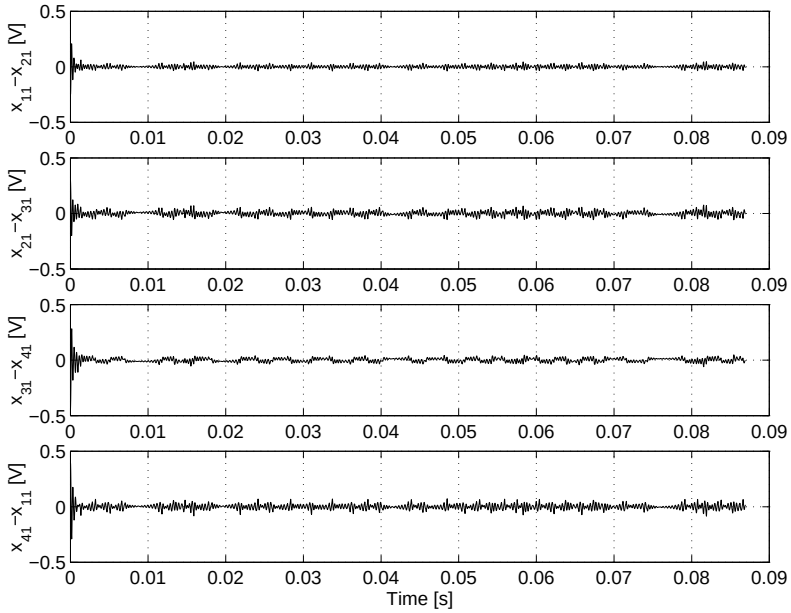

Figure 5.15: Synchronization error for $R_{c0} = R_{c1} = 3200$ [Ω].

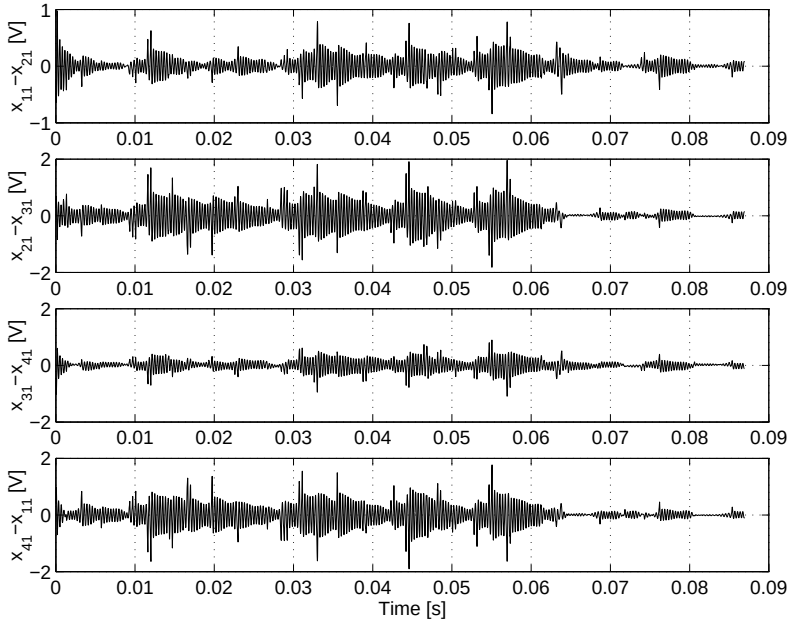

Figure 5.16: Synchronization error for $R_{c0} = R_{c1} = 8500$ [Ω].

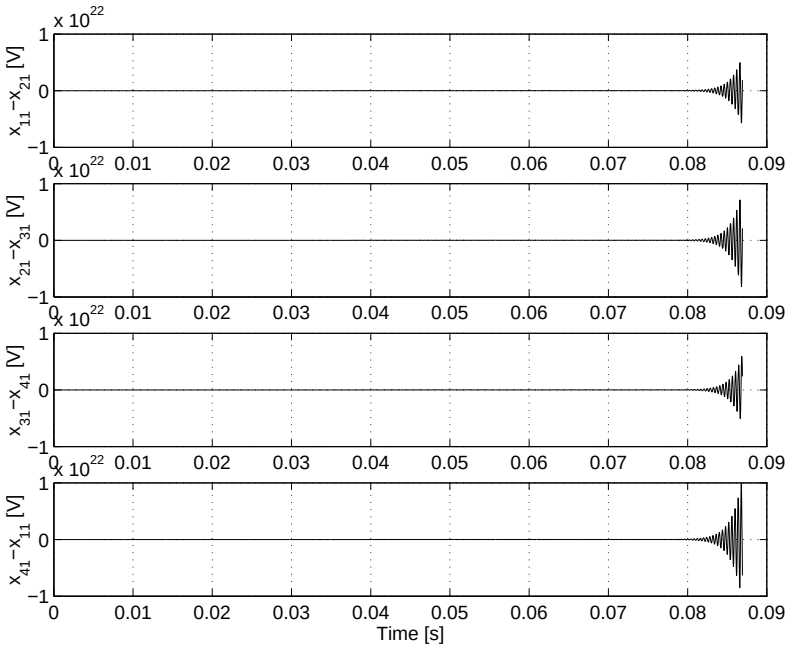

Figure 5.17: Synchronization error for $R_{c0} = R_{c1} = 20000$ [Ω].

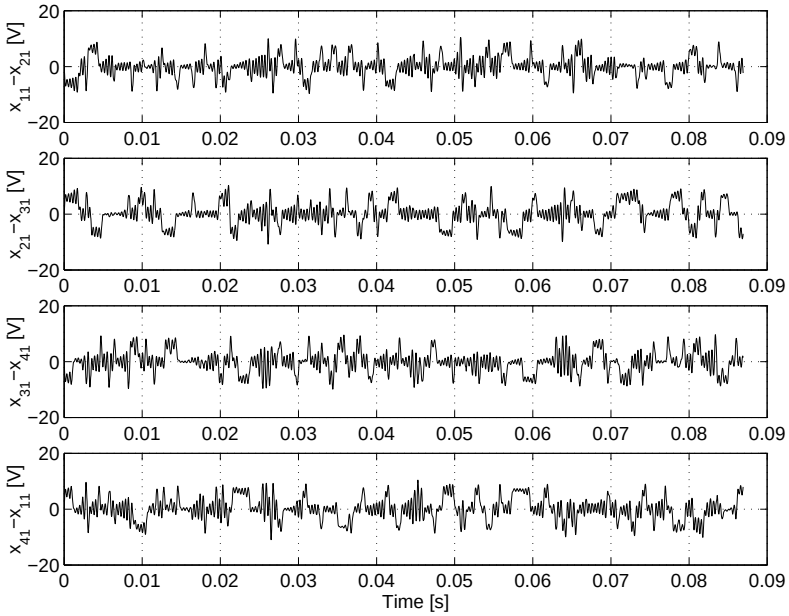

Figure 5.18: Synchronization error for $R_{c0} = R_{c1} = 70000$ [Ω].

Chapter 6

Conclusions and recommendations

As final part of this thesis conclusions are drawn and recommendations for future research are presented.

6.1 Conclusions

In this thesis the complex behavior of multiple hybrid chaotic systems has been investigated. This objective has been achieved by analyzing multiple Chua circuits. The objective has been divided into three main aspects and conclusions will be drawn accordingly.

6.1.1 Analysis of a single Chua circuit

The Chua circuit is a complex system capable of generating bifurcation and chaos phenomena. The nonlinearity of the circuit is given by a piece-wise linear characteristic, which consists of three linear parts. The dynamic behavior is analyzed by looking at the stability properties of the equilibria and a 2D Poincaré map is derived to explain the bifurcations. This complex Poincaré map is approximated by a simpler 1D Poincaré map, which can be calculated for any given parameter set. The qualitative behavior of the Chua circuit can be visualized by iterating this 1D Poincaré map, without actual integration of the differential equations. With the 1D Poincaré map the single scroll and 'birth' and 'death' of the double scroll trajectories are explained.
To classify a system as chaotic it has to satisfy certain properties. We showed that these conditions can be fulfilled and therefore we can conclude that a Chua circuit is a chaotic system.

6.1.2 Development and comparison with experimental results

To compare the obtained numerical results with experimental results a new experimental setup has been designed. This resulted in a small portable setup with some additional advantages to previous designs. The circuit can be divided into two subsystems to measure the nonlinear resistor or a resonance circuit, consisting of the inductor, separately. Further data acquisition devices or other circuits can be easily connected.

To identify the parameters of the experimental setup two identification methods are used. First the parameters are determined by experiments of the separate subsystems and secondly three different Kalman filters are developed and compared.
With the obtained parameters numerical simulations are carried out to compare the results with experiments. However if the obtained parameters from measurement identification or the Kalman filters are used in a numerical simulation, without using measurement data, the solution always differs from experimental data. There are two important reasons for this.
Although all the experimental trajectories are qualitatively comparable with numerical results, there is a quantitative difference. This difference is also present if we compare a measured single

limit cycle with a filtered result obtained by a Kalman filter, which indicates that the used model in the Kalman filter is not correct.
This is caused by the assumptions we made on the location of the breakpoints and the fact the dynamic behavior of the electric components is neglected.
Secondly if we are able to develop an exact model, it is still impossible to obtain the same trajectory when the circuit generates a chaotic time signal. We can only measure with a finite precision and a numerical solver causes unwanted rounding and truncation errors. Due to the sensitivity of initial conditions the trajectories will always diverge from each other.

6.1.3 Synchronization of multiple circuits

As last part of this thesis we considered two synchronization methods, master-slave synchronization and mutual synchronization.

In the case of master-slave synchronization two Chua circuits, operating at the double scroll attractor, are unidirectionally coupled. This is achieved by applying a negative feedback to the slave system. Two different feedback signals are considered. We used either the voltage across the capacitor in parallel with the nonlinear resistor or the voltage across the capacitor in parallel with the inductor to create the feedback signal, state one or two respectively.
To be able to specify asymptotic synchronization of non-identical systems we introduced a form of practical synchronization. This is done because one of the drawbacks of the experimental setup is that it is impossible to achieve a zero synchronization error due to tolerances in presumably identical electrical components of the circuits.
It followed from both simulations and experiments that synchronization is possible. A smaller synchronization error is obtained if the coupling strength is increased and the error is also smaller if the first state is used to compose the feedback signal.
Besides synchronization we also observed intermittency when the second state is used in the feedback signal.

In the case of mutual synchronization the circuits are diffusively coupled using the first state. First synchronization of two systems is considered. Again by increasing the coupling strength the synchronization error decreases. However if the coupling strength is decreased the systems starts to desynchronize and above a certain threshold value a bursting phenomenon is observed and the trajectories are no longer bounded by the attractor. If a second threshold is crossed, the coupling is too weak to synchronize the circuits and they operate as free systems.
Secondly we looked at synchronization in a network of four symmetrically coupled Chua circuits. In this case there are three linear invariant manifolds, corresponding to a partial synchronized situation. Two of these manifolds can be made locally stable if the trajectories remain bounded by the double scroll attractors. Global stability is not obtained because a Chua circuit is not (semi)passive, which can result in unbounded trajectories. However on the experimental setup the solutions are normally bounded by the attractor. Therefore by altering the coupling strength one of the manifolds can be made locally stable and as a result partial synchronization is experimentally observed. These experimental observations are confirmed by performing several simulations.

To achieve synchronization of chaotic dynamical systems several aspects play a role. The way of coupling and the coupling strength are two important factors for experimental synchronization of non-identical systems. The systems' input-output relations can be used to prove (semi)passivity of the system, which guarantees bounded solutions.
If a dynamical system, driven by a bounded external signal, is convergent the solutions will forget their specific initial conditions. This indicates that if convergent systems are synchronized they remain synchronized.
For the Chua circuit we proved that the using the first state the system is convergent, while using the second state we can not prove this. This might explain the intermittency when the second state is used in the feedback signal.

6.2 Recommendations

Besides a better understanding of the very complex behavior of a Chua circuit several observations have been made in this thesis leading to a number of recommendations for further research.

- We concluded that it is impossible to obtain the same numerical trajectory when a dynamical system generates a chaotic time signal if no measurement information is used. To use measurement information a robust observer can be used to correct a numerical solution from time to time. This can also be viewed as a form of synchronization (Nijmeijer and Mareels, 1997).
- Experimental setup: At the current setup a fixed voltage supply of $\pm 15\ V$ is used, a variable voltage supply could be used to place the locations of the breakpoints more symmetrically. The possible frequency dependency of the nonlinear resistor should be investigated further. If this effect is caused by the operational amplifiers a different realization of the nonlinear resistor may be desirable.
- Identification: First of all one should consider if the used numerical model is accurate enough to fully describe the electrical dynamics.
  One of the drawbacks of using a Kalman filter is the initialization (P, R, Q matrices) of the filter and this needs more attention. One of the problems with the current model is that it is ill-conditioned and this can lead to instability of the filter. The estimation of the states and parameters might improve if a dimensionless model can be implemented.
  A filter that is also capable of estimating the location of the breakpoints can improve the current results, e.g. (Santoboni and Nijmeijer, 2001)
- Synchronization: The bursting phenomenon, which occurs if the coupling strength crosses a certain threshold value, should be investigated further. A possible technique that can be used is the examination of transverse Lyapunov exponents of the synchronization manifold (Heagy *et al.*, 1994; Pecora, 1998).
  The possibility of real-time synchronization / identification between an experimental setup and a numerical model may be realized using a TUeDacs in combination with a TUeDAX Linux Live CD.

Bibliography

Awrejcewicz, J. and M.L. Calvisi (2002). Mechanical models of chua's circuit. *International Journal of Bifurcation and Chaos* **12**(4), 671–686.

Carroll, T.L. and L.M. Pecora (1991). Synchronizing chaotic circuits. *IEEE Transactions on Circuits and Systems* **38**(4), 453–456.

Chua, L.O., M. Komuro and T. Matsumoto (1986). The double scroll family. *IEEE Transactions on Circuits and Systems* **33**(11), 1073–1118.

Chua, L.O., T. Yang, G.-Q. Zhong and C.W. Wu (1996). Synchronization of Chua's circuits with time-varying channels and parameters. *IEEE Transactions on Circuits and Systems* **43**(10), 862–868.

Criens, C.H. (2005). Het gedrag van een negatieve weerstand voor een Chua circuit. Technical report. Eindhoven University of Technology. DCT nr. 2005.49.

Cruz, C. and H. Nijmeijer (2000). Synchronization through filtering. *International Journal of Bifurcation and Chaos* **10**(4), 763–775.

Cruz, C., H. Nijmeijer and A. Aguilar (2001). Synchronization of a noisy Chua circuit via two switching Kalman filters. *Journal of the Mexican Society of Instrumentation* **5**(3), 162–169.

Cruz, J.M. and L.O. Chua (1992). A CMOS IC nonlinear resistor for Chua's circuit. *IEEE Transactions on Circuits and Systems* **39**(12), 985–995.

Dedieu, H., M.P. Kennedy and M. Hasler (1993). Chaos shift keying: Modulation and demodulation of a chaotic carrier using self-synchronizing Chua's circuits. *IEEE Transactions on Circuits and Systems II* **40**(10), 634–642.

Devaney, R.L. (1986). *An introduction to chaotic dynamical systems*. Benjamin/Cummings Publishing Co.. Menlo park.

Feigenbaum, M.J. (1978). Quantitative universality for a class of nonlinear transformations. *Journal of Statistical Physics* **19**(1), 25–52.

Gelb, A., Ed.) (2001). *Applied optimal estimation*. 16th ed.. M.I.T. Press. Cambridge MA.

Gray, C.M. (1994). Synchronous oscillations in neuronal systems: mechanisms and functions. *Journal of Computational Neuroscience* **1**, 11–38.

Grebogi, C., E. Ott and J.A. Yorke (1982). Chaotic attractors in crisis. *Physical Review Letters* **48**(22), 1507–1510.

Guckenheimer, J. and P. Holmes (1983). *Nonlinear oscillations, dynamical systems and bifurcations of vector fields*. Springer-Verlag. New York.

Hasler, M., Y. Maistrenko and O. Popovych (1998). Simple example of partial synchronization of chaotic systems. *Physical Review E* **58**(5), 6843–6846.

Heagy, J.F., T.L. Carroll and L.M. Pecora (1994). Synchronous chaos in coupled oscillator systems. *Physical Review E* **50**(3), 1874–1886.

Hees, M.H.G.W. (2004). Experimenteel bepalen van parameters van het Chua circuit. Technical report. Eindhoven University of Technology. DCT nr. 2004.71.

Huygens, C. (1986). *Christiaan Huygens' the pendulum or geometrical demonstrations concerning the motion of pendula as applied to clocks (translated by R. Blackwell).* Iowa State University Press. Ames, Iowa.

Kapitaniak, T. (2000). *Chaos for engineers.* 2nd ed.. Springer-Verlag. Berlin.

Kennedy, M.P. (1992). Robust Op Amp realization of Chua's circuit. *Frequenz* **46**(3-4), 66–80.

Leonov, G.A., D.V. Ponomarenko and V.B. Smirnova (1996). *Frequency methods for nonlinear analysis. Theory and applications.* World Scientific. Singapore.

Li, T.Y. and J.A. Yorke (1975). Period three implies chaos. *The American Mathematical Monthly* **82**, 985–992.

Lorenz, E.N. (1963). Deterministic nonperiodic flow. *Journal of the Atmospheric Sciences* **20**, 130–141.

Matías, M.A., V. Pérez-Muñuzuri, M.N. Lorenzo, I.P. Mariño and V.Pérez-Villar (1997). Observation of a fast rotating wave in rings of coupled chaotic oscillators. *Physical Review Letters* **78**(2), 219–222.

Matsumoto, T. (1984). A chaotic attractor from Chua's circuit. *IEEE Transactions on Circuits and Systems* **31**(12), 1055–1058.

Matsumoto, T., L.O. Chua and K. Tokumasu (1986). Double scroll via a two-transistor circuit. *IEEE Transactions on Circuits and Systems* **33**(8), 828–835.

May, R.M. (1976). Simple mathematical models with very complicated dynamics. *Nature* **261**, 459–467.

Mihajlovic, N. (2005). Torsional and Lateral Vibrations in Flexible Rotor Systems with Friction. PhD thesis. Technische Universiteit Eindhoven.

Nijmeijer, H. and A. Rodrigues-Angeles (2003). *Synchronization of mechanical systems.* World Scientific Publishing Co. London.

Nijmeijer, H. and I.M.Y. Mareels (1997). An observer looks at synchronization. *IEEE Transactions on Circuits and Systems* **44**(10), 882–890.

Ott, E., C. Grebogi and J.A. Yorke (1990). Controlling chaos. *Physical Review Letters* **64**(11), 1196–1199.

Pecora, L.M. (1998). Synchronization conditions and desynchronizing patterns in coupled limit-cycle and chaotic systems. *Physical Review E* **58**(1), 347–360.

Pecora, L.M. and T.L. Carroll (1990). Synchronization in chaotic systems. *Physical Review Letters* **64**(8), 821–824.

Pegna, G., R. Marrocu, R. Tonelli, F. Meloni and G. Santoboni (2000). Experimental definition of the basin of attraction for Chua's circuit. *International Journal of Bifurcation and Chaos* **10**(5), 959–970.

Pikovsky, A., M. Rosenblum and J. Kurths (2001). *Synchronization: A universal concept in nonlinear sciences.* Cambridge University Press. Cambridge.

Pogromsky, A.Y., G. Santoboni and H. Nijmeijer (2002). Partial synchronization: from symmetry towards stability. *Physica D* **172**, 65–87.

Poincaré, H. (1890). Sur les équations de la dynamique et le problème de trois corps. *Acta Mathematica* **13**, 1–270.

Pyragas, K. (1992). Continuous control of chaos by self-controlling feedback. *Physics Letters A* **170**, 421–428.

Quarles, T., A.R. Newton, D.O. Pederson and A. Sangiovanni-Vincentelli (1993). SPICE3 Version 3f3 User's Manual. Technical report. University of California.

Rössler, O.E. (1976). An equation for continuous chaos. *Physics Letters A* **57**(5), 397–398.

Ruelle, D. and F. Takens (1971). On the nature of turbulence. *Communications in Mathematical Physics* **20**, 167–192.

Santoboni, G. and H. Nijmeijer (2001). Synchronization with state and parameter estimation for Chua's circuit. Technical report. Eindhoven University of Technology.

Santoboni, G., A.Yu. Pogromsky and H. Nijmeijer (2001). An observer for phase synchronization of chaos. *Physics Letters A* **291**, 265–273.

Silva, C.P. (1993). Shil'nikov's Theorem - A tutorial. *IEEE Transactions on Circuits and Systems* **40**(10), 675–682.

Smale, S. (1967). Differentiable dynamical systems. *Bulletin of the American Mathematical Society* **73**, 747–817.

Terry, J.R., K. Scott Thornburg Jr., D.J. DeShazer, G.D. VanWiggeren, S. Zhu, P. Ashwin and R. Roy (1999). Synchronization of chaos in an array of three lasers. *Physical Review E* **59**(4), 4036–4043.

Ticos, C.M., E Rosa Jr., W.B. Pardo, J.A. Walkenstein and M. Monti (2000). Experimental real-time phase synchronization of a paced chaotic plasma discharge. *Physical Review Letters* **85**(14), 2929–2932.

van der Pol, B. (1927). Forced oscillations in a circuit with nonlinear resistance. *Philosophical Magazine* **3**, 65–80.

van der Pol, B. and J. van der Mark (1928). Frequency demultiplication. *Nature* **120**, 363–364.

van der Steen, R. and H. Nijmeijer (2006). Partial synchronization of diffusively coupled Chua systems: An experimental case study. *submitted*.

Verhees, T. (2004). A mechanical Chua's circuit: Feasible or not?. Technical report. Eindhoven University of Technology. DCT nr. 2004.66.

Šarkovskii, A.N. (1964). Coexistence of cycles of a continuous map of a line into itself. *Ukrainskii Matematicheskii Zhurnal* **16**, 61–71.

Willems, J.C. (1972). Dissipative dynamical systems part I: General theory. *Archive for Rational Mechanics and Analysis* **45**, 321–351.

Winfree, A.T. (1980). *The geometry of biological time*. Springer. New York.

Wouters, J.A.G. (2005). Parametervariatie bij het Chua circuit. Technical report. Eindhoven University of Technology. DCT nr. 2005.48.

Wu, C.W. and L.O. Chua (1995). Synchronization in an array of linearly coupled dynamical systems. *IEEE Transactions on Circuits and Systems* **42**(8), 430–447.

Zhang, Y., G. Hu, H.A. Cerdeira, S. Chen, T. Braun and Y. Yao (2001). Partial synchronization and spontaneous spatial ordering in coupled chaotic systems. *Physical Review E* **63**, 026211.

Zhong, G.-Q. and F. Ayrom (1985). Experimental confirmation of chaos from Chua's circuit. *International Journal of Circuit Theory and Applications* **13**, 93–98.

Appendix A

Reference frame

In this appendix the explicit coordinates of the points A, B, C, D, E and F in the D_0 and D_1 units, see figure A.1, are given in terms of the real and complex eigenvalues $\sigma_0 = \frac{\tilde{\sigma}_0}{\tilde{\omega}_0}$, $\gamma_0 = \frac{\tilde{\gamma}_0}{\tilde{\omega}_0}$, $\sigma_1 = \frac{\tilde{\sigma}_1}{\tilde{\omega}_1}$, $\gamma_1 = \frac{\tilde{\gamma}_1}{\tilde{\omega}_1}$. These coordinates are used to compute the approximated 1D Poincaré map.

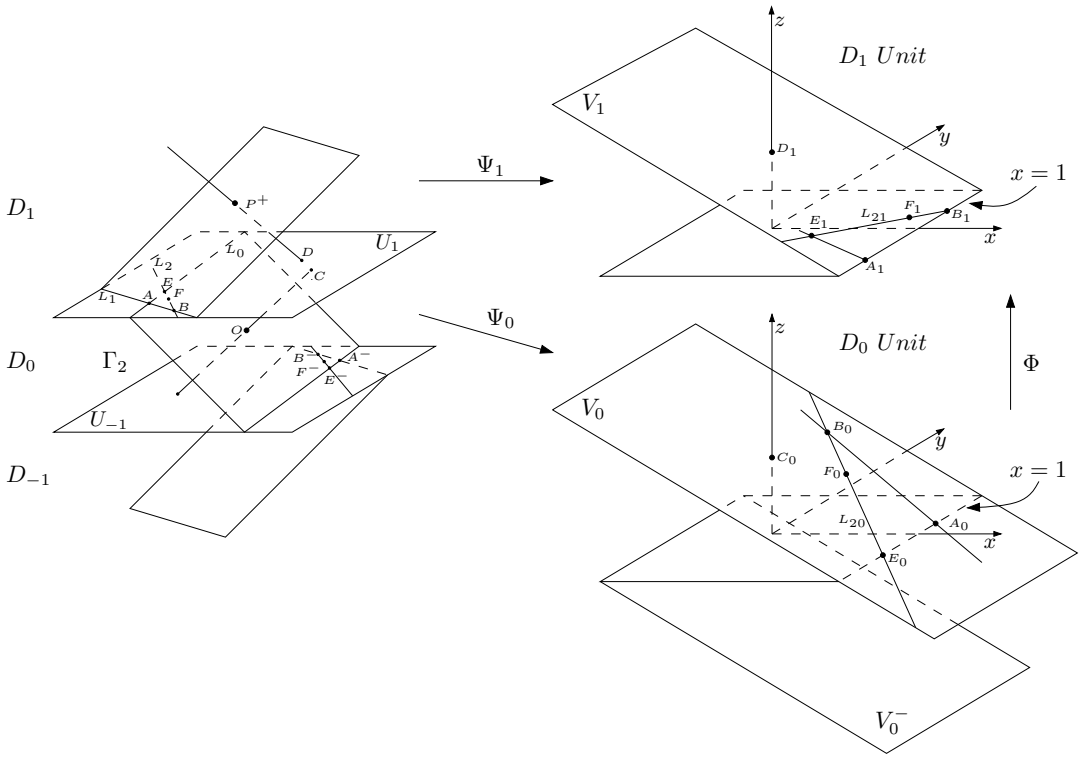

Figure A.1: Original system and their images in the D_0 and D_1 units of the transformed system.

A.1 D_0 unit

$$A_0 = [1\ p_0\ 0] \tag{A.1}$$

$$B_0 = \left[\frac{\gamma_0(\gamma_0-\sigma_0-p_0)}{Q_0}\ \frac{\gamma_0[1-p_0(\sigma_0-\gamma_0)]}{Q_0}\ 1-\frac{\gamma_0(\gamma_0-\sigma_0-p_0)}{Q_0}\right] \tag{A.2}$$

$$C_0 = [0\ 0\ 1] \tag{A.3}$$

$$E_0 = [1\ \sigma_0\ 0] \tag{A.4}$$

$$F_0 = \left[\frac{\gamma_0(\gamma_0-2\sigma_0)}{Q_0}\ \frac{\gamma_0[1-\sigma_0(\sigma_0-\gamma_0)]}{Q_0}\ \frac{(\sigma_0^2+1)}{Q_0}\right] \tag{A.5}$$

$$p_0 = \sigma_0+\frac{k_0}{\gamma_0}(\sigma_0^2+1) \tag{A.6}$$

$$Q_0 = (\sigma_0-\gamma_0)^2+1 \tag{A.7}$$

$$k_0 = -\frac{\tilde{\gamma}_0}{\tilde{\gamma}_1} \tag{A.8}$$

A.2 D_1 unit

$$A_1 = [1\ p_1\ 0] \tag{A.9}$$

$$B_1 = [1\ \sigma_1\ 0] \tag{A.10}$$

$$D_1 = [0\ 0\ 1] \tag{A.11}$$

$$E_1 = \left[\frac{\gamma_1(\gamma_1-\sigma_1-p_1)}{Q_1}\ \frac{\gamma_1[1-p_1(\sigma_1-\gamma_1)]}{Q_1}\ 1-\frac{\gamma_1(\gamma_1-\sigma_1-p_1)}{Q_1}\right] \tag{A.12}$$

$$F_1 = \left[\frac{\gamma_1(\gamma_1-2\sigma_1)}{Q_1}\ \frac{\gamma_1[1-\sigma_1(\sigma_1-\gamma_1)]}{Q_1}\ \frac{(\sigma_1^2+1)}{Q_1}\right] \tag{A.13}$$

$$p_1 = \sigma_1+\frac{k_1}{\gamma_1}(\sigma_1^2+1) \tag{A.14}$$

$$Q_1 = (\sigma_1-\gamma_1)^2+1 \tag{A.15}$$

$$k_1 = \frac{1}{k_0} \tag{A.16}$$

A.3 Connection map

The connection map Φ can be used to transform coordinates from the D_0 unit into the D_1 unit. Since $z_i = 1 - x_i$, we only need a relation for the x and y coordinates

$$\begin{bmatrix} x_1 \\ y_1 \end{bmatrix} = \Phi \begin{bmatrix} x_0 \\ y_0 \end{bmatrix}, \tag{A.17}$$

which can be rewritten as, cf. (Chua *et al.*, 1986),

$$\begin{bmatrix} x_1-1 \\ y_1-p_1 \end{bmatrix} = L \begin{bmatrix} x_0-1 \\ y_0-p_0 \end{bmatrix} \tag{A.18}$$

where L is given by

$$L = \frac{(\sigma_1^2+1)k_1}{(\sigma_0^2+1)(k_0+1)Q_1\gamma_1}\begin{bmatrix} -\gamma_1(k_0+1)[Q_0+\gamma_0(\sigma_0-\gamma_0)(k_1+1)] & \gamma_0\gamma_1(k_0+1)(k_1+1) \\ -\gamma_0(k_1+1)(\sigma_0-\gamma_0)[\sigma_1(\sigma_1-\gamma_1)+1] & \gamma_0(k_1+1)[Q_1+\gamma_1(\sigma_1-\gamma_1)(k_0+1)] \\ -\gamma_1(k_0+1)(\sigma_1-\gamma_1)[\sigma_0(\sigma_0-\gamma_0)+1] & \end{bmatrix} \tag{A.19}$$

Appendix B

Component list and layout

B.1 Component list

Table B.1: Component list.

Component	Value	Description
R_1	220 [Ω]	$\frac{1}{4}$ W resistor
R_2	220 [Ω]	$\frac{1}{4}$ W resistor
R_3	2200 [Ω]	$\frac{1}{4}$ W resistor
R_4	22000 [Ω]	$\frac{1}{4}$ W resistor
R_5	22000 [Ω]	$\frac{1}{4}$ W resistor
R_6	3300 [Ω]	$\frac{1}{4}$ W resistor
R_7	22 [Ω]	$\frac{1}{4}$ W resistor
R_8	100000[Ω]	$\frac{1}{4}$ W resistor
R_9	1500 [Ω]	$\frac{1}{4}$ W resistor
R_{10}	0-500 [Ω]	$\frac{1}{4}$ W resistor
C_1	10 $[nF]$	capacitor
C_2	100 $[nF]$	capacitor
C_3	10 $[nF]$	capacitor
C_4	1 $[\mu F]$	tantalum capacitor
C_5	1 $[\mu F]$	tantalum capacitor
C_6	1 $[\mu F]$	tantalum capacitor
C_7	1 $[\mu F]$	tantalum capacitor
C_8	1 $[\mu F]$	tantalum capacitor
C_9	1 $[\mu F]$	tantalum capacitor
C_{10}	1 $[\mu F]$	tantalum capacitor
C_{11}	1 $[\mu F]$	tantalum capacitor
$U_1,\ U_2,\ U_3,\ U_4$		AD712JN operational amplifier
$V1a,\ V2a$		BNC connector
$V1b,\ V2b$		pin
$X2a,\ X2b$		pin+jumper
$X3a,\ X3b$		pin+jumper

B.2 Layout

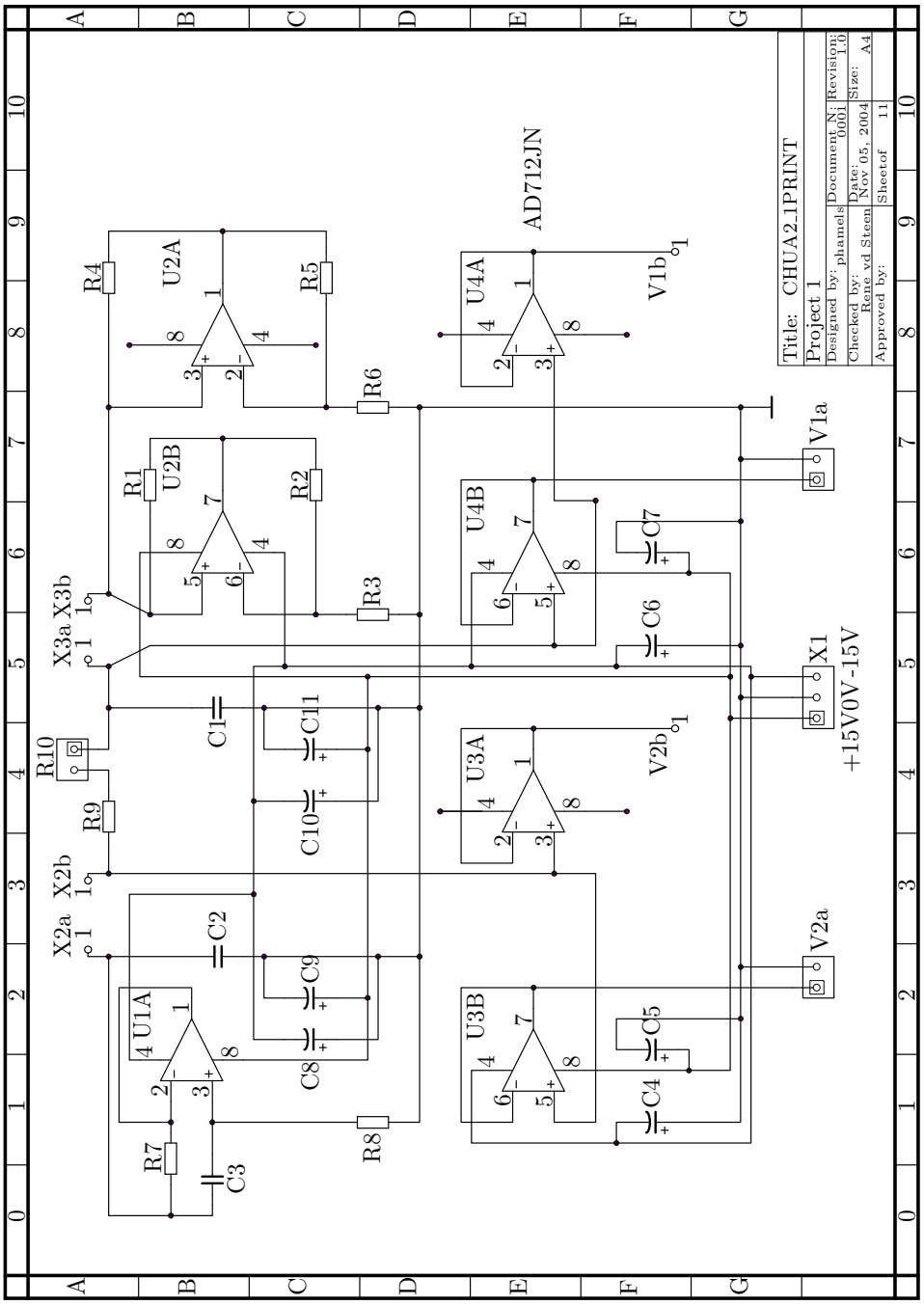

Figure B.1: Electrical layout

Acknowledgements

This thesis is the final result of intensive work on a seemingly simple electronic device. For the completion of this work several people have been a great help. First of all, I would like to thank my supervisor Henk Nijmeijer for his advise, guidance and above all his confidence during the last years of my study and especially the last week. I am also grateful for the trip to Prague, where I presented at the 16^{th} IFAC world congress. This has been a great experience.
Furthermore I would like to thank my coach Rens Kodde for his contribution in the practical part of this work. He helped me out with the electrical equipment I used to accompany the obtained theoretical results with experiments.
Another word of thanks goes to Peter Hamels for his help in the design of a new printed circuit board, he also did a great job by soldering the components on the new PCBs.
Further I am grateful for the everlasting support of my parents and brothers. At last I would like to thank my friends for all the help and the enjoyable time during all the years I have spent at the university.